# 論文 / 著書情報
# Article / Book Information

| | |
|---|---|
| 題目(和文) | |
| Title(English) | Evolution and Thermal Stability of Nanoclusters in Al-Mg-Si Alloys: Insights from Interatomic Structure of Clusters Formed at Low Temperature and Two-step Aging |
| 著者(和文) | Song Minyoung |
| Author(English) | MinYoung Song |
| 出典(和文) | 学位:博士(工学),<br>学位授与機関:東京工業大学,<br>報告番号:甲第12548号,<br>授与年月日:2023年9月22日,<br>学位の種別:課程博士,<br>審査員:小林 郁夫,史 蹟,藤居 俊之,多田 英司,村石 信二 |
| Citation(English) | Degree:Doctor (Engineering),<br>Conferring organization: Tokyo Institute of Technology,<br>Report number:甲第12548号,<br>Conferred date:2023/9/22,<br>Degree Type:Course doctor,<br>Examiner:,,,, |
| 学位種別(和文) | 博士論文 |
| Type(English) | Doctoral Thesis |

# Evolution and Thermal Stability of Nanoclusters in Al-Mg-Si Alloys: Insights from Interatomic Structure of Clusters Formed at Low Temperature and Two-step Aging

by

MinYoung Song

Doctoral Thesis

Department of Materials Science and Technology
Tokyo Institute of Technology

2023

東京工業大学
Tokyo Institute of Technology

# Nomenclature

| Symbol | Meaning |
|---|---|
| AA | Artificial aging |
| APT | Atom probe tomography |
| AQ | As-quenched |
| $Cluster^{Temp.}$ | Clusters formed at a specific temperature |
| $Cluster^{Temp.}_{time\ (ks)}$ | Clusters formed at a specific time and temperature |
| DSC | Differential scanning calorimetry |
| DBSCAN | Density-based Spatial Clustering of Applications with Noise |
| $D_{max}$ | Maximum distance between solute atoms |
| FIB | Focused ion beam |
| GP | Guinier-Preston |
| *k*NND | *k*th-nearest neighbor distance |
| $l_g$ | Gyration radius |
| LEAP | Local electrode atom probe |
| MSM | Maximum separation method |
| NA | Natural aging |
| NA (time ks) | Natural aging for specific time |
| $N_{min}$ | Minimum number of solute atoms |
| PA | Pre-aging |
| PALS | Positron annihilation lifetime spectroscopy |
| $\rho_{l_g}$ | Atomic density inside a cluster based on $l_g$ |
| $\rho_{r_G}$ | Atomic density inside a cluster based on $r_G$ |
| $r_G$ | Guinier radius |
| $r_G^{max}$ | Upper 10% of size of clusters based on $r_G$ |

| | |
|---|---|
| $r_G^{min}$ | lower 10% of size of clusters based on $r_G$ |
| SA | Single aging |
| SA(Temp.) | Single aging during a specific temperature |
| ST | Solution treatment |
| SSSS | Supersaturated solid solution |
| TTT | Time-temperature-transformation |
| TEM | Transmission electron microscopy |
| TSA(Temp.) | Two-step aging during a specific temperature |
| TSA (Temp., time (ks)) | Two-step aging during a specific time and temperature |
| Two (time ks) | Two-step aging for specific time ks after natural aging for 2419.2 ks |
| $V_{l_g}$ | Volume of a cluster based on $l_g$ |
| $V_{l_g}$ | Volume of a cluster based on $r_G$ |

# List of Contents

# Chapter 1

# General Introduction

## 1.1 Background

With the rapid emergence of environmental issues caused by recent climate change, there has been a growing global interest in achieving carbon neutrality. The significance of this matter was highlighted by the adoption of the Paris Agreement during the 21st Conference of the Parties (COP21) to the United Nations Framework Convention on Climate Change (UNFCCC) in 2015 [1]. The automotive industry plays an important role in current $CO_2$ emission levels. Therefore, the pursuit of weight reduction and fuel efficiency improvement in the automotive field is not an option, but a necessity. Research and development focused on weight reduction is particularly focused on reducing the weight of the body, which accounts for approximately 30% of the total vehicle weight. Meanwhile, as crash tests such as frontal and small overlap crash tests become more stringent [2], the automotive industry faces the challenge of meeting these rigorous requirements. To ensure compliance with these strict crash standards, it is essential to enhance the strength of vehicles. However, steel, which was widely used in the past, had limitations in reducing the weight of automobiles. Therefore, there is a need for the development of high-strength technology for lightweight aluminum alloys. The density of aluminum is approximately 2.7 g/cm$^3$ (at 20 °C), making it roughly one-third lighter than an equivalent volume of iron. Aluminum alloys can be broadly classified into two categories: casting alloys and wrought alloys. The wrought alloys, as depicted in Fig. 1.1, are further divided into eight different types. These wrought alloys can be categorized as age-

hardenable and non-age-hardenable alloys. Age-hardenable alloys are widely used as structural materials in various applications due to their ability to enhance mechanical properties through the formation of precipitates via heat treatment. The age-hardening effect can be obtained by bake-hardening process at the final stage of production of Al panels. This process involves performing an isothermal treatment at around 170 °C for approximately 20 minutes, resulting in improved mechanical properties.

### 1.2 General precipitation in age-hardening alloys

The age-hardening is one of the most effective strengthening mechanisms in designing high-strength alloys. It is based on the precipitation reactions that result in the formation of new phases from the solid solution. An important requirement for these precipitation reactions is the difference in solid solubility, which decreases as the temperature decreases. When such alloys with the aforementioned difference are rapidly quenched from high temperature (α single phase) to low temperature (α+β), the supersaturated α phase begins to undergo phase decomposition. In the subsequent isothermal reaction, before the equilibrium phases are formed, various transition phases (i.e. metastable phases) can be formed, leading to a complex multistage phase decomposition. The Al-Cu binary alloys are the classical age-hardening alloy. The generally accepted precipitation sequence is as follows: SSSS → GP Zone → θ″ → θ′ → θ. Where SSSS is supersaturated solid solution. The precipitation sequence is influenced by the aging temperature. Since the TTT diagram provides valuable information on the sequence of phase transformations during aging, the effect of that temperature can be understood through the TTT (Time-Temperature-Transformation) diagram, which is illustrated with metastable solvus lines as shown in Fig. 1.2 [3]. For a given alloy composition, the solvus temperature of each phase and the C-shape of the TTT curve can be seen. From these, two general precipitation

phenomena are noted based on aging time and temperature. Firstly, the type of precipitates initially formed varies with temperature, but given sufficient aging time, equilibrium precipitates can also be formed. Secondly, precipitates formed at higher temperatures and longer aging times are thermally stable, and vice versa. However, the details of the complex reaction pathways at lower temperatures vary depending on the type of alloy.

## 1.3 Age-hardening in Al-Mg-Si alloys

### 1.3.1 Precipitation sequence

The age-hardenable Al-Mg-Si alloys are widely used in automotive exterior panels. Research on the precipitation phenomenon of this alloy, also known as Al-$Mg_2Si$ pseudo-binary alloys, have been conducted. Figure 1.3 shows the phase diagram of this pseudo-binary alloys [4]. This alloy has the precipitation requirement mentioned in Section 1.2. The generally accepted precipitation sequence in Al-Mg-Si alloys is as follows [5–7].

$$\text{SSSS} \rightarrow \text{nanocluster} \rightarrow \text{GP zone} \rightarrow \beta'' \rightarrow \beta', \text{U1}, \text{U2}, \text{B}' \rightarrow \beta$$

β is the equilibrium phase. Before it is formed, there are several metastable phases. β′, U1, U2 and B′ are the metastable precipitates that are usually observed in over-aging condition [8]. U1, U2 and B′ are also known as Type A, Type B and Type C [6,9], respectively. β″ is the main strengthening phase observed in peak aging [5,7,10]. Obtaining the uniformly distributed fine β″ with high number density is the key factor in making high-strength Al-Mg-Si alloys. The nanoclusters formed at the early stage of phase decomposition influence on the formation of β″. Therefore, it is important to understand the clustering behavior.

### 1.3.2 Two-step aging

Figure 1.4 shows the manufacturing process of Al panel. It can be seen that the Al panel is produced by the two-step aging process exposed to room temperature (i.e. natural aging (NA)) before artificial aging (AA) at about 170 ℃ (i.e. bake-hardening). Since nanoclusters are formed during NA, their formation is inevitable during Al panel fabrication. It was first proposed by Pashley et al. [11] that the formation of nanoclusters causes harmful effect on the precipitate formation during subsequent artificial aging, so-called the *Negative effect of two-step aging*. This NA effect is dependent on total solute content [12], Mg/Si ratio [13–15], natural aging time [14,16] and AA temperature [17]. On the other hand, positive effect of NA on two-step aging behavior can be confirmed in alloys with low (Mg+Si<1 wt. %) total solute content [12] and high AA temperature (250 ℃) [17]. Unlike the variable influence of natural aging (NA) depending on the conditions, pre-aging (PA) performed at relatively high temperatures (T ≥ 70 ℃) always have a positive effect on the two-step aging behavior. The effects of NA and PA on the two-step aging behavior introduced above are related to the microstructure change during two-step aging due to the complex clustering behavior in Al-Mg-Si alloys. As shown in Fig. 1.5, the clustering behavior of pre-existing clusters during the two-step aging at a given AA temperature can be summarized into three categories: direct evolution, neither dissolution nor evolution, and evolution after dissolution/atomic rearrangement. The main factors determining these distinct clustering behaviors are the clustering evolution and thermal stability of nanoclusters.

### 1.3.3 Clustering evolution

The clustering evolution of the nanoclusters in Al-Mg-Si alloys shows an uncommon clustering evolution different from what was introduced in Section 1.2. Investigating the clustering evolution in this alloy is essential for understanding the complex two-step aging behavior in Al-Mg-Si alloys. The literatures reported so far in relation to the issues of clustering evolution are summarized as follows.

Gupta et al. [18] confirmed the double exothermal peak related to the clustering between 25 and 115 °C in DSC thermogram. They reported that these heat evolutions are derived from the clustering of different reaction rates. Yamada et al. [19] confirmed the presence of Si-rich clusters and GP zones at lower and higher temperatures than 70 °C, respectively, using low-temperature adiabatic calorimetry and electrical resistivity measurements. They introduced Si-rich cluster do not act as nucleation site for β″, whereas GP zone serves as nucleation site for β″. It can be confirmed from several literatures [20–22] that clusters formed at lower and higher temperatures than 70 °C have negative and positive effects on two-step aging behavior. Serizawa et al. [23] successfully characterized clusters formed at natural aging and 100 °C using APT, and defined those as Cluster (1) and Cluster (2), respectively. They reported that unlike Cluster (2), Cluster (1) cannot evolve to a more stable phase. The studies by Aruga et al. [24] and Kim et al. [16] also confirmed that even after prolonged natural aging (NA), Cluster (1) does not transition to a more stable phase. In order to understand those different clustering behavior, various studies [15,23,25,26] have reported differences in the size, composition, and vacancy concentration of the nanoclusters. However, despite these attempts, the difference in the characteristics of nanoclusters that explain the distinct clustering evolution are not clearly understood. New approach other than the existing characterization methods is needed.

### 1.3.4 Thermal stability

As introduced in Section 1.2, generally the phases formed at high temperature and long aging time are thermally stable. However, due to the unconventional thermal stability of the nanoclusters in Al-Mg-Si alloys, it is difficult to understand the two-step aging behavior in this alloy. In the following, the literatures reported so far related to the thermal stability of nanoclusters in Al-Mg-Si alloys are summarized.

Lorimer and Nicholson [27] have proposed that the model for reversion of GP zone based on thermodynamic stability of the clusters and the precipitates. They introduced that there is a critical size for determining the thermal stability of GP zone in Al-Zn-Mg alloys. The NA before artificial aging causes the positive effect on two-step aging in Al-Zn-Mg alloys on the contrast to the Al-Mg-Si alloys. In order to understand these differences, Pashley et al. [28] proposed a model based on the kinetics stability of the clusters. They considered the mean size of the clusters increasing with increasing aging time at a given temperature, but this model is also based on critical size. Suzuki et al. [29] reported that the effect of pre-aging with different temperatures on two-step aging cannot be fully interpreted by the previous model such as Lorimer and Nicholson [27] and Pashley et al. [28]. Serizawa et al. [23] confirmed that the Cluster (1) and Cluster (2) cannot be distinguished only by their size. Thus, the model about critical size cannot be applied for understanding the two-step aging behavior in Al-Mg-Si alloys. Asano et al. [30] reported that the model for elaborating the two-step aging in Al-Zn-Mg alloys based on the difference in the number of GP zones between the pre-aging and artificial aging. Refer to study of Hirata et al. [31], it can be confirmed that the model describing the two-step aging in Al-Zn-Mg alloys is difficult to apply to Al-Mg-Si alloys. Meanwhile, Kim et al. [16] confirmed the three distinct two-step aging behavior with the different NA time. They showed that the clusters formed after prolonged NA are more thermally unstable than the cluster formed initial stage of NA. They suggested that the all previous models cannot explain these three

stages, and that the thermal stability of nanoclusters in Al-Mg-Si alloys depends on their interatomic structure. However, there is still no direct experimental evidence to prove their idea. Therefore, characterization of the nanoclusters especially by interatomic structure, is essential to better understand the two-step aging behavior in Al-Mg-Si alloys.

### 1.3.5 Atom Probe Tomography

As introduced in Sections 1.3.3 and 1.3.4, the characterization of nanoclusters in Al-Mg-Si alloys is important. The TEM is powerful tool for analyzing the structure of fine precipitates. Nowadays, the Norwegian group from NTNU introduced that these nanoclusters can be observed by the low-angle annular dark field scanning TEM (LADDF-STEM). Although advanced compared to the past when they could hardly be observed [21], it is still insufficient to characterize the nanoclusters by TEM. The APT is the only technique capable of characterization the nanoclusters. In the following, the basic and shortcomings of APT experiment are introduced.

The Fig. 1.6 shows the schematic diagram of the APT [32]. When the pulse (voltage or laser) is applied to the specimen, the atoms apex on the specimen are ionized and evaporated. Then, these evaporated atoms are attracted to the detector and strike it. At that time, the time-of-flight (TOF) and spatial coordinate of each atom can be obtained. Based on this information, it is possible to identify the type of element and the position of individual atoms. Unfortunately, sometimes undesirable displacement of atoms, so-called trajectory aberrations, can occur when the evaporated atoms flight to the detector. Trajectory aberrations are caused by sources such as local magnification [33,34], chromatic aberrations [35–37], and crystallographic poles [38]. The local density fluctuation of the APT dataset caused by those APT experimental artifacts. Meanwhile, since the APT datasets do not provide the information about the clusters itself, the

cluster identification algorithm is used for analyzing the clusters. The maximum separation method (MSM) [39–41] is one of the representative cluster identification algorithms. Many researchers have been used the maximum separation method to characterize the nanoclusters in Al-Mg-Si alloys [14,23,25,26,42–54]. However, the MSM is sensitivity to local density fluctuation [55]. Moreover, although the result of MSM strongly depends on the user-defined parameters [41], there is still no guideline for determining the user defined parameters that can be used in all situations regardless of alloy type and pretreatment process. In order to obtain reliable cluster characterization results, it is important to find an optimum method.

### 1.4 Objectives of Present Thesis

Understanding the clustering behavior is not enough to elaborate the two-step aging behavior in Al-Mg-Si alloys. The clustering evolution and thermal stability of nanoclusters formed with different aging time at a given temperature are mainly discussed by characterizing the nanoclusters using APT. The main issues addressed in present thesis are summarized as follows.

I. There is currently no established consensus on the optimal method for characterizing clusters using cluster identification algorithms in APT.

II. No attempt has been made to investigate the transition behavior of nanoclusters at a elevated temperature than natural aging under considering diffusion rate of solute atoms.

III. The main factor of determining the thermal stability of nanoclusters is not clear.

IV. The reason for the different clustering evolution with different temperatures has not been fully understood yet.

V. The atomic-scale microstructure evolution during the initial stage of two-step aging has not been understood well.

To address the aforementioned issues, a novel method was employed to characterize the nanoclusters in Al-Mg-Si alloys by analyzing their interatomic structure. This approach successfully provided insights for better understanding the clustering evolution and thermal stability of nanoclusters. The main investigations conducted in this thesis are outlined as follows.

1. To optimize the user-defined parameters for characterizing the nanoclusters.
2. To investigate the transition behavior of nanoclusters.
3. To figure out the main factor of determining the thermal stability of nanoclusters.
4. To characterize the nanoclusters formed at different temperatures.
5. To investigate the microstructure evolution during the initial stage of two-step aging.

## 1.5 Outline of Present Thesis

The importance of understanding the clustering behavior of nanoclusters in Al-Mg-Si alloys is introduced in **Chapter 1** ***"General Introduction"***. This chapter deal with unclear aspects of clustering evolution and thermal stability of nanoclusters as well.

Optimization of the user-defined parameters in cluster identification algorithm was attempted based on the various characterization method for cluster characterization in ***Chapter 2 "Parameters optimization in cluster identification algorithms for characterizing nanoclusters in Al-Mg-Si-Cu alloy"***. Alternative algorithm that compensate for the limitations of MSM were considered. A guideline on how to determine user-defined parameters has been successfully proposed.

The transition behavior of the nanoclusters taking into consideration the diffusion rate of solute atoms is investigated in **Chapter 3** ***"Transition behavior of nanoclusters under***

***sufficient low-temperature aging time in Al-Mg-Si alloy"***. The aging time at the different temperatures is normalized to discuss transition behavior of nanoclusters. The transition behavior at 50°C is primarily discussed in comparison to NA.

The main factor of determining the thermal stability of nanoclusters are investigated in ***Chapter 4 "Interatomic structure as a determining factor of thermal stability of nanoclusters in Al-Mg-Si alloy"***. A new analysis with normalization for the different sizes of clusters is performed on the arrangement of atoms inside clusters. The relationship between the interatomic structure and thermal stability of the nanoclusters is mainly discussed.

The nanoclusters formed at different temperatures are characterized of the Al-Mg-Si alloy in **Chapter 5** ***"Correlation between nanocluster formation and aging temperature in Al-Mg-Si alloy"***. A new approach that overcomes the limitations of previous methods for nanocluster characterization is adopted. The two distinct characteristics of nanoclusters are mainly discussed.

The microstructure evolution during the initial stage of two-step aging is investigated in **Chapter 6** ***"Microstructural evolution at the initial stage of two-step aging in an Al-Mg-Si alloy characterized by an atom probe tomography".*** The dissolution of nanoclusters and nucleation of precipitates are simultaneously considered. The changes in internal structure of nanocluster and their partial dissolution are discussed. Moreover, effects of microstructure evolution on hardness change is elaborated.

Finally, the **Chapter 7** ***"General Conclusions"*** summarizes the main results and findings in **Chapter 2** through **5** of the present research works.

## References

[1] F.C.P.L. Rev, ADOPTION OF THE PARIS AGREEMENT Proposal by the President, 21932 (2015) 1–32.

[2] I.I. for H.S. IIHS, Small Overlap Frontal Crashworthiness Evaluation Crash Test Protocol (Version VI), (2017) 1–33.

[3] D.A. Porter, K.E. Easterling, M.Y. Sherif, Phase Transformations in Metals and Alloys, third ed., Taylor & Francis Group, Boca Raton, FL., 2009.

[4] I.J. Polmear, Light alloys: From traditional alloys to nanocrystals, Light Alloy. From Tradit. Alloy. to Nanocrystals. (2005) 1–421. https://doi.org/10.1016/B978-0-7506-6371-7.X5000-2.

[5] G.A. Edwards, K. Stiller, G.L. Dunlop, M.J. Couper, The precipitation sequence in Al–Mg–Si alloys, Acta Mater. 46 (1998) 3893–3904. https://doi.org/10.1016/S1359-6454(98)00059-7.

[6] K. Matsuda, Y. Sakaguchi, Y. Miyata, Y. Uetani, T. Sato, A. Kamio, S. Ikeno, Precipitation sequence of various kinds of metastable phases in Al-1.0mass% Mg2Si-0.4mass% Si alloy, J. Mater. Sci. 35 (2000) 179–189. https://doi.org/10.1023/A:1004769305736.

[7] C.D. Marioara, S.J. Andersen, H.W. Zandbergen, R. Holmestad, The influence of alloy composition on precipitates of the Al-Mg-Si system, Metall. Mater. Trans. A Phys. Metall. Mater. Sci. 36 (2005) 691–702. https://doi.org/10.1007/s11661-005-1001-7.

[8] C.D. Marioara, H. Nordmark, S.J. Andersen, R. Holmestad, Post-β″ phases and their influence on microstructure and hardness in 6xxx Al-Mg-Si alloys, J. Mater. Sci. 41 (2006) 471–478. https://doi.org/10.1007/s10853-005-2470-1.

[9] K. Matsuda, S. Ikeno, T. Sato, A. Kamio, Classification of metastable phases in Al-Mg2Si alloys by HRTEM, Mater. Sci. Forum. 217–222 (1996) 707–712. https://doi.org/10.4028/www.scientific.net/msf.217-222.707.

[10] H.W. Zandbergen, S.J. Andersen, J. Jansen, Structure determination of Mg5Si6:particles in Al by dynamic electron diffraction studies, Science 277 (1997) 1221–1225. https://doi.org/10.1126/science.277.5330.1221.

[11] D.W. Pashley, J.W. Rohdes, A. Sendorek, Delayed Ageing in Aluminium-Magnesium-Silicon Alloys: Effect on Structure and Mechanical Properties, J. Institue Met. 94 (1966) 41–49.

[12] C.S.T. Chang, I. Wieler, N. Wanderka, J. Banhart, Positive effect of natural pre-ageing on precipitation hardening in Al-0.44 at% Mg-0.38 at% Si alloy, Ultramicroscopy. 109 (2009) 585–592. https://doi.org/10.1016/j.ultramic.2008.12.002.

[13] L. Zhen, S.B. Kang, DSC analyses of the precipitation behavior of two Al–Mg–Si alloys naturally aged for different times, Mater. Lett. 37 (1998) 349–353. https://doi.org/10.1016/S0167-577X(98)00118-9.

[14] Y. Aruga, S.N. Kim, M. Kozuka, E. Kobayashi, T. Sato, Effects of cluster characteristics on two-step aging behavior in Al-Mg-Si alloys with different Mg/Si ratios and natural aging periods, Mater. Sci. Eng. A. 718 (2018) 371–376. https://doi.org/10.1016/j.msea.2018.01.086.

[15] A. Poznak, R.K.W. Marceau, P.G. Sanders, Composition dependent thermal stability and evolution of solute clusters in Al-Mg-Si analyzed using atom probe tomography, Mater. Sci. Eng. A. 721 (2018) 47–60. https://doi.org/10.1016/j.msea.2018.02.074.

[16] J. Kim, E. Kobayashi, T. Sato, Influence of natural aging time on two-step aging behavior of Al-Mg-Si(-Cu) alloys, Mater. Trans. 56 (2015) 1771–1780. https://doi.org/10.2320/matertrans.L-M2015824.

[17] J. Kim, S. Kim, E. Kobayashi, T. Sato, Thermal stability and transition behavior of nanoclusters during two-step aging at 250 °C in Al-Mg-Si(-Cu) alloys, Mater. Trans. 55 (2014) 768–773. https://doi.org/10.2320/matertrans.M2013411.

[18] A.K. Gupta, D.J. Lloyd, Study of precipitation kinetics in a super purity Al-0.8 pct Mg-0.9 pct Si alloy using differential scanning calorimetry, Metall. Mater. Trans. A. 30 (1999) 879–884. https://doi.org/10.1007/s11661-999-0081-1.

[19] K. Yamada, T. Sato, A. Kamio, Cluster formation and two-step aging behaviors of Al-Mg-Si alloys, Keikinzoku/Journal Japan Inst. Light Met. 51 (2001) 215–221. https://doi.org/10.2464/jilm.51.215.

[20] M. Saga, Y. Sasaki, M. Kikuchi, Z. Yan, M. Matsuo, Effect of pre-aging temperature on the behavior in the early stage of aging at high temperature for Al-Mg-Si alloy, Mater. Sci. Forum. 217–222 (1996) 821–826. https://doi.org/10.4028/www.scientific.net/msf.217-222.821.

[21] M. Murayama, K. Hono, Pre-precipitate clusters and precipitation processes in Al–Mg–Si alloys, Acta Mater. 47 (1999) 1537–1548. https://doi.org/10.1016/S1359-6454(99)00033-6.

[22] T. Sato, High strength and high ductility aluminum alloys with controlled nano-clusters, J. Japan Inst. Light Met. 56 (2006) 592–601. https://doi.org/10.2464/jilm.56.592.

[23] A. Serizawa, S. Hirosawa, T. Sato, Three-Dimensional Atom Probe Characterization of Nanoclusters Responsible for Multistep Aging Behavior of an Al-Mg-Si Alloy, Metall. Mater. Trans. A. 39 (2008) 243–251. https://doi.org/10.1007/s11661-007-9438-5.

[24] Y. Aruga, M. Kozuka, Y. Takaki, T. Sato, Formation and reversion of clusters during natural aging and subsequent artificial aging in an Al–Mg–Si alloy, Mater. Sci. Eng. A. 631 (2015) 86–96. https://doi.org/10.1016/j.msea.2015.02.035.

[25] M. Torster, H.S. Hasting, W. Lefebvre, C.D. Marioara, J.C. Walmsley, S.J. Andersen, R. Holmestad, The influence of composition and natural aging on clustering during preaging in Al-Mg-Si alloys, J. Appl. Phys. 108 (2010) 1–9. https://doi.org/10.1063/1.3481090.

[26] M.W. Zandbergen, Q. Xu, A. Cerezo, G.D.W. Smith, Study of precipitation in Al–Mg–Si alloys by Atom Probe Tomography I. Microstructural changes as a function of ageing temperature, Acta Mater. 101 (2015) 136–148. https://doi.org/10.1016/j.actamat.2015.08.017.

[27] G.W. Lorimer, R.B. Nicholson, Further results on the nucleation of precipitates in the AlZnMg system, Acta Metall. 14 (1966) 1009–1013. https://doi.org/10.1016/0001-6160(66)90229-X.

[28] D.W. Pashley, M.H. Jacobs, J.T. Vietz, The basic processes affecting two-step ageing in an Al-Mg-Si alloy, Philos. Mag. 16 (1967) 51–76. https://doi.org/10.1080/14786436708229257.

[29] S. Hisashi, M. Kanno, G. Itoh, A consideration on two-step aging in Al-Mg-Si alloy, J. Japan Inst. Met. 30 (1980) 609–616.

[30] K. Asano, K. Hirano, Two-Step Ageing in an Aluminum-5 wt% Zinc-1 wt% Magnesium Alloy, Trans. Japan Inst. Met. 9 (1968) 149–155. https://doi.org/10.2320/matertrans1960.9.149.

[31] T. Hirata, S. Matsuo, Two-Step Ageing Behaviours in an Al-1.2 wt% $Mg_2Si$ Alloy, Trans. Japan Inst. Met. 13 (1972) 231–237. https://doi.org/10.2320/matertrans1960.13.231.

[32] M.K. Miller, R.G. Forbes, Atom probe tomography, Mater. Charact. 60 (2009) 461–469. https://doi.org/10.1016/j.matchar.2009.02.007.

[33] F. Vurpillot, A. Bostel, E. Cadel, D. Blavette, The spatial resolution of 3D atom probe in the investigation of single-phase materials, Ultramicroscopy. 84 (2000) 213–224. https://doi.org/10.1016/S0304-3991(00)00035-8.

[34] F. VURPILLOT, F. DE GEUSER, G. DA COSTA, D. BLAVETTE, Application of Fourier transform and autocorrelation to cluster identification in the three-dimensional atom probe, J. Microsc. 216 (2004) 234–240. https://doi.org/10.1111/j.0022-2720.2004.01413.x.

[35] K. Stiller, P.J. Warren, V. Hansen, J. Angenete, J. Gjønnes, Investigation of precipitation in an Al-Zn-Mg alloy after two-step ageing treatment at 100° and 150°C, Mater. Sci. Eng. A. 270 (1999) 55–63. https://doi.org/10.1016/S0921-5093(99)00231-2.

[36] T. Engdahl, V. Hansen, P.J. Warren, K. Stiller, Investigation of fine scale precipitates in Al-Zn-Mg alloys after various heat treatments, Mater. Sci. Eng. A. 327 (2002) 59–64. https://doi.org/10.1016/S0921-5093(01)01876-7.

[37] E.A. Marquis, F. Vurpillot, Chromatic aberrations in the field evaporation behavior of small precipitates, Microsc. Microanal. 14 (2008) 561–570. https://doi.org/10.1017/S1431927608080793.

[38] B. Gault, M.P. Moody, J.M. Cairney, S.P. Ringer, Atom Probe Microscopy, 1st ed., Springer New York, New York, NY, 2012. https://doi.org/10.1007/978-1-4614-3436-8.

[39] D. Vaumousse, A. Cerezo, P.J. Warren, A procedure for quantification of precipitate microstructures from three-dimensional atom probe data, Ultramicroscopy. 95 (2003) 215–221. https://doi.org/10.1016/S0304-3991(02)00319-4.

[40] M.K. Miller, E.A. Kenik, Atom probe tomography: A technique for nanoscale characterization, Microsc. Microanal. 10 (2004) 336–341. https://doi.org/10.1017/S1431927604040577.

[41] J.M. Hyde, E.A. Marquis, K.B. Wilford, T.J. Williams, A sensitivity analysis of the maximum separation method for the characterisation of solute clusters, Ultramicroscopy. 111 (2011) 440–447. https://doi.org/10.1016/j.ultramic.2010.12.015.

[42] O. Engler, C.D. Marioara, Y. Aruga, M. Kozuka, O.R. Myhr, Effect of natural ageing or pre-ageing on the evolution of precipitate structure and strength during age hardening of Al–Mg–Si alloy AA 6016, Mater. Sci. Eng. A. 759 (2019) 520–529. https://doi.org/10.1016/j.msea.2019.05.073.

[43] Z.J. Cui, H.C. Jiang, D. Zhang, Y.Y. Song, D.S. Yan, L.J. Rong, Influence of Mn on the negative natural aging effect in 6082 Al alloy, Mater. Sci. Eng. A. 793 (2020) 139874. https://doi.org/10.1016/j.msea.2020.139874.

[44] W. Yu, H. He, W. Zhang, L. Li, C. Sun, Modulation of the natural aging effect on subsequent artificial aging in Al–Mg–Si aluminum alloys with alloying content～1wt% through temperature tuning, J. Alloys Compd. 814 (2020) 152277. https://doi.org/10.1016/j.jallcom.2019.152277.

[45] S. Zhu, H. Shih, X. Cui, C. Yu, S.P. Ringer, Acta Materialia Design of solute clustering during thermomechanical processing of AA6016 Al–Mg–Si alloy, 203 (2021). https://doi.org/10.1016/j.actamat.2020.10.074.

[46] W. Tu, J. Tang, L. Ye, L. Cao, Y. Zeng, Q. Zhu, Y. Zhang, S. Liu, L. Ma, J. Lu, B. Yang, Effect of the natural aging time on the age-hardening response and precipitation behavior of the Al-0.4Mg-1.0Si-(Sn) alloy, Mater. Des. 198 (2021) 109307. https://doi.org/10.1016/j.matdes.2020.109307.

[47] M.Y. Song, J.H. Kim, Microstructural evolution at the initial stage of two-step aging in an Al-Mg-Si alloy characterized by a three dimensional atom probe, Mater. Sci. Eng. A. 815 (2021) 141301. https://doi.org/10.1016/j.msea.2021.141301.

[48] H. Shishido, Y. Aruga, Y. Murata, C.D. Marioara, O. Engler, Evaluation of precipitates and clusters during artificial aging of two model Al–Mg–Si alloys with different Mg/Si ratios, J. Alloys Compd. 927 (2022) 166978. https://doi.org/10.1016/j.jallcom.2022.166978.

[49] Y. Aruga, M. Kozuka, T. Sato, Formulation of initial artificial age-hardening response in an Al-Mg-Si alloy based on the cluster classification using a high-detection-efficiency atom probe, J. Alloys Compd. 739 (2018) 1115–1123. https://doi.org/10.1016/j.jallcom.2017.10.220.

[50] A. Serizawa, S. Hirosawa, T. Sato, 3DAP Characterization and Thermal Stability of Nano-Scale Clusters in Al-Mg-Si Alloys, Mater. Sci. Forum. 519–521 (2006) 245–250. https://doi.org/10.4028/www.scientific.net/MSF.519-521.245.

[51] A. Serizawa, T. Sato, M.K. Miller, Effect of cold rolling on the formation and distribution of nanoclusters during pre-aging in an Al-Mg-Si alloy, Mater. Sci. Eng. A. 561 (2013) 492–497. https://doi.org/10.1016/j.msea.2012.10.070.

[52] H. Zhong, P.A. Rometsch, X. Wu, L. Cao, Y. Estrin, Influence of pre-ageing on the stretch formability of Al-Mg-Si automotive sheet alloys, Mater. Sci. Eng. A. 697 (2017) 79–85. https://doi.org/10.1016/j.msea.2017.05.009.

[53] Z. Jia, L. Ding, L. Cao, R. Sanders, S. Li, Q. Liu, The Influence of Composition on the Clustering and Precipitation Behavior of Al-Mg-Si-Cu Alloys, Metall. Mater. Trans. A. 48 (2017) 459–473. https://doi.org/10.1007/s11661-016-3850-7.

[54] Y. Weng, Z. Jia, L. Ding, S. Muraishi, Q. Liu, Clustering behavior during natural aging and artificial aging in Al-Mg-Si alloys with different Ag and Cu addition, Mater. Sci. Eng. A. 732 (2018) 273–283. https://doi.org/10.1016/j.msea.2018.07.018.

[55] L.T. Stephenson, M.P. Moody, P. V. Liddicoat, S.P. Ringer, New techniques for the analysis of fine-scaled clustering phenomena within Atom Probe Tomography (APT) data, Microsc. Microanal. 13 (2007) 448–463. https://doi.org/10.1017/S1431927607070900.

**Tables**

**Figures**

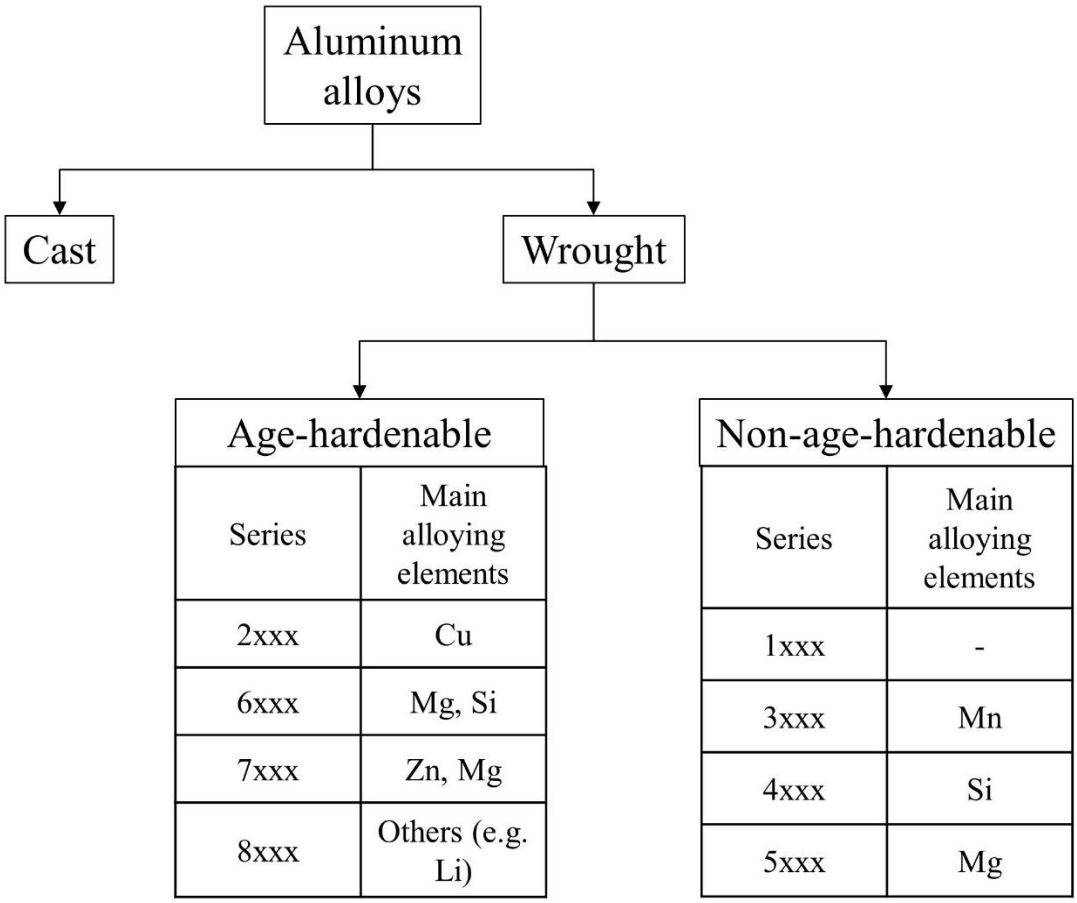


Figure 1.1 The general classification of Aluminum alloys.

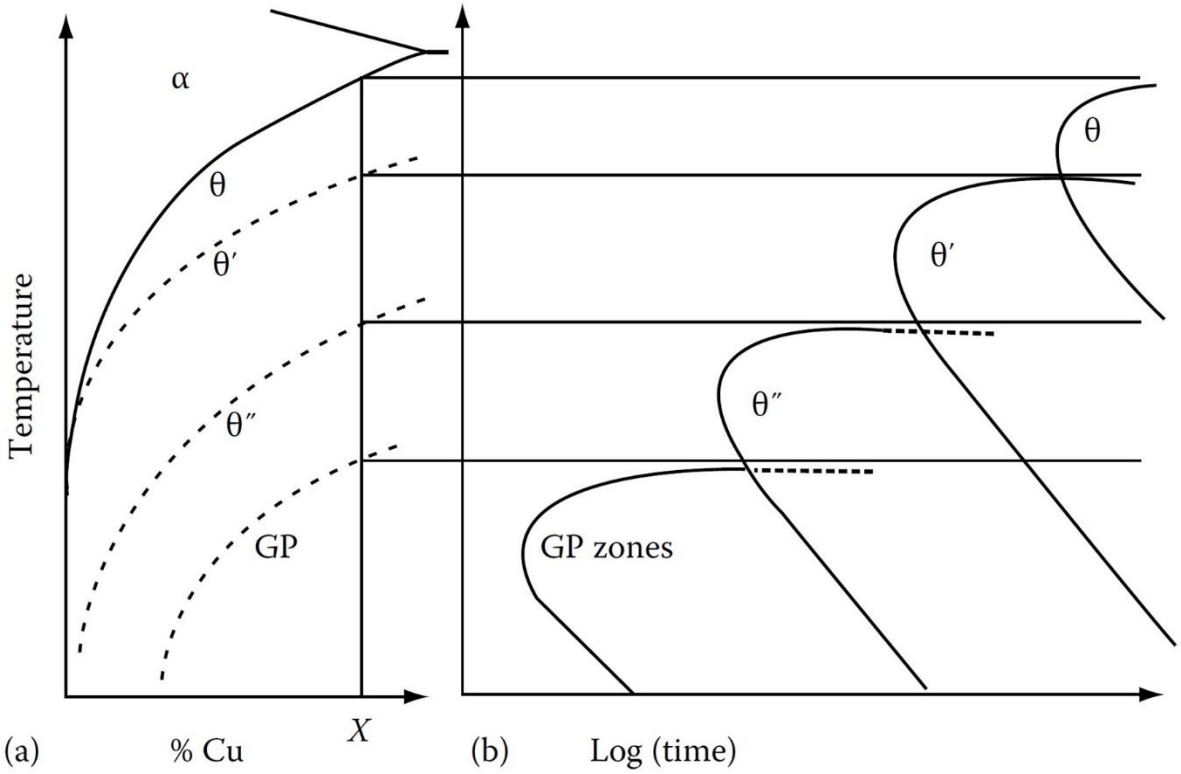


Figure 1.2 The schematic TTT diagram and metastable solvus line of Al-Cu binary alloys at a given composition [3].

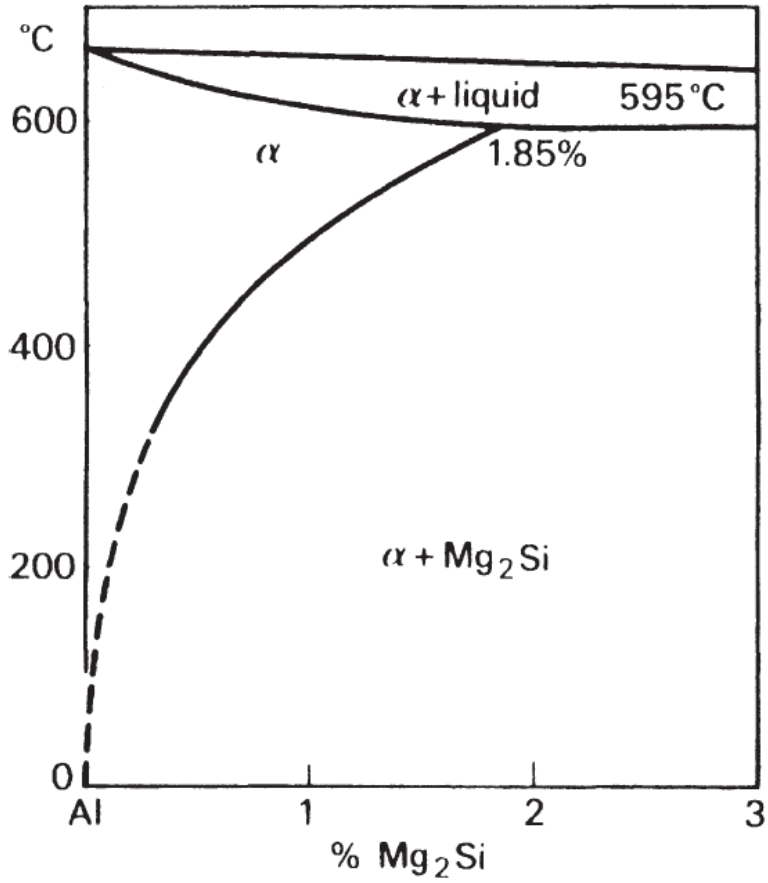


Figure 1.3 The Al-$Mg_2Si$ pseudo-binary phase diagram [4].

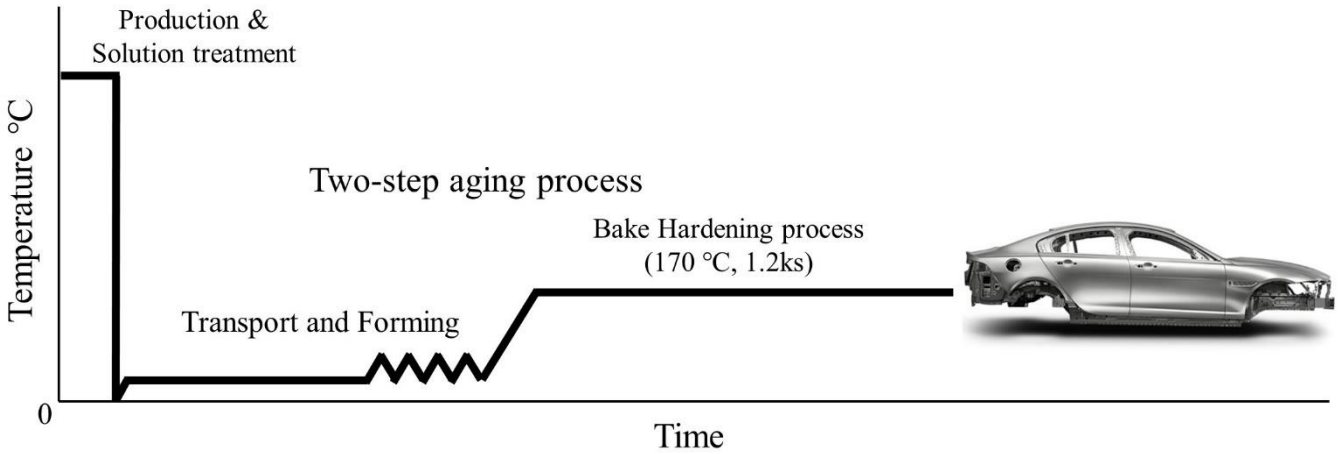


Figure 1.4 The manufacturing process of Al body panel.

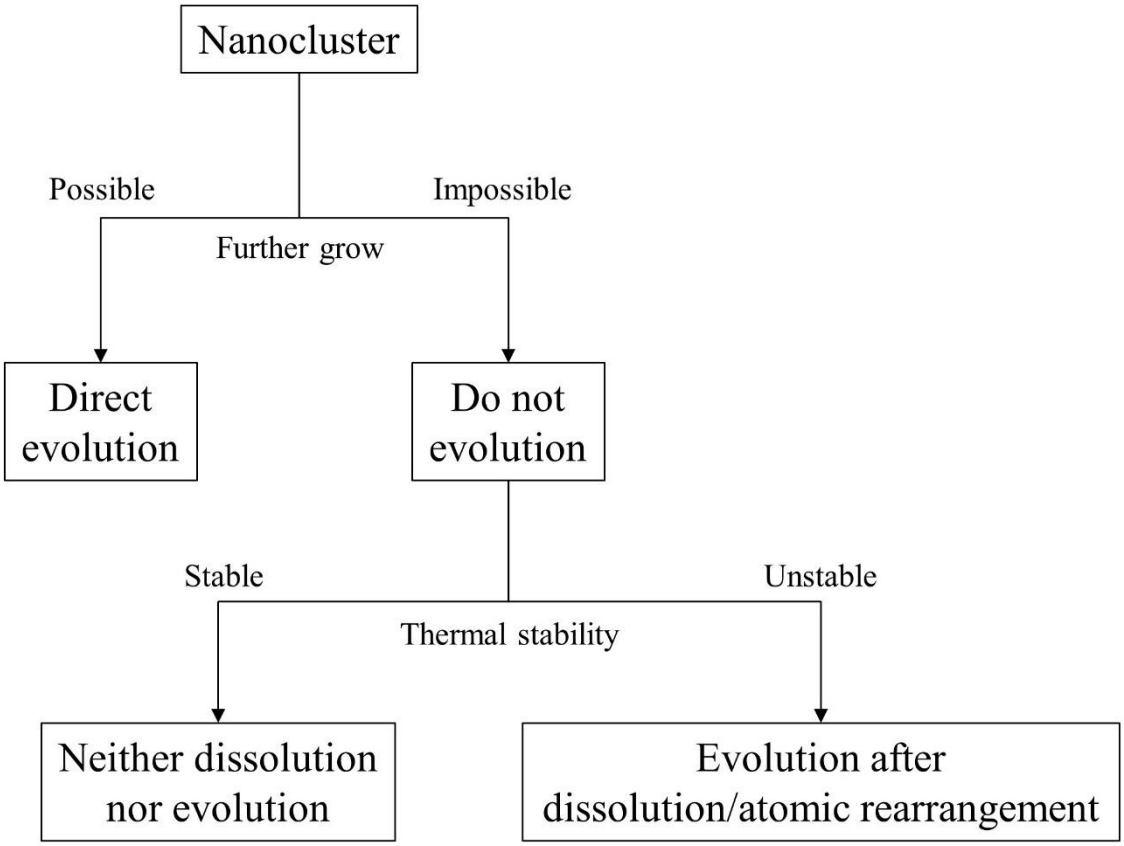


Figure 1.5 Classification of clustering behavior at a given artificial aging temperature.

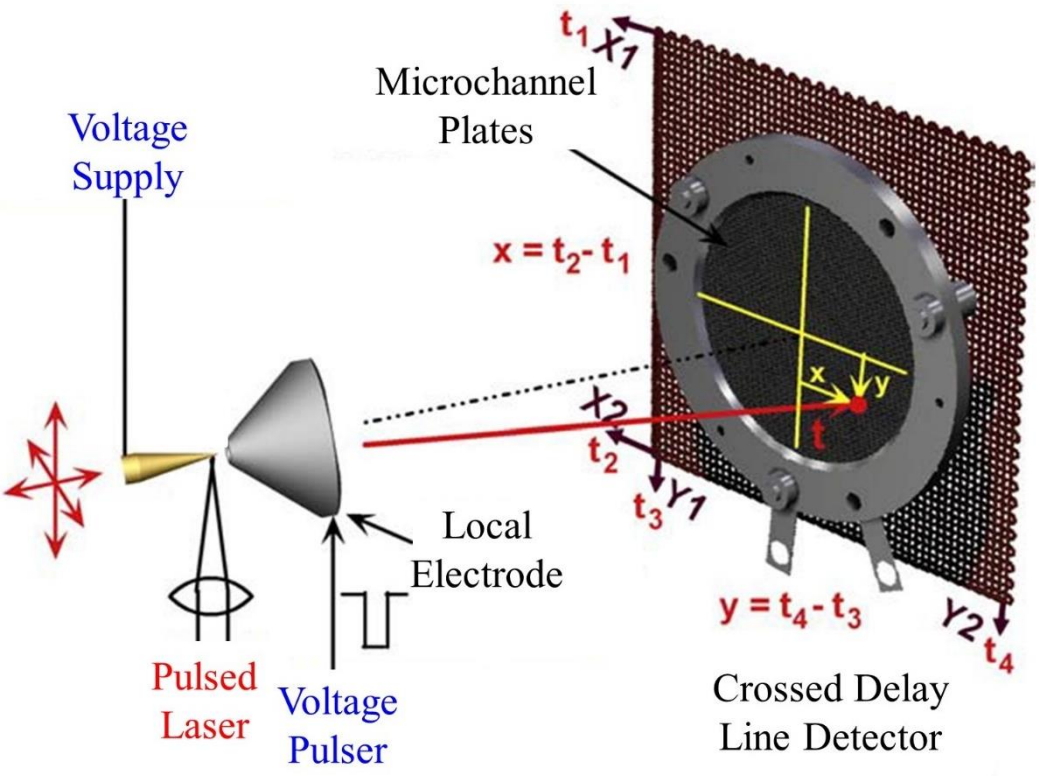


Figure 1.6 The schematic diagram of atom probe tomography [32].

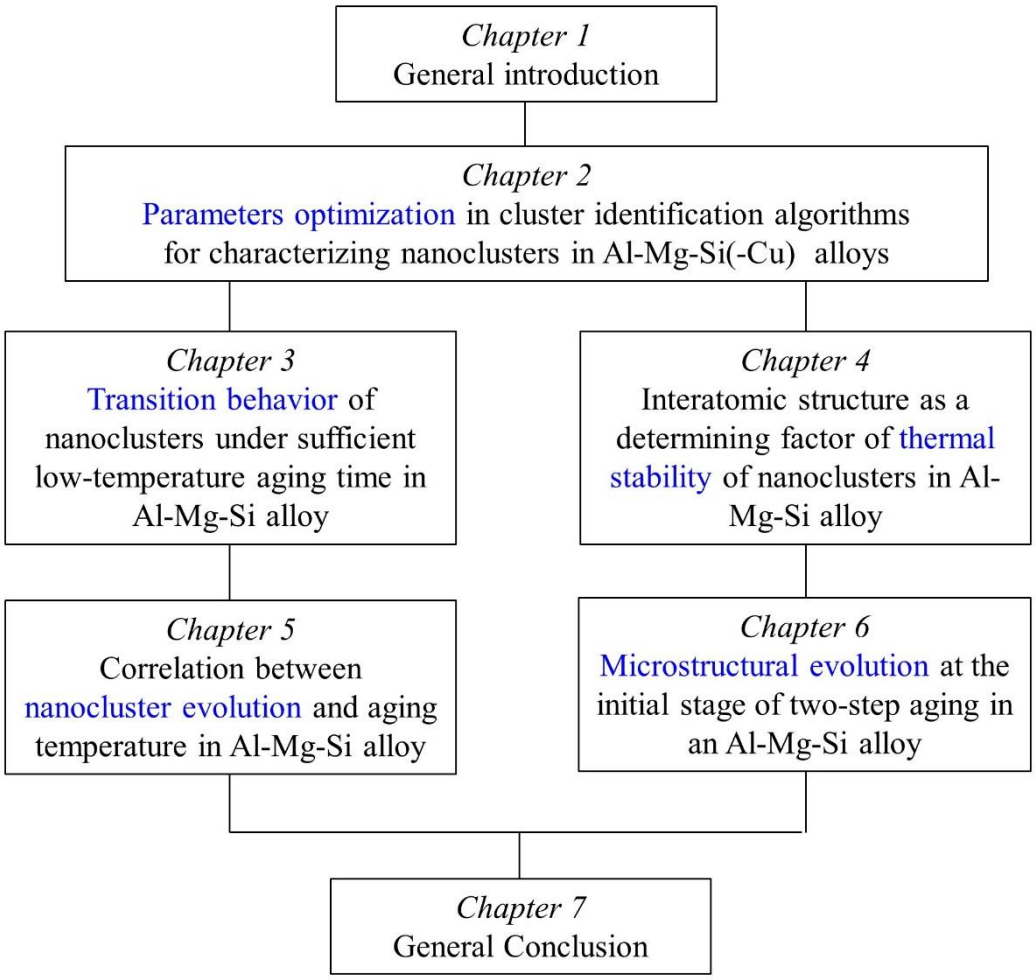


Figure 1.7 Schematic outline of present thesis.

# Chapter 2

# Parameters optimization in cluster identification algorithms for characterizing nanoclusters in Al-Mg-Si-Cu alloys

## 2.1 Introduction

The age-hardeable Al-Mg-Si alloys can lead to excellent mechanical properties by forming precipitates through heat-treatment. The formation of precipitates can be controlled by designing the alloy and heat-treatment history. The precipitation sequence of Al-Mg-Si-Cu alloy is as follows [1–4].

$$\text{SSSS} \rightarrow \text{Nanocluster} \rightarrow \text{GP zone} \rightarrow \beta'', \text{L, S, C, QP, QC} \rightarrow \beta', \text{Q}' \rightarrow \text{Q}$$

where SSSS and GP zone are the supersaturated solid solution and Guinieir-Preston zone, respectively. It is known that the nanoclusters are formed at the early stage of phase decomposition. The nanoclusters formed below and above 70 ℃ cause negative and positive effects on the subsequent precipitate formation, respectively [5–8]. These results indicate the existence of two types of nanoclusters that can be distinguished. Several researchers have been tried to characterize the two distinct nanoclusters [9–13]. However, the clustering behavior has not been fully understood yet despite these efforts. Since this lack of understanding is due to the limitation of characterization methods such as size, composition and atomic density, a new approach beyond the existing characterization method is needed. The metastable precipitates in Al-Mg-Si alloys are known to share similar atomic structure [14–17] which are useful for understanding the precipitation behavior of the metastable phases. It can be extrapolated that the structural relationships provide the information for better understanding the clustering

behavior. Therefore, in order to characterize the nanoclusters, it is necessary to understand factors related to atomic arrangement as well.

The transmission electron microscope (TEM) is useful for observing the atomic structure of precipitate. However, in multi-component alloys composed of elements in close proximity on the periodic table, it is nearly impossible to differentiate the constituent elements of particles with non-periodic atomic structures [18,19]. In practice, the nanoclusters in Al-Mg-Si alloys do not provide sufficient contrast to analyze them [6]. The Atom probe tomography (APT) is the only technique capable of detecting individual atoms of any element in a three-dimensional structure. Recently, studies on the clusters using APT have been reported [9,10,12,20–36]. Iso-concentration [37] and cluster identification algorithms have been used. The results of iso-concentration analysis vary depending on the chosen concentration level [38] (input parameter) without a clear selection criterion, and they do not provide quantitative information about the clusters themselves. Due to this reason, the use of cluster identification algorithms becomes necessary to obtain quantitative information about the clusters. The maximum separation method (MSM) [39–41], one of the cluster identification algorithms, is widely used in cluster analysis. Since the analysis result strongly depends on user-defined parameters ($D_{max}$ and $N_{min}$), it is important to determine these parameters. Table 2.1 shows the user-defined parameters that used in literatures. It can be seen that fixed user-defined parameters were applied to different experimental conditions (i.e. each experimental dataset). However, there are several artifacts in APT experiment. For instance, the chromatic aberration phenomenon, which depends on the atomic arrangement of small precipitates, causes ion trajectory aberrations [42]. In addition, the local magnification effect reduces the accuracy of determining atomic positions and is dependent on the atomic density [43] or size [42,44] of the precipitates. For those reasons, the application of fixed parameters is not desirable for characterizing clusters.

Since MSM is sensitive to local density fluctuations, it has the disadvantage that there is a possibility of identifying unphysical clusters by inducing single-link effect despite the using reasonable parameters [45] Density-based Spatial Clustering of Applications with Noise (DBSCAN) can compensate for these disadvantages of MSM. DBSCAN is MSM with one of the user parameters, order ($k$), added. MSM is a special case of DBSCAN (1st-order). The use of a high $k$ reduces the single-link effect by ignoring local density fluctuations, but allows only the identification of large clusters and ignores information about local atomic arrangement. Optimization of the combination of the user defined parameters ($D_{max}$, $N_{min}$, $k$) is required. The random labelling process [19,45,46] can provide $D_{max}$ and $N_{min}$ suitable for a given $k$, but there is currently no guideline for determining which combination of the three user-defined parameters is the optimal condition. In order to determine the optimal condition, it is necessary to establish a criterion that can distinguish whether it is a physical cluster or an unphysical cluster. Therefore, in this study, we proposed a methodology for optimizing user-defined parameters by minimizing the formation of unphysical clusters identified using the DBSCAN algorithm.

## 2.2 Methods

### 2.2.1 Experimental procedure

1.0 mm thick sheets with Al-0.9Mg-1.0Si-0.3Cu (mass %) alloy provided by UACJ Corp. (Japan) were used. The sheets were fabricated in size of 10×10 mm before heat treatment. The samples were solution heat treated (ST) at 560 ℃ for 1.8 ks in a salt bath containing a 1:1 mixture of $KNO_3$ and $NaNO_3$ powder, and then quenched in ice water at 0 ℃ for 0.06 ks. Each solution heat-treated alloy was undergone two separate heat treatment procedures; Natural

aging (NA) for 2419.2 ks and pre-aging (PA) at 100 °C for 3.6 ks were performed. These naturally aged and pre-aged specimens are shown as NA and PA samples, respectively. NA indicates room temperature exposure at around 25 °C. A Silicone Oil (Shin-Etsu, KF-96 1000CS) bath was used to conduct PA. After heat treatment, all samples for the APT were prepared using a cryo-focused ion beam (Helios NanoLab 600, FEI) under liquid nitrogen to avoid the specimen being exposed to room temperature and a temperature increase during FIB operation. A capping process using platinum was applied at the apex of samples while the FIB milling proceeded to prevent gallium implantation which may cause incorrect composition, or even the amorphization of crystalline regions [47,48]. Utilizing a local electrode atom probe (LEAP 4000X HRTM, CAMECA instruments Inc.) in the voltage pulsed mode with a pulse fraction of 20 % and under the operating temperature of approximately -223 °C in a vacuum of up to 3.8 x $10^{-11}$, the APT experiments were carried out. The Integrated Visualization and Analysis Software (IVAS 3.8.12) was used for all data processing of APT data such as reconstruction and visualization. Careful reconstruction is required for the reliability and reproducibility of the data since the results of cluster analysis by APT rely on reconstruction. Here, we demonstrate some key reconstruction methods applied in this study. First, to maintain integrity of depth resolution and avoid ion trajectory aberrations, the low-index poles were deliberately excluded from consideration. Second, the key input parameters for tomographic reconstruction, the image compression factor and k-factor, were calibrated based on a crystallographic calibration method [49] that matches the theoretically and experimentally measured interplanar spacing. The spatial distribution maps [50] were used to measure the interplanar spacing. The measured Mg/(Mg+Si+Cu) of NA and PA samples are 0.49 and 0.47, respectively.

### 2.2.2 Analysis

In the following, we introduce the random labelling process [19,45,46] that was used to determine the $D_{max}$ and $N_{min}$ in our analysis. Vaumousse et al. [39] showed that the *k*th-nearest neighbor distance (*k*NND) distribution can provide a guideline for determining the parameters of the density-based clustering algorithm. The *k*NND distribution follows a bimodal pattern in extremely dilute alloy which has a non-random solute cluster, thereby providing clear information about $D_{max}$ [49]. However, as the solute concentration increases, it becomes difficult to distinguish the origin of the *k*NND distribution [49]. In that case, it is necessary to use a comparator. Artifacts of the experimental dataset can be ignored using the randomly rebelled dataset (randomized dataset) [51]. Figure 2.1 shows how the $D_{max}$ is determined. Figure 2.1(a) is an example of the *k*NND distribution. Figure 2.1(b) represents the accumulated distribution of Fig. 2.1(a). The $D_{max}$ was set at the point where the maximum difference between the experimental and randomized datasets. Meanwhile, there are several reasons for applying $N_{min}$ [49], but we focused only on filtering random clusters caused by randomized datasets. Cluster size distribution [52] was used to filter out the random clusters. Figure 2.2 shows an example of the cluster size distribution with applied the $D_{max}$ obtained from Fig. 2.1. It is noted that if $N_{min}$ is too low and too high, respectively, small clusters might be ignored and a high proportion of random clusters can be identified [52] Taking this into consideration, $N_{min}$ was determined as the point where the random cluster (i.e. randomized) first reached zero. The identical method was applied for each individual $D_{max}$ since $N_{min}$ is a function of $D_{max}$. Table 2.2 shows the user-defined parameters determined from Figs. 2.1 and 2.2 in NA and PA samples. There are 10 combinations that the orders from the 1st to the 5th are considered for both samples.

## 2.3 Results

Figure 2.3 shows APT maps before and after applying DBSCAN with different combinations. APT maps of the before applying DBSCAN, 1st, 2nd, 3rd, 4th, and 5th-order combinations are shown in order from the left of each sample. Only solute atoms are shown in these APT maps. Red, blue and green dots represent Mg, Si and Cu atoms, respectively, and they do not reflect the actual atomic size. Table 2.3 shows the statistical data of clusters analyzed with different *k*th-order combinations. As the *k* increases, the average size and volume fraction of clusters tend to increase.

### 2.3.1 Characteristics not related to the atomic arrangement

Figure 2.4 shows size and composition of the clusters with different *k*th-order combinations. Figure 2.4(a) size distribution of clusters in NA sample. The size of the cluster was expressed based on the Guinier radius ($r_G$) [38], which is known to reflect the actual cluster size. It can be seen that the average size increases as *k* increases, and the deviation of the distribution increases. Figure 2.4(b) Mg fraction (i.e. Mg/solutes) distribution inside clusters in NA sample. For convenience of analysis, clusters with Mg fraction$<$0.4, 0.4$\leq$Mg fraction$\leq$0.6, and Mg fraction$>$0.6 were referred to as Si-rich cluster, Balanced cluster, and Mg-rich cluster, respectively. As the *k* increases, the fraction of Balanced clusters increases, but the fractions of Si-rich and Mg-rich clusters tend to decrease. In the PA sample (Fig. 2.4(d) and (e)), the change in size and Mg faction distribution with the *k* seems to be the same as in the NA sample (Figs. 2.4(a) and (b)). Figures 2.4(c) and (f) shows the Mg fraction with size in NA and PA samples, respectively. The dotted line and each dot represent the Mg fraction of the alloy and individual clusters, respectively. In both samples, as the *k* increases, it can be seen that the Mg fraction

approaches to the alloy composition as the increase in cluster size. There are only clusters having alloy composition above a certain size. These large clusters having alloy composition lead to high fraction of Balanced cluster.

Figure 2.5 shows distribution of atomic density inside clusters with different *k*th-order combinations. Atomic density is given by number of atoms inside a cluster over volume of a cluster. The two types of volume measuring methods used for atomic density analysis of clusters are summarized here. First, it is based on radius of gyration ($l_g$) [40]. The volume of the cluster based on $l_g$ is as follows.

$$V_{l_g} = (4/3)\pi l_x l_y l_z \tag{2.1}$$

where $\pi$ is the circumference rate, and $l_x, l_y, l_z$ are the one-dimensional radius of gyration. The other is based on Guinier radius ($r_G$). The volume of the cluster based on $r_G$ is as follows [45].

$$V_{r_G} = (4/3)\pi r_G^3 \tag{2.2}$$

where $r_G$ is given by

$$r_G = \sqrt{\frac{5}{3}({l_x}^2 + {l_y}^2 + {l_z}^2)} \tag{2.3}$$

Figure 2.5(a) shows distribution of atomic density ($\rho_{l_g}$) inside clusters based on $V_{l_g}$. Since the size of the cluster obtained by $l_g$ is underestimated, it shows a high atomic density on average. The clusters in all combinations except the 1st-order have an atomic density of less than 154 nm$^{-3}$, whereas the clusters with a maximum atomic density of 423 nm$^{-3}$ are confirmed in the 1st-order. Figure 2.5(b) shows distribution of atomic density ($\rho_{r_G}$) inside clusters based on $V_{r_G}$. The atomic density of the clusters is confirmed to be less than 18 nm$^{-3}$ in all combinations. It is noted that the deviation of 1st-order combination in $\rho_{r_G}$ is small, unlike in

$\rho_{l_g}$. The abnormally high atomic density observed only in $\rho_{l_g}$ is also confirmed in the PA sample (see Fig. 2.5(c)).

### 2.3.2 Features associated with the atomic arrangement

Figure 2.6 shows the concentration profile [53] with different *k*th-order combinations. It shows solutes (Mg+Si+Cu) concentration inside and outside of clusters. It is observed that the solutes concentration decreases as the distance from the center of the cluster increases in all combinations. Figures 2.6(b) and (d) are enlarged images of the areas indicated by the red dotted lines in Figs. 2.6(a) and (c), respectively. The black dotted lines in Figs. 2.6(a) and (c) indicate the measured solutes concentration of the matrix in each experimental dataset. In the 1st-order combination in both samples, it is confirmed that the solutes concentration of matrix region is higher than that of measured value, even though the matrix region, $d$=1.8 nm, is far from the clusters. It can be confirmed that solute concentration inside of clusters ($d$<1.0 nm) is similar with the measured solute concentration of the matrix under 4th and 5th-order combinations in both samples.

Figure 2.7 shows the distribution of first-nearest neighbor distance (1NND) of six solute pairs (Mg-Mg, Si-Si, Cu-Cu, Mg-Cu and Si-Cu) in NA (Fig. 2.7(a)) and PA (Fig. 2.7(b)) samples. Only the solutes atoms constituting the clusters identified by DBSCAN with different *k*th-order combinations were considered. As the *k* increases, the 1NND distribution broadened in both samples.

## 2.4 Discussion

### 2.4.1 Types of unphysical clusters

#### 2.4.1.1 Composition with size

The studies have been reported that the clusters formed at the initial stage of aging undergo Mg-enrichment as aging progresses using DSC [54–56], positron annihilation lifetime spectroscopy (PALS) [57,58] and modelling [59]. These studies support the fact that composition of clusters is an important factor for characterizing them. In studies using APT, the composition of the cluster is dependent on the alloy composition, that is, a high fraction of clusters similar to the alloy composition is commonly confirmed [10,13,32]. However, careful analysis is required if this alloy composition dependence is confirmed. In Fig. 2.4, it was confirmed that the high fraction of the Balanced cluster was caused by the large clusters having alloy composition. Ordinary Balanced clusters are difficult to determine physical/unphysical clusters, whereas the large clusters having alloy composition confirmed in Figs. 2.4(c) and (f) are considered as unphysical cluster. The difference between those large cluster having alloy composition and ordinary Balanced cluster come from size of the clusters. The inclusion of randomly distributed solute atoms (i.e. in matrix) contributed to the increase in size of the identified clusters. In the following, the reason for this is elaborated by employing a simplified approach considering only Mg and Si. Assume a situation in which a total of $n$ solute atoms having a ratio of Mg and Si atoms of $R_{\mathrm{Mg}}$:$R_{\mathrm{Si}}$ are randomly distributed. The number of Mg and Si atoms, $N_{\mathrm{Mg}}$ and $N_{\mathrm{Si}}$, are given by $nR_{\mathrm{Mg}}/(R_{\mathrm{Mg}}+R_{\mathrm{Si}})$ and $nR_{\mathrm{Si}}/(R_{\mathrm{Mg}}+R_{\mathrm{Si}})$, respectively. If $X$ is the number of Mg atoms selected at random when $r$ number of solute atoms are randomly selected, then $X$ follows the binomial distribution. The probability that $X = K$ is given by

$$P(X = K) = \left({}_{N_{\mathrm{Mg}}}\mathrm{C}_K\right)\left({}_{N_{\mathrm{Si}}}\mathrm{C}_{r-K}\right)/\,{}_n\mathrm{C}_r \tag{2.4}$$

where ${}_nC_r$ represents the number of cases where r solute atoms are selected from total of $n$ solute atoms where the order of the selection does not matter, and is obtained as $n!/(r!(n-r)!$.

The probability that Mg/(Mg+Si) is greater than A and less than B [$P$(A≤Mg/(Mg+Si)≤B)] can be calculated as follows.

$$\sum_{X=1}^{K} P(X = K), r\mathrm{A} \leq K \leq \mathrm{rB} \tag{2.5}$$

In NA and PA samples, an average of 3500 solute atoms were considered for analysis, and the largest number of solute atoms in the cluster was confirmed as 173. The $P$(0.4≤Mg/(Mg+Si)≤0.6) with the number of selected solute atoms ($r$) is plotted in Fig. 2.8 using Eqs. (2.4) and (2.5). Since the Mg fraction (Mg/solutes) of NA and PA samples was measured to be approximately 0.5, $R_{Mg}$:$R_{Si}$ = 1:1 was considered. It can be seen that as the $r$ value (x-axis) increases, the probability (y-axis) increases. This indicates that as the randomly distributed solute atoms within the matrix are included, the composition of the detected clusters become similar with alloy composition. Therefore, the large clusters with alloy composition are considered unphysical clusters that contain a significant number of solute atoms within the matrix.

#### 2.4.1.2 Atomic density

Zurob et al. [60] proposed a model for cluster growth in Al alloys. In their model, a key factor in cluster growth is vacancy escape from clusters dependent on the solute-vacancy binding energy ($E_b$). This model well describes the logarithmic change with aging time of electrical resistivity during clustering. They assumed only one type of solute atom, but this kind of change in electrical resistivity was also confirmed in Al-Mg-Si alloys [61]. The results obtained by Seyedezal et al. [61], using electrical resistivity and PALS, suggest the incorporation of vacancies into the clusters during clustering. Liu et al. [62] reported a study showing the change in vacancy concentration inside the cluster during clustering. Aruga et al.

[33] introduced the importance of atomic density analysis, which represents the concentration of vacancies inside clusters, using APT experiments to characterize clusters. Meanwhile, the abnormally high atomic density was observed in $\rho_{l_g}$, unlike $\rho_{r_G}$ (see Fig. 2.5). This difference arises from the considered morphological variations. Since the $V_{r_G}$ only considers the spherical shape, it overestimates volume of a cluster in the case of an ellipsoidal cluster. From Eq. (2.3), $l_x$, $l_y$, and $l_z$ can be expressed as the coordinates of a point on a sphere centered at the origin (0,0,0) with a radius of $\sqrt{(3/5)r_G}$. For convenience, the radius is simply denoted as $r$.

$$l_x{}^2 + l_y{}^2 + l_z{}^2 = r^2 \tag{2.6}$$

If Eq. (2.6) is expressed in spherical coordinates, it is given as follows.

$$(\mathrm{r}\cos\alpha)^2 + (\mathrm{r}\cos\beta)^2 + (\mathrm{r}\cos\gamma)^2 = r^2 \tag{2.7}$$

where $\cos\alpha$, $\cos\beta$ and $\cos\gamma$ are the direction cosines for $l_x$, $l_y$ and $l_z$ axes, respectively. From Eq. (2.6) and (2.7) $l_x l_y l_z$ is given as:

$$l_x l_y l_z = r^3 \cos\alpha \cos\beta \cos\gamma \tag{2.8}$$

From Eq. (2.8) $l_x l_y l_z$ has a maximum value when $\cos\alpha \cos\beta \cos\gamma$ is maximum. Due to the property of the direction cosine, $\cos^2\alpha + \cos^2\beta + \cos^2\gamma = 1$, the value of $l_x l_y l_z$ reach their maximum when $\cos\alpha = \cos\beta = \cos\gamma$. This means that among several $l_x, l_y, l_z$ combinations satisfying Eq. (2.6), a combination of three identical ones has the largest $l_x l_y l_z$. Assuming a cluster with $l_x, l_y, l_z$ as semi-axes, the volume of this cluster (Eq. (2.1)) is maximized when the cluster takes the form of sphere. Even with the same $r_G$ value, the atomic density ($\rho_{l_g}$) is lower for clusters with a more spherical shape, and vice versa. To confirm the relationship between morphology and atomic density ($\rho_{l_g}$), the relationship between $\rho_{l_g}$, $r_G$

and ellipticity is presented in Fig. 2.9. Only the clusters obtained from 1th-order combination in both samples are considered. In order to assess the ellipticity of clusters, the method commonly employed for evaluating the morphology of clusters [49,63] is utilized. When $l_x > l_y > l_z$, the oblateness is defined as $l_z/l_y$, and the aspect ratio is defined as $l_y/l_z$. In this study, the ellipticity, represented by the sum of oblateness and aspect ratio, indicates the degree of deviation from a perfect sphere. This ellipticity value close to 2 signifies a shape closer to a sphere. Referring back to the Fig. 2.9, the dotted circles represent the clusters with similar $r_G$. It is confirmed that the atomic density increases as the ellipticity decreases despite the similarity of $r_G$. In particular, clusters with an atomic density of 300 $nm^{-3}$ or higher have a string-type morphology, where the length of the shortest axis is less than 0.1 nm. These results indicate the atomic density is reverse proportional to the ellipticity. It is considered that the abnormally high atomic density observed exclusively in $\rho_{l_g}$ is attributed to the influence of morphology. Therefore, the clusters with abnormally high atomic density identified in $\rho_{l_g}$ are unphysical clusters.

#### 2.4.1.3 Concentration profile

Aruga et al. [32] introduced that Mg-enriched clusters are thermally unstable regardless of alloy composition, whereas Poznak et al. [13] reported that the thermal stability of nanoclusters is dependent on the alloy composition. In these contrasting studies conducted in the two groups, only the variation in atomic density based on the composition of clusters was considered. Therefore, it is important to analyze not only their size and composition, but also their concentration profile to fully understand the clustering behavior in Al-Mg-Si alloys.

In the 1st-order combination of both NA and PA samples, it was observed that the solutes concentration in the matrix region located at a distance of the cluster radius from the cluster (*d* = 1.8 nm) was higher than the measured solutes concentration in the matrix (see Figs. 2.6(b) and (d)). This situation is caused by identification of fragmented clusters. Furthermore, it was confirmed that solute concentration inside of clusters (d<1.0 nm) is similar with the measured solute concentration of the matrix under 4th and 5th-order combinations in both samples (see Figs. 2.6(b) and (d)). This situation is contributed to the connected clusters. The fragmented and connected clusters are visualized in a schematic diagram in Fig. 2.10. The 6×6×6 Al FCC unit cells were considered. Top and front views are expressed to clearly show the atomic distribution and bonds between solute atoms. Figs. 2.10 (c) and (d) represent a physical cluster. This physical cluster can be seen divided into four fragmented clusters as shown in Figs. 2.10(a) and (b). It is observed that the matrix region (bright gray region) of one fragmented cluster overlaps with the other fragmented cluster. This fragmented cluster results in a higher solute concentration than the measured solutes concentration of matrix. Meanwhile, Figs. 2.10 (e) and (f) represent a connected cluster. It appears that all regions are included within a single connected cluster. This means that the region that was the matrix of the physical cluster is recognized as the inside of the cluster in the connected cluster. Such misrecognition is reflected in the concentration profile results, resulting in the solutes concentration inside a cluster to be similar to the matrix. Therefore, the fragmented and connected clusters are considered as unphysical clusters.

### 2.4.2 Optimum condition

Table 2.4 shows the number of identified clusters obtained by applying the parameters that introduced in Table 2.1 to NA and PA samples. Since detection efficiency affects the results of

cluster analysis, only parameters applied in the literature using LEAP 4000 (used in this study) were considered. $N_{min}$ was fixed at 10, which was applied in most of the literature. Due to the presence of only a small number of clusters (5 or less) with $D_{max}$ values of 0.50 and 0.60 nm, only the cluster analysis results for NA and PA samples with $D_{max}$ values of 0.70 nm and 0.75 nm are presented in Fig. 2.11. Figs. 2.11 (a), (b) and (c) correspond to Figs. 2.4 (c)/(f), Figs. 2.5 (a)/(c) and Fig 2.6, respectively. From Figs. 2.11 (b) and (c), it is observed that unlike NA samples, the PA sample contains the fragmented clusters and the clusters that contribute to abnormally high atomic density. These clusters are unphysical clusters as discussed in Section 2.4.1. As a result, it demonstrates the importance of avoiding the use of fixed parameters for different datasets. Thus, it is desirable to independently apply the parameters that minimizes the unphysical clusters identified in Section 2.4.1 for each dataset. The combinations causing unphysical clusters are summarized in Table 2.5. The combinations where unphysical clusters were not observed in NA and PA samples were confirmed as 2nd and 2nd/3rd conditions, respectively. In the case of the PA sample, it is insufficient to determine the optimum parameters. In the following, another factor for determining the optimum combination is discussed.

The *k*th-nearest neighbor distance (*k*NND) is a fundamental method for analyzing the spatial distribution of different species in APT data. The *k*NND allows for precise analysis of difficult-to-identify cluster compositions [64], as well as providing information about the local atomic structure of amorphous alloys with short-range order [43]. In addition, it can be confirmed that it is effective in analyzing the change of short-range order caused by structural relaxation during annealing [65]. Thus, the *k*NND is useful to characterize the nanoclusters in Al-Mg-Si alloys. Meanwhile, it was confirmed that the 1NND distribution broadened as the order increased (see Fig. 2.7). As the *k* increased, $D_{max}$ increased (see Table 2.2). This large $D_{max}$ is

believed to cause the high deviation in 1NND during the selection process of border atoms in DBSCAN. This means that the *k*NND distribution result of less than k applied to DBSCAN may be misinterpreted due to the use of high order DBSCAN. When there are several combinations that unphysical clusters are not confirmed, such as the PA sample, it is considered reasonable to select a low order combination. Therefore, the optimum user-defined parameter for NA and PA samples are determined to be 2nd-order combination.

The distribution data of each element in space can be expressed as a scalar field. There are contouring and isosurfacing to visualize this data. The contouring means expressing scalar data of the same value as contour lines [37]. The volume render is a representative example of contouring in space. Isosurfacing is the representation of a surface at a given threshold in space [37]. Since the key to cluster analysis by the cluster identification algorithm is to find a region with higher solute concentration than the surroundings (i.e. matrix), it is worth comparing DBSCAN results with the volume renders and iso-concentration surfaces. Figure 2.12 shows a comparison of DBSCAN, volume render and iso-concentration surface. DBSCAN is the result of applying the 2nd-order combination to both NA and PA samples. It is confirmed that the distribution of the high-concentration solute atom region and the clusters identified by DBSCAN are in good agreement. Consequently, the proposed guidelines for optimizing user-defined parameters of the DBSCAN algorithm for characterizing nanoclusters in Al-Mg-Si alloys are concluded to be reasonable.

In this study, we identified unphysical clusters using various analysis methods useful for cluster characterization, and concluded that it was reasonable to select user-defined parameters that minimized them as optimum conditions. However, this optimization process has limitations. It is the ambiguity of the boundaries of physical and unphysical clusters. We plan to clearly suggest this boundary through quantitative analysis in the future.

## 2.5 Conclusions

An attempt was conducted to reduce the error of the nanocluster analysis in Al-0.9% Mg-1.0% Si-0.3% Cu (mass %) alloy using APT. The 10 different combinations of user-defined parameters ($D_{max}$, $N_{min}$, order) of the DBSCAN algorithm were applied to various analysis methods for cluster characterization. The main findings derived from these results and analyses are as follows.

- From the results of composition with size of clusters, it was confirmed that large clusters having alloy composition caused a high fraction of Balanced clusters (0.4≤Mg/solutes≤0.6). Probability calculations revealed that these large clusters having alloy composition contained large amounts of solute atoms in the matrix. These results suggest that careful analysis is required when clusters with a high fraction of alloy composition are detected.
- Two types of cluster volume measurements, $V_{l_g}$ and $V_{r_G}$, were considered to investigate the relationship between morphology and atomic density of clusters.
- It has been observed that as the morphology of the cluster deviates from a sphere, the atomic density ($\rho_{l_g}$) is overestimated. Especially, string-type clusters with the shortest axis is less than 0.1 nm caused the atomic density of 300 $nm^{-3}$ or higher.
- The atomic arrangement inside and outside of the clusters was investigated using the concentration profile. Non-ideal solutes concentration was observed, including cases where the similar solutes concentration inside the clusters with the matrix, and cases where the solute concentration in the matrix region was higher than the measured value. It was confirmed that those non-ideal solutes concentration inside the clusters and in the matrix region were caused by fragmented and connected clusters, respectively.

- The optimum parameters that do not cause unphysical clusters confirmed by the above results and analyzes was derived. The results of cluster analysis using optimum parameters were found to be in good agreement with the results of volume render and iso-concentration surface. Guidelines for optimizing user-defined parameters in DBSCAN algorithm for cluster analysis of Al-Mg-Si-Cu alloy was successfully proposed.

## References

[1] C. Cayron, L. Sagalowicz, L. Sagalowicz, P.A. Buffat, Structural phase transition in Al-Cu-Mg-Si alloys by transmission electron microscopy study on an Al-4 wt% Cu-1 wt% Mg-Ag alloy reinforced by SiC particles, Philos. Mag. A Phys. Condens. Matter, Struct. Defects Mech. Prop. 79 (1999) 2833–2851. https://doi.org/10.1080/01418619908212027.

[2] W.F. Miao, D.E. Laughlin, Effects of Cu Content and Preaging on Precipitation Characteristics in Aluminum Alloy 6022, 31 (2000) 361–371.

[3] D.J. Chakrabarti, D.E. Laughlin, Phase relations and precipitation in Al-Mg-Si alloys with Cu additions, Prog. Mater. Sci. 49 (2004) 389–410. https://doi.org/10.1016/S0079-6425(03)00031-8.

[4] C.D. Marioara, S.J. Andersen, T.N. Stene, H. Hasting, J. Walmsley, A.T.J. Van Helvoort, R. Holmestad, The effect of Cu on precipitation in Al-Mg-Si alloys, Philos. Mag. 87 (2007) 3385–3413. https://doi.org/10.1080/14786430701287377.

[5] M. Saga, Y. Sasaki, M. Kikuchi, Z. Yan, M. Matsuo, Effect of pre-aging temperature on the behavior in the early stage of aging at high temperature for Al-Mg-Si alloy, Mater. Sci. Forum. 217–222 (1996) 821–826. https://doi.org/10.4028/www.scientific.net/msf.217-222.821.

[6] M. Murayama, K. Hono, Pre-precipitate clusters and precipitation processes in Al–Mg–Si alloys, Acta Mater. 47 (1999) 1537–1548. https://doi.org/10.1016/S1359-6454(99)00033-6.

[7] K. Yamada, T. Sato, A. Kamio, Effects of Quenching Conditions on Two-Step Aging Behavior of Al-Mg-Si Alloys, Mater. Sci. Forum. 331–337 (2000) 669–674. https://doi.org/10.4028/www.scientific.net/MSF.331-337.669.

[8] T. Sato, High strength and high ductility aluminum alloys with controlled nano-clusters, J. Japan Inst. Light Met. 56 (2006) 592–601. https://doi.org/10.2464/jilm.56.592.

[9] A. Serizawa, S. Hirosawa, T. Sato, Three-Dimensional Atom Probe Characterization of Nanoclusters Responsible for Multistep Aging Behavior of an Al-Mg-Si Alloy, Metall. Mater. Trans. A. 39 (2008) 243–251. https://doi.org/10.1007/s11661-007-9438-5.

[10] M. Torster, H.S. Hasting, W. Lefebvre, C.D. Marioara, J.C. Walmsley, S.J. Andersen, R. Holmestad, The influence of composition and natural aging on clustering during preaging in Al-Mg-Si alloys, J. Appl. Phys. 108 (2010) 1–9. https://doi.org/10.1063/1.3481090.

[11] S. Pogatscher, H. Antrekowitsch, H. Leitner, D. Po, Influence of interrupted quenching on artificial aging of Al – Mg – Si alloys, 60 (2012) 4496–4505. https://doi.org/10.1016/j.actamat.2012.04.026.

[12] M.W. Zandbergen, Q. Xu, A. Cerezo, G.D.W. Smith, Study of precipitation in Al-Mg-Si alloys by Atom Probe Tomography I. Microstructural changes as a function of ageing temperature, Acta Mater. 101 (2015) 136–148. https://doi.org/10.1016/j.actamat.2015.08.017.

[13] A. Poznak, R.K.W. Marceau, P.G. Sanders, Composition dependent thermal stability and evolution of solute clusters in Al-Mg-Si analyzed using atom probe tomography, Mater. Sci. Eng. A. 721 (2018) 47–60. https://doi.org/10.1016/j.msea.2018.02.074.

[14] S.J. Andersen, C.D. Marioara, A. Frøseth, R. Vissers, H.W. Zandbergen, Crystal structure of the orthorhombic U2-$Al_4Mg_4Si_4$ precipitate in the Al–Mg–Si alloy system and its relation to the β′ and β″ phases, 390 (2005) 127–138. https://doi.org/10.1016/j.msea.2004.09.019.

[15] S.J. Andersen, C.D. Marioara, R. Vissers, A. Frøseth, H.W. Zandbergen, The structural relation between precipitates in Al-Mg-Si alloys, the Al-matrix and diamond silicon, with emphasis on the trigonal phase U1-$MgAl_2Si_2$, Mater. Sci. Eng. A. 444 (2007) 157–169. https://doi.org/10.1016/j.msea.2006.08.084.

[16] M.A. Van Huis, J.H. Chen, Phase stability and structural relations of nanometer-sized , matrix-embedded precipitate phases in Al – Mg – Si alloys in the late stages of evolution, 54 (2006) 2945–2955. https://doi.org/10.1016/j.actamat.2006.02.034.

[17] M.A. van Huis, J.H. Chen, M.H.F. Sluiter, H.W. Zandbergen, Phase stability and structural features of matrix-embedded hardening precipitates in Al-Mg-Si alloys in the early stages of evolution, Acta Mater. 55 (2007) 2183–2199. https://doi.org/10.1016/j.actamat.2006.11.019.

[18] M.K. Miller, T.F. Kelly, K. Rajan, S.P. Ringer, The future of atom probe tomography, Mater. Today. 15 (2012) 158–165. https://doi.org/10.1016/S1369-7021(12)70069-X.

[19] R.K.W. Marceau, Atomic-scale analysis of light alloys using atom probe tomography Atomic-scale analysis of light alloys using atom probe tomography, 0836 (2016). https://doi.org/10.1179/1743284715Y.0000000088.

[20] H. Zhong, P.A. Rometsch, X. Wu, L. Cao, Y. Estrin, Influence of pre-ageing on the stretch formability of Al-Mg-Si automotive sheet alloys, Mater. Sci. Eng. A. 697 (2017) 79–85. https://doi.org/10.1016/j.msea.2017.05.009.

[21] Z. Jia, L. Ding, L. Cao, R. Sanders, S. Li, Q. Liu, The Influence of Composition on the Clustering and Precipitation Behavior of Al-Mg-Si-Cu Alloys, Metall. Mater. Trans. A. 48 (2017) 459–473. https://doi.org/10.1007/s11661-016-3850-7.

[22] Y. Weng, Z. Jia, L. Ding, S. Muraishi, Q. Liu, Clustering behavior during natural aging and artificial aging in Al-Mg-Si alloys with different Ag and Cu addition, Mater. Sci. Eng. A. 732 (2018) 273–283. https://doi.org/10.1016/j.msea.2018.07.018.

[23] O. Engler, C.D. Marioara, Y. Aruga, M. Kozuka, O.R. Myhr, Effect of natural ageing or pre-ageing on the evolution of precipitate structure and strength during age hardening of Al–Mg–Si alloy AA 6016, Mater. Sci. Eng. A. 759 (2019) 520–529. https://doi.org/10.1016/j.msea.2019.05.073.

[24] Z.J. Cui, H.C. Jiang, D. Zhang, Y.Y. Song, D.S. Yan, L.J. Rong, Influence of Mn on the negative natural aging effect in 6082 Al alloy, Mater. Sci. Eng. A. 793 (2020) 139874. https://doi.org/10.1016/j.msea.2020.139874.

[25] W. Yu, H. He, W. Zhang, L. Li, C. Sun, Modulation of the natural aging effect on subsequent artificial aging in Al–Mg–Si aluminum alloys with alloying content～1wt% through temperature tuning, J. Alloys Compd. 814 (2020) 152277. https://doi.org/10.1016/j.jallcom.2019.152277.

[26] S. Zhu, H. Shih, X. Cui, C. Yu, S.P. Ringer, Acta Materialia Design of solute clustering during thermomechanical processing of AA6016 Al – Mg – Si alloy, 203 (2021). https://doi.org/10.1016/j.actamat.2020.10.074.

[27] W. Tu, J. Tang, L. Ye, L. Cao, Y. Zeng, Q. Zhu, Y. Zhang, S. Liu, L. Ma, J. Lu, B. Yang, Effect of the natural aging time on the age-hardening response and precipitation behavior of the Al-0.4Mg-1.0Si-(Sn) alloy, Mater. Des. 198 (2021) 109307. https://doi.org/10.1016/j.matdes.2020.109307.

[28] M.Y. Song, J.H. Kim, Microstructural evolution at the initial stage of two-step aging in an Al-Mg-Si alloy characterized by a three dimensional atom probe, Mater. Sci. Eng. A. 815 (2021) 141301. https://doi.org/10.1016/j.msea.2021.141301.

[29] H. Shishido, Y. Aruga, Y. Murata, C.D. Marioara, O. Engler, Evaluation of precipitates and clusters during artificial aging of two model Al–Mg–Si alloys with different Mg/Si ratios, J. Alloys Compd. 927 (2022) 166978. https://doi.org/10.1016/j.jallcom.2022.166978.

[30] Y. Aruga, M. Kozuka, Y. Takaki, T. Sato, Evaluation of Solute Clusters Associated with Bake-Hardening Response in Isothermal Aged Al-Mg-Si Alloys Using a Three-Dimensional Atom Probe, Metall. Mater. Trans. A. 45 (2014) 5906–5913. https://doi.org/10.1007/s11661-014-2548-y.

[31] Y. Aruga, M. Kozuka, Y. Takaki, T. Sato, Formation and reversion of clusters during natural aging and subsequent artificial aging in an Al–Mg–Si alloy, Mater. Sci. Eng. A. 631 (2015) 86–96. https://doi.org/10.1016/j.msea.2015.02.035.

[32] Y. Aruga, S.N. Kim, M. Kozuka, E. Kobayashi, T. Sato, Effects of cluster characteristics on two-step aging behavior in Al-Mg-Si alloys with different Mg/Si ratios and natural aging periods, Mater. Sci. Eng. A. 718 (2018) 371–376. https://doi.org/10.1016/j.msea.2018.01.086.

[33] Y. Aruga, M. Kozuka, T. Sato, Formulation of initial artificial age-hardening response in an Al-Mg-Si alloy based on the cluster classification using a high-detection-efficiency atom probe, J. Alloys Compd. 739 (2018) 1115–1123. https://doi.org/10.1016/j.jallcom.2017.10.220.

[34] A. Serizawa, S. Hirosawa, T. Sato, 3DAP Characterization and Thermal Stability of Nano-Scale Clusters in Al-Mg-Si Alloys, Mater. Sci. Forum. 519–521 (2006) 245–250. https://doi.org/10.4028/www.scientific.net/MSF.519-521.245.

[35] A. Serizawa, T. Sato, M.K. Miller, Effect of cold rolling on the formation and distribution of nanoclusters during pre-aging in an Al-Mg-Si alloy, Mater. Sci. Eng. A. 561 (2013) 492–497. https://doi.org/10.1016/j.msea.2012.10.070.

[36] S. Pogatscher, H. Antrekowitsch, H. Leitner, T. Ebner, P.J. Uggowitzer, Mechanisms controlling the artificial aging of Al – Mg – Si Alloys, Acta Mater. 59 (2011) 3352–3363. https://doi.org/10.1016/j.actamat.2011.02.010.

[37] J. Dykes, A.M. Maceachren, M.-J. Kraak, Exploring geovisualization, 1st editio, Pergamon, Ensched, 2005.

[38] M.K. Miller, R.G. Forbes, The Local Electrode Atom Probe, in: Atom-Probe Tomography, Springer US, Boston, MA, 2014: pp. 229–258. https://doi.org/10.1007/978-1-4899-7430-3_5.

[39] D. Vaumousse, A. Cerezo, P.J. Warren, A procedure for quantification of precipitate microstructures from three-dimensional atom probe data, Ultramicroscopy. 95 (2003) 215–221. https://doi.org/10.1016/S0304-3991(02)00319-4.

[40] M.K. Miller, E.A. Kenik, Atom probe tomography: A technique for nanoscale characterization, Microsc. Microanal. 10 (2004) 336–341. https://doi.org/10.1017/S1431927604040577.

[41] J.M. Hyde, E.A. Marquis, K.B. Wilford, T.J. Williams, A sensitivity analysis of the maximum separation method for the characterisation of solute clusters, Ultramicroscopy. 111 (2011) 440–447. https://doi.org/10.1016/j.ultramic.2010.12.015.

[42] E.A. Marquis, F. Vurpillot, Chromatic aberrations in the field evaporation behavior of small precipitates, Microsc. Microanal. 14 (2008) 561–570. https://doi.org/10.1017/S1431927608080793.

[43] T. Philippe, M. Gruber, F. Vurpillot, D. Blavette, Clustering and Local Magnification Effects in Atom Probe Tomography: A Statistical Approach, (2010) 643–648.

[44] D.J. Rose, On the Magnification and Resolution of the Field Emission Electron Microscope, Am. Inst. Phys. 215 (1956) 215–220.

[45] L.T. Stephenson, M.P. Moody, P. V. Liddicoat, S.P. Ringer, New techniques for the analysis of fine-scaled clustering phenomena within Atom Probe Tomography (APT) data, Microsc. Microanal. 13 (2007) 448–463. https://doi.org/10.1017/S1431927607070900.

[46] J.M. Cairney, K. Rajan, D. Haley, B. Gault, P.A.J. Bagot, P. Choi, P.J. Felfer, S.P. Ringer, R.K.W. Marceau, M.P. Moody, Ultramicroscopy Mining information from atom probe data, Ultramicroscopy. 159 (2015) 324–337. https://doi.org/10.1016/j.ultramic.2015.05.006.

[47] D.J. Larson, D.T. Foord, A.K. Petford-Long, T.C. Anthony, I.M. Rozdilsky, A. Cerezo, G.W.D. Smith, Focused ion-beam milling for field-ion specimen preparation: Preliminary

investigations, Ultramicroscopy. 75 (1998) 147–159. https://doi.org/10.1016/S0304-3991(98)00058-8.

[48] D.J. Larson, D.T. Foord, A.K. Petford-Long, A. Cerezo, G.D.W. Smith, Focused ion-beam specimen preparation for atom probe field-ion microscopy characterization of multilayer film structures, Nanotechnology. 10 (1999) 45–50. https://doi.org/10.1088/0957-4484/10/1/010.

[49] B. Gault, M.P. Moody, J.M. Cairney, S.P. Ringer, Atom Probe Microscopy, 1st ed., Springer US, 2012.

[50] B.P. Geiser, T.F. Kelly, D.J. Larson, J. Schneir, J.P. Roberts, M icroscopy M icroanalysis Spatial Distribution Maps for Atom Probe Tomography, (2007) 437–447.

[51] R.K.W. Marceau, G. Sha, R. Ferragut, A. Dupasquier, S.P. Ringer, Solute clustering in Al–Cu–Mg alloys during the early stages of elevated temperature ageing, Acta Mater. 58 (2010) 4923–4939. https://doi.org/10.1016/j.actamat.2010.05.020.

[52] D.J. Larson, T.J. Prosa, R.M. Ulfig, B.P. Geiser, T.F. Kelly, Local Electrode Atom Probe Tomography, 2013. https://doi.org/10.1007/978-1-4614-8721-0.

[53] M. Song, E. Kobayashi, J. Kim, Clustering evolution during low temperature aging and thermal stability during two-step aging in Al-Mg-Si alloys, J. Alloys Compd. 946 (2023) 169291. https://doi.org/10.1016/j.jallcom.2023.169291.

[54] A.K. Gupta, D.J. Lloyd, Study of precipitation kinetics in a super purity Al-0.8 pct Mg-0.9 pct Si alloy using differential scanning calorimetry, Metall. Mater. Trans. A. 30 (1999) 879–884. https://doi.org/10.1007/s11661-999-0081-1.

[55] C.S.T. Chang, J. Banhart, Low-Temperature Differential Scanning Calorimetry of an Al-Mg-Si Alloy, Metall. Mater. Trans. A. 42 (2011) 1960–1964. https://doi.org/10.1007/s11661-010-0596-5.

[56] C. Sin, T. Chang, Z. Liang, E. Schmidt, J. Banhart, Influence of Mg / Si ratio on the clustering kinetics in Al – Mg – Si alloys, 103 (2012) 955–961.

[57] J. Banhart, M.D.H. Lay, C.S.T. Chang, A.J. Hill, Kinetics of natural aging in Al-Mg-Si alloys studied by positron annihilation lifetime spectroscopy, 014101 (2011) 1–13. https://doi.org/10.1103/PhysRevB.83.014101.

[58] M.D.H. Lay, H.S. Zurob, C.R. Hutchinson, T.J. Bastow, A.J. Hill, Vacancy Behavior and Solute Cluster Growth During Natural Aging of an Al-Mg-Si Alloy, (2012). https://doi.org/10.1007/s11661-012-1257-7.

[59] V. Fallah, B. Langelier, N. Ofori-Opoku, B. Raeisinia, N. Provatas, S. Esmaeili, Cluster evolution mechanisms during aging in Al–Mg–Si alloys, Acta Mater. 103 (2016) 290–300. https://doi.org/10.1016/j.actamat.2015.09.027.

[60] H.S. Zurob, H. Seyedrezai, A model for the growth of solute clusters based on vacancy trapping, Scr. Mater. 61 (2009) 141–144. https://doi.org/10.1016/j.scriptamat.2009.03.025.

[61] H. Seyedrezai, D. Grebennikov, P. Mascher, H.S. Zurob, Study of the early stages of clustering in Al – Mg – Si alloys using the electrical resistivity measurements, 525 (2009) 186–191. https://doi.org/10.1016/j.msea.2009.06.054.

[62] M. Liu, Z. Wu, R. Yang, J. Wei, Y. Yu, P.C. Skaret, H.J. Roven, DSC analyses of static and dynamic precipitation of an Al–Mg–Si–Cu aluminum alloy, Prog. Nat. Sci. Mater. Int. 25 (2015) 153–158. https://doi.org/10.1016/j.pnsc.2015.02.004.

[63] R.K.W. Marceau, L.T. Stephenson, C.R. Hutchinson, S.P. Ringer, Ultramicroscopy Quantitative atom probe analysis of nanostructure containing clusters and precipitates with multiple length scales, Ultramicroscopy. 111 (2011) 738–742. https://doi.org/10.1016/j.ultramic.2010.12.029.

[64] A. Shariq, T. Al-kassab, R. Kirchheim, R.B. Schwarz, Exploring the next neighbourhood relationship in amorphous alloys utilizing atom probe tomography, 107 (2007) 773–780. https://doi.org/10.1016/j.ultramic.2007.02.030.

[65] A. Shariq, T. Al-kassab, R. Kirchheim, Studying nearest neighbor correlations by atom probe tomography (APT) in metallic glasses as exemplified for Fe 40 Ni 40 B 20 glassy ribbons, J. Alloys Compd. 512 (2012) 270–277. https://doi.org/10.1016/j.jallcom.2011.09.079.

**Tables**

Table 2.1 Summary of user-defined parameters ($D_{max}$ and $N_{min}$) used in several literatures using maximum separation method.

| Author | Year | Eqipment | $D_{max}$ | $N_{min}$ |
|---|---|---|---|---|
| Aruga et al. | 2014 | LEAP[c] 3000 | 0.75 | 10 |
| | 2015 | LEAP[c] 3000 | 0.75 | 10 |
| | 2018 | LEAP[c] 3000 | 0.75 | 10 |
| | | LEAP[c] 5000 | 0.65 | 20 |
| Engler et al. | 2018 | LEAP[c] 3000 | 0.75 | 10 |
| | 2019 | LEAP[c] 3000 | 0.75 | 10 |
| Serizawa et al. | 2006 | ECAP[a] | 0.6 | 20 |
| | 2008 | DLD[b] | 0.6 | 20 |
| Weng et al. | 2013 | LEAP[c] 4000 | 0.6 | 10 |
| | 2018 | LEAP[c] 4000 | 0.5 | 10 |
| Zandbergen et al. | 2015 | LEAP[c] | 0.65 | 10 |
| Zhu et al. | 2021 | LEAP[c] 4000 | 0.6 | 2 |
| Torsæter et al. | 2010 | ECAP[a] | 0.6 | 8 |
| Cui et al. | 2020 | LEAP[c] 5000 | 0.7 | 10 |
| Zhong et al. | 2017 | LEAP[c] 4000 | 0.7 | 10 |
| Shishido et al. | 2020 | LEAP[c] 5000 | 0.6 | 10 |
| Yu et al. | 2020 | LEAP[c] 5000 | 0.75 | 10 |
| Jia et al. | 2017 | LEAP[c] 4000 | 0.5 | 10 |
| Tu et al. | 2021 | LEAP[c] 4000 | 0.7 | 10 |
| Song et al. | 2021 | LEAP[c] 4000 | 0.75 | 10 |

[a] Energy compensated atom probe (ECAP)
[b] Imago Scientific Instruments (Madison, WI) APT with a delay-line detector (DLD)
[c] Local electrode atom probe (LEAP)

Table 2.2 The user-defined parameters determined from Figs. 1 and 2 at a given order ($k$) in NA and PA samples. The 1st to 5th-orders were applied to both samples.

| Conditions | Order ($k$) | $D_{max}$ | $N_{min}$ |
|---|---|---|---|
| NA sample | 1st | 0.62 | 6 |
| | 2nd | 0.87 | 13 |
| | 3rd | 0.96 | 22 |
| | 4th | 1.13 | 25 |
| | 5th | 1.18 | 22 |
| PA sample | 1st | 0.60 | 8 |
| | 2nd | 0.83 | 17 |
| | 3rd | 0.88 | 18 |
| | 4th | 1.05 | 28 |
| | 5th | 1.10 | 28 |

Table 2.3 Statistical data of clusters analyzed with different conditions in Table 2.

| Conditions | Order ($k$) | Number density ($10^{23}$ $m^{-3}$) | Guinier radius (nm) | Volume fraction (%) | Mg/solutes | Atomic density (Al) ($nm^{-3}$) |
|---|---|---|---|---|---|---|
| NA sample | 1st | 21.7 | 0.74 | 0.06 | 0.58 | 72.6 |
| | 2nd | 38.0 | 1.41 | 0.78 | 0.50 | 30.6 |
| | 3rd | 17.7 | 1.94 | 0.91 | 0.47 | 23.4 |
| | 4th | 28.5 | 2.51 | 3.57 | 0.50 | 24.7 |
| | 5th | 25.8 | 2.48 | 3.06 | 0.49 | 31.2 |
| PA sample | 1st | 16.3 | 0.76 | 0.05 | 0.37 | 55.1 |
| | 2nd | 31.2 | 1.52 | 0.82 | 0.45 | 21.1 |
| | 3rd | 28.5 | 1.54 | 0.75 | 0.46 | 23.4 |
| | 4th | 29.8 | 2.52 | 3.93 | 0.48 | 20.1 |
| | 5th | 20.3 | 3.03 | 4.24 | 0.47 | 22.3 |

Table 2.4 Number of clusters with different $D_{max}$ applied. The Dmax was taken from the literatures that used LEAP 4000 in Table 1. $N_{min}$ was set to 10 for all conditions.

| | Dmax | Nmin | Cluster count |
|---|---|---|---|
| NA | 0.50 | 10 | 0 |
| | 0.60 | 10 | 2 |
| | 0.70 | 10 | 8 |
| | 0.75 | 10 | 12 |
| PA | 0.50 | 10 | 1 |
| | 0.60 | 10 | 5 |
| | 0.70 | 10 | 23 |
| | 0.75 | 10 | 36 |

Table 2.5 Summary of *k*th-order DBSCAN resulting in unphysical clusters identified from composition with size, atomic density and concentration profile. Suitable candidates represent the conditions that the unphysical clusters are not confirmed.

| | Dmax | Nmin | Cluster count |
|---|---|---|---|
| NA | 0.50 | 10 | 0 |
| | 0.60 | 10 | 2 |
| | 0.70 | 10 | 8 |
| | 0.75 | 10 | 12 |
| PA | 0.50 | 10 | 1 |
| | 0.60 | 10 | 5 |
| | 0.70 | 10 | 23 |
| | 0.75 | 10 | 36 |

**Figures**

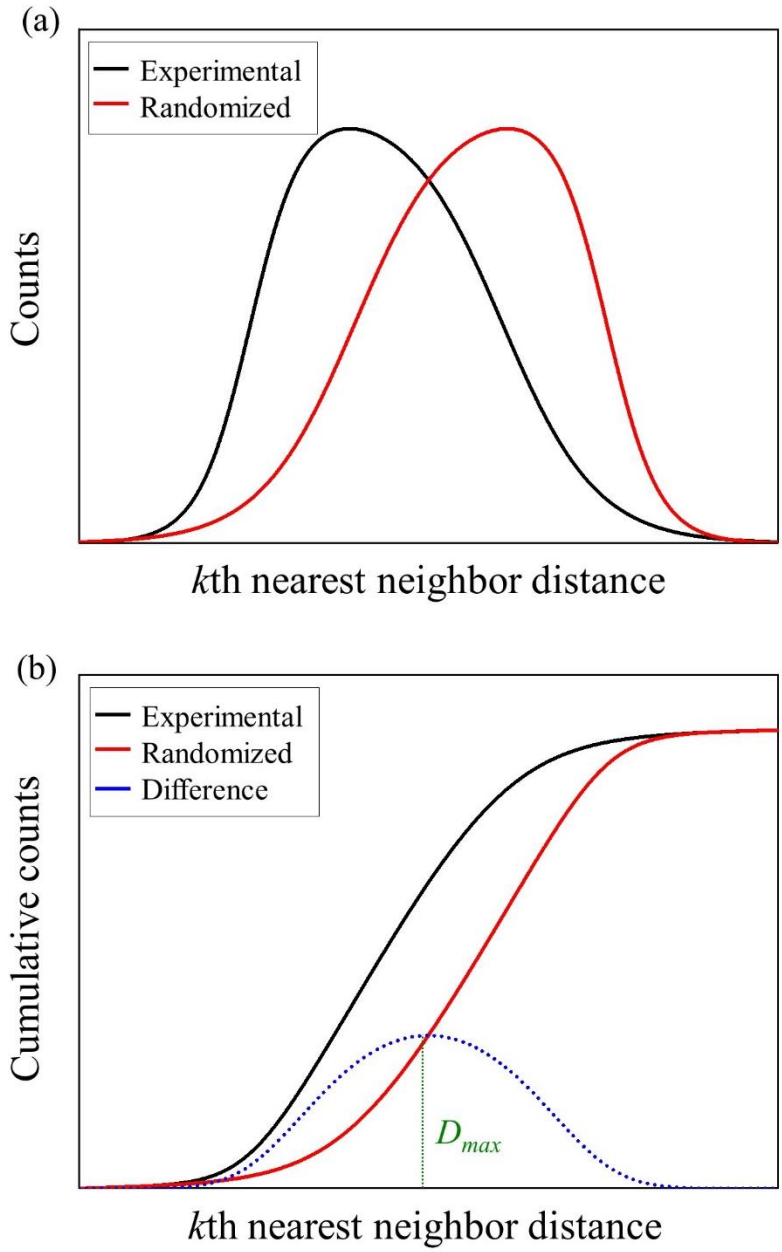


Figure 2.1 Determination of $D_{max}$ based on random labelling process. (a) shows *k*th-nearest neighbor distance (*k*NND) distribution. (b) represents the accumulated distribution of (a). The blue dotted line represents the difference between experimental and randomized datasets. The green dotted line indicates the maximum difference as determined by $D_{max}$ in a given order (*k*).

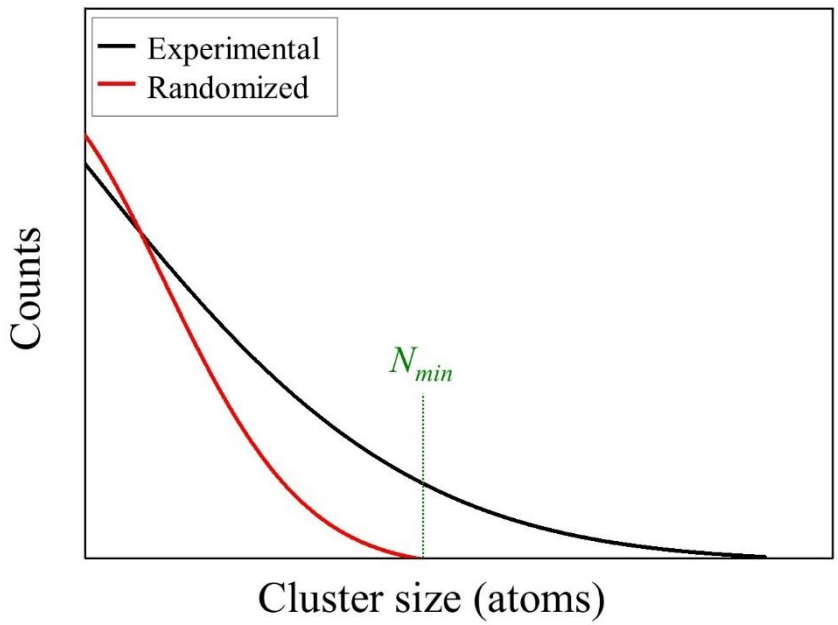


Figure 2.2 Determination of $N_{min}$ based on random labelling process. That figure shows the size distribution of experimental and randomized datasets at a given $D_{max}$ obtained from Fig. 1. The green dotted line indicates the point at which the randomized value first becomes zero. That point is determined by $N_{min}$.

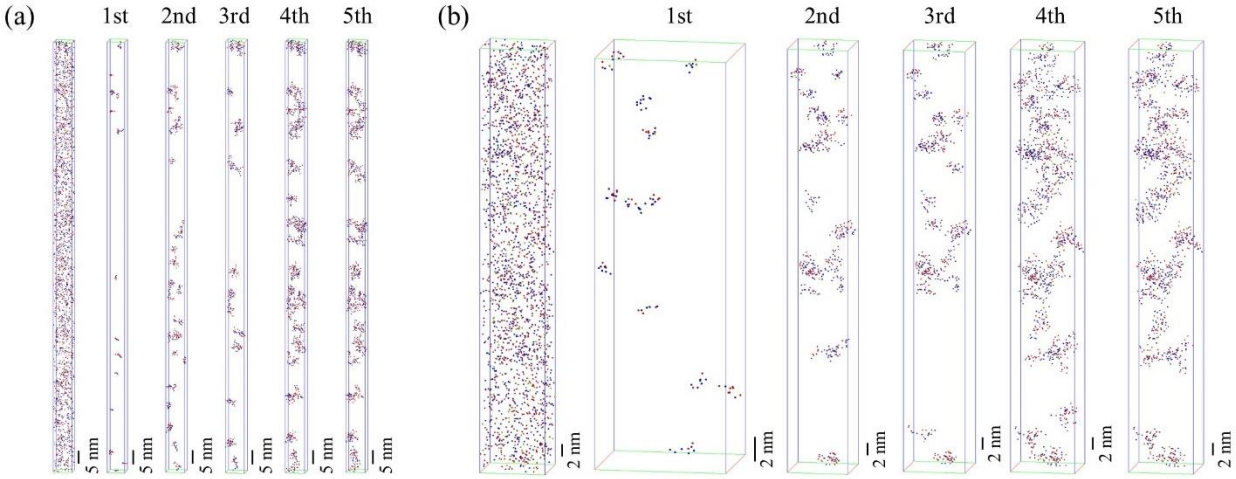


Figure 2.3 APT maps of (a) NA and (b) PA samples without and with 1st to 5th DBSCAN. Only solute atoms are shown. The red, blue and green dots represent the Mg, Si and Cu atoms, respectively. The size of dots does not reflect the actual atomic size.

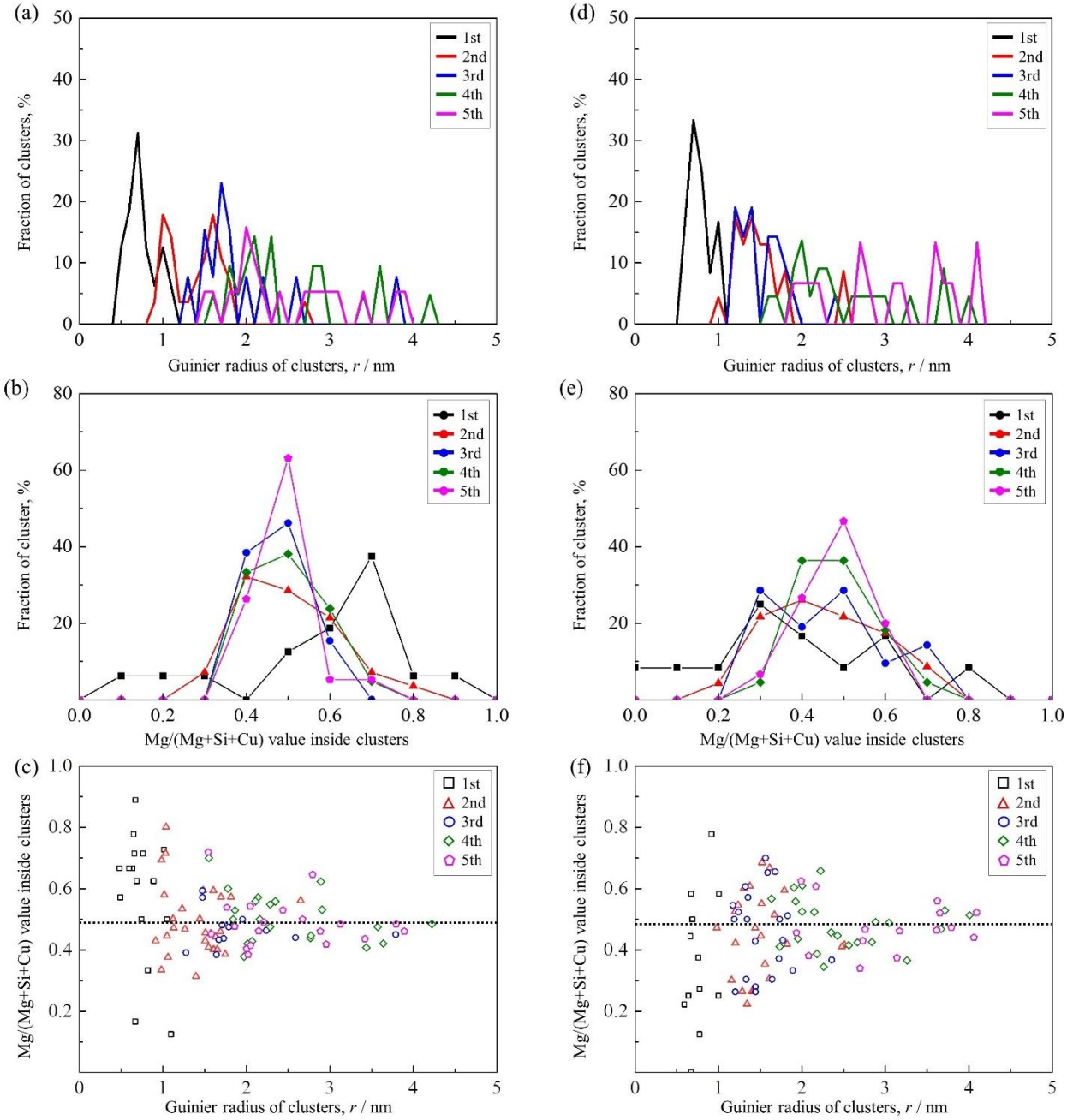


Figure 2.4 (a, d) Size distribution, (b, e) Mg fraction (Mg/solutes) distribution and (c, f) Mg fraction with size in (a, b, c) NA and (d, e, f) PA samples with different order (k) . The dashed lines in (c) and (f) indicate the measured Mg fraction of each sample.

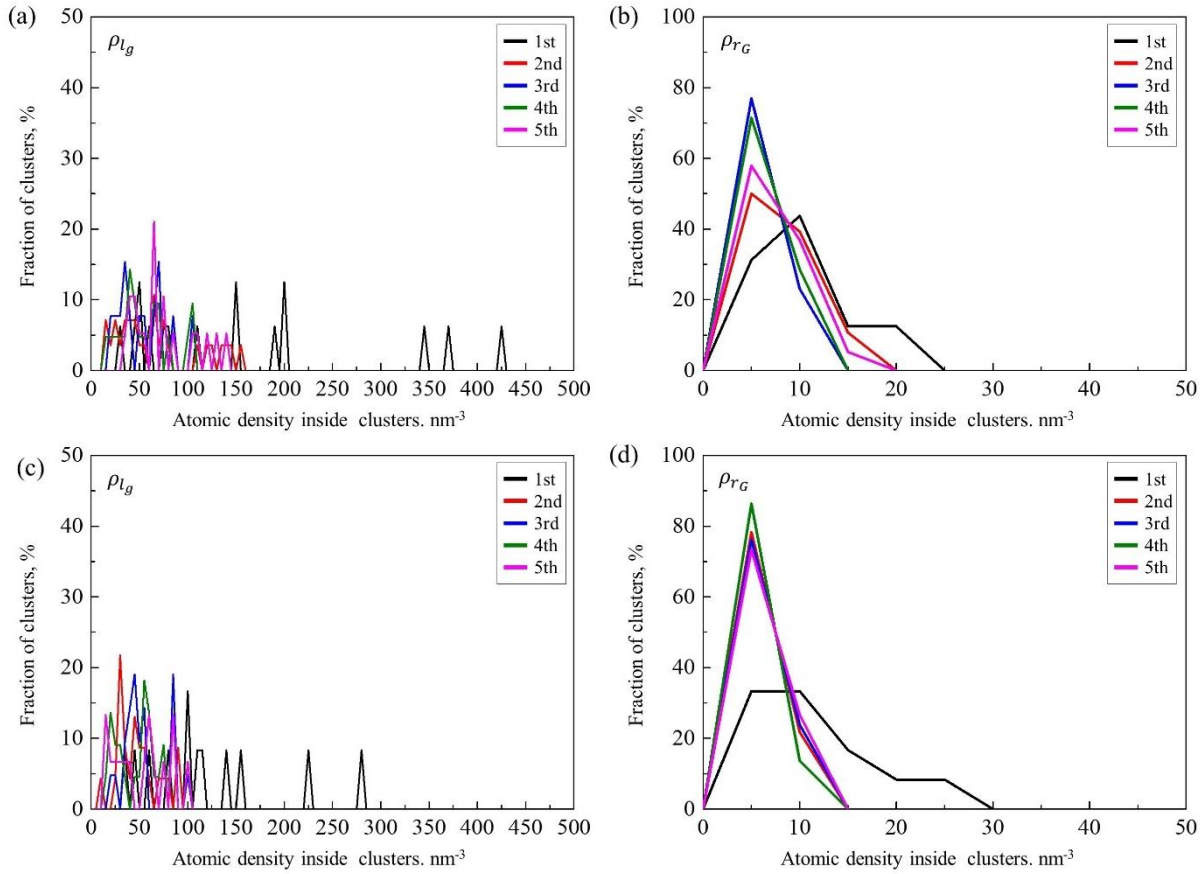


Figure 2.5 Distribution of atomic density ($\rho$) inside clusters of (a, b) NA and (c, d) PA samples based on (a, c) radius of gyration ($l_g$) and (b, d) Guinier radius ($r_G$). The details of $\rho_{l_g}$ and $\rho_{r_G}$ are elaborated in the manuscript. The step size of $\rho_{l_g}$ and $\rho_{r_G}$ are 5. The fraction of clusters (y axis) represents the number of clusters at each step.

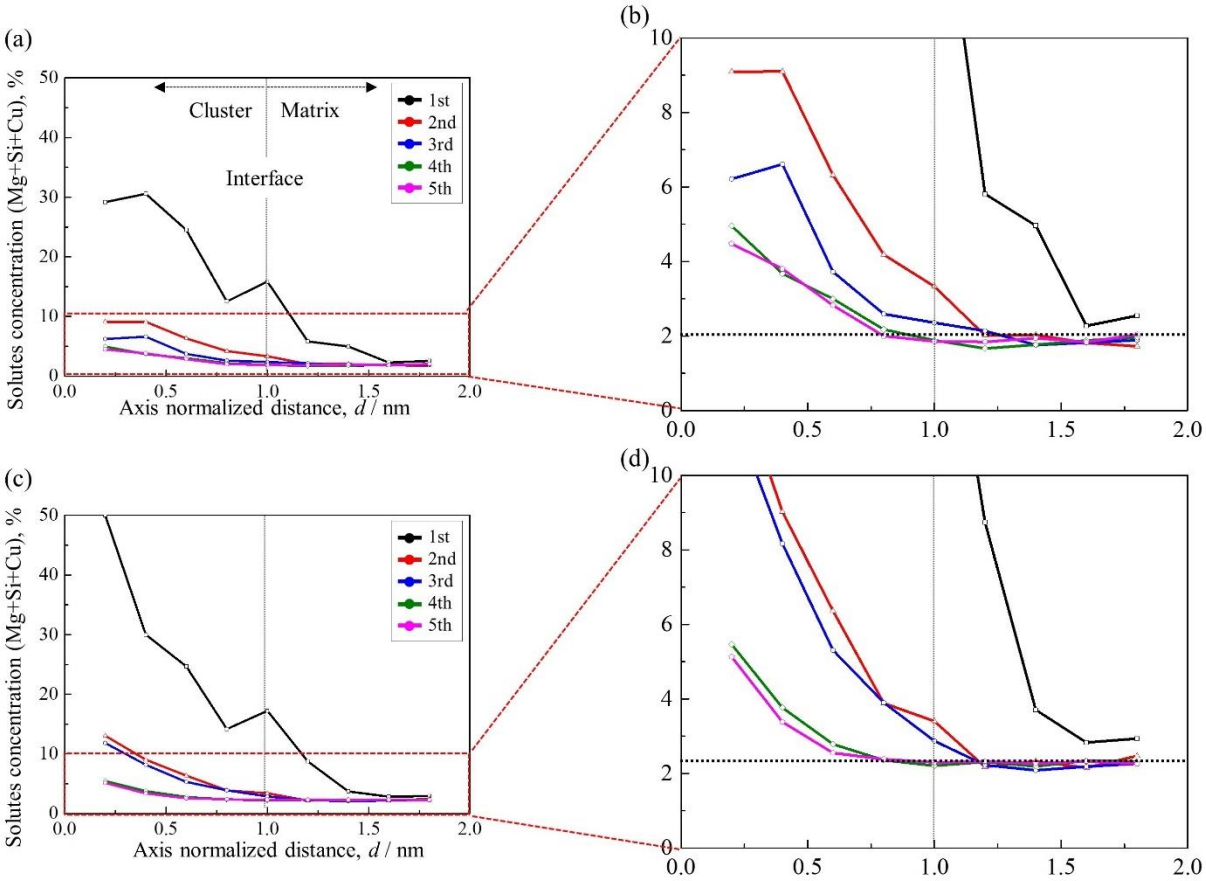


Figure 2.6 Concentration profile of clusters with different order (*k*) in (a, b) NA and (c, d) PA samples. The size of each cluster is normalized to *d*=1.0 nm based on maximum delta. Based on cluster-matrix interface (*d*=1.0), *d*<1.0 and d>1.0 nm represent the inside of a cluster and the matrix, respectively. (b) and (d) are enlarged images of red dashed lines in (a) and (c), respectively. The black dotted lines in (b, d) indicate the measured solutes concentration (Mg+Si+Cu).

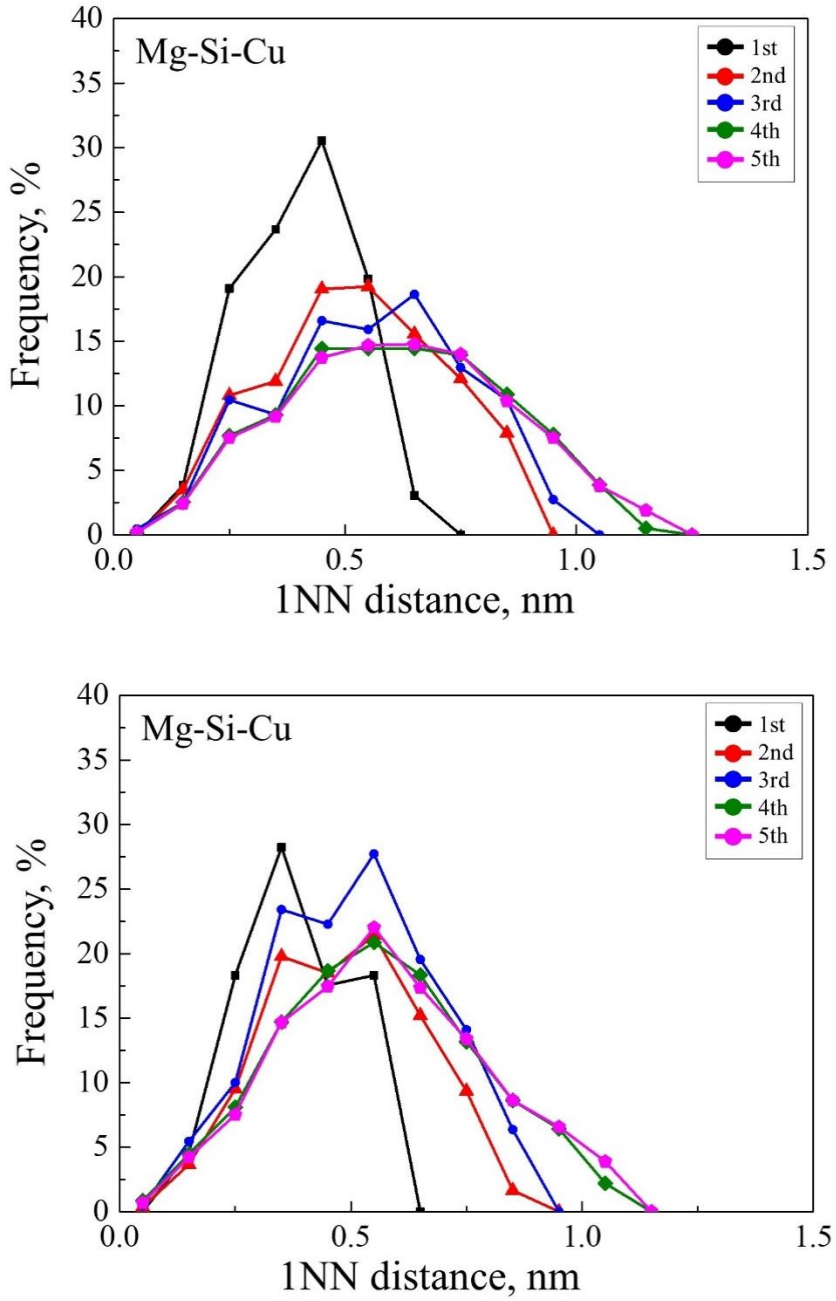


Figure 2.7 Distribution of first-nearest neighbor (1NN) distance of six solute pairs (Mg-Mg, Si-Si, Cu-Cu, Mg-Si, Mg-Cu and Si-Cu ) in (a) NA and (b) PA samples. Only solute atoms that make up the clusters were considered. The step size of 1NND was set to 0.1 nm.

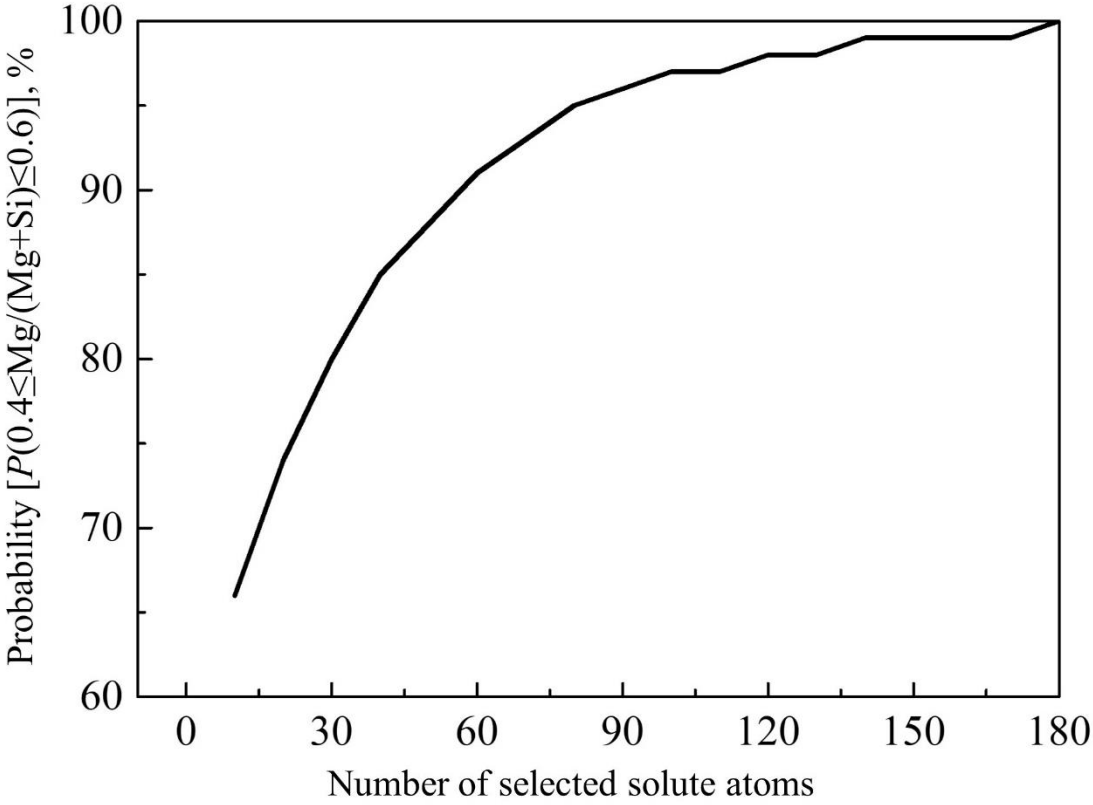


Figure 2.8 Probability of satisfying $P(0.4 \leq Mg/(Mg+Si) \leq 0.6)$ when selecting a given number of solute atoms (x-axis) from a total of 3500 solute atoms with Mg:Si=1:1. The probabilities are calculated from eq. (3) and (4).

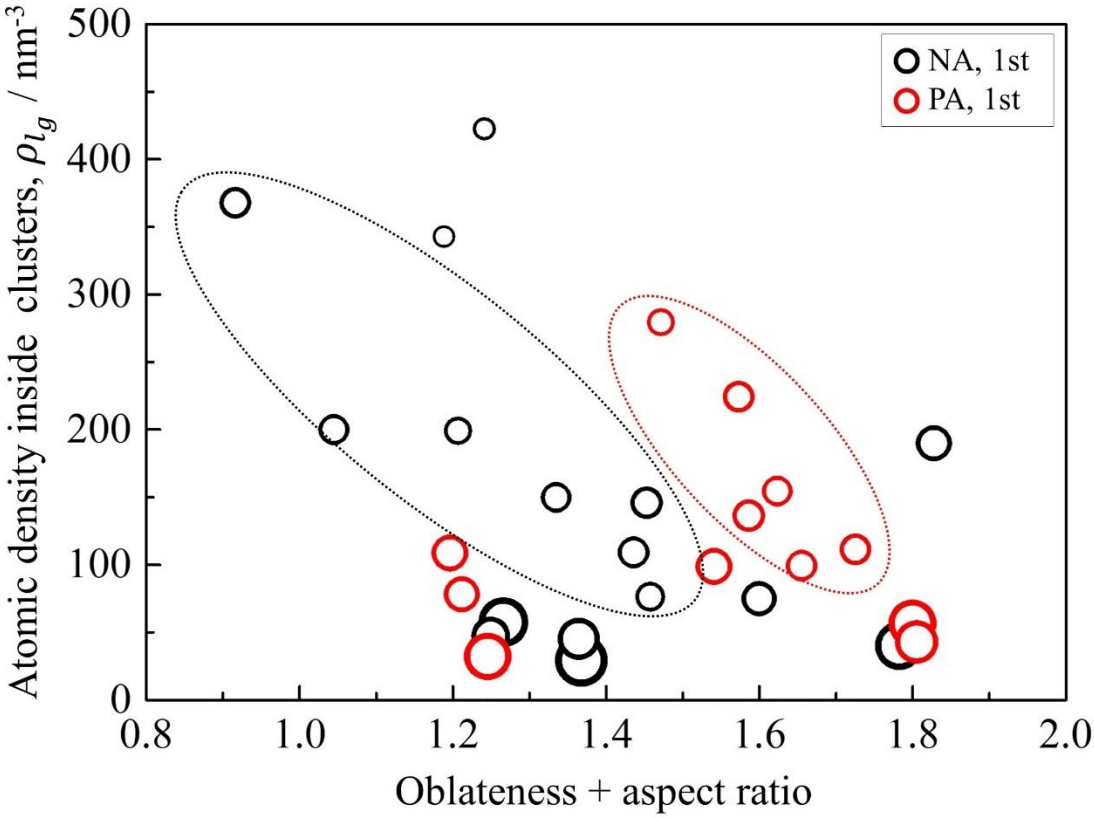


Figure 2.9 Relationship between atomic density inside clusters ($\rho_{l_g}$), ellipticity (oblateness + aspect ratio) and Guinier radius ($r_G$). The oblateness and aspect ratio are widely used for evaluating morphology of the clusters [Marceau_2011, Gault book]. The black and red circles represent the NA and PA samples applied 1st-order DBSCAN, respectively. The size of each circle indicates the $r_G$ of a cluster. The dotted line indicates the clusters with similar $r_G$.

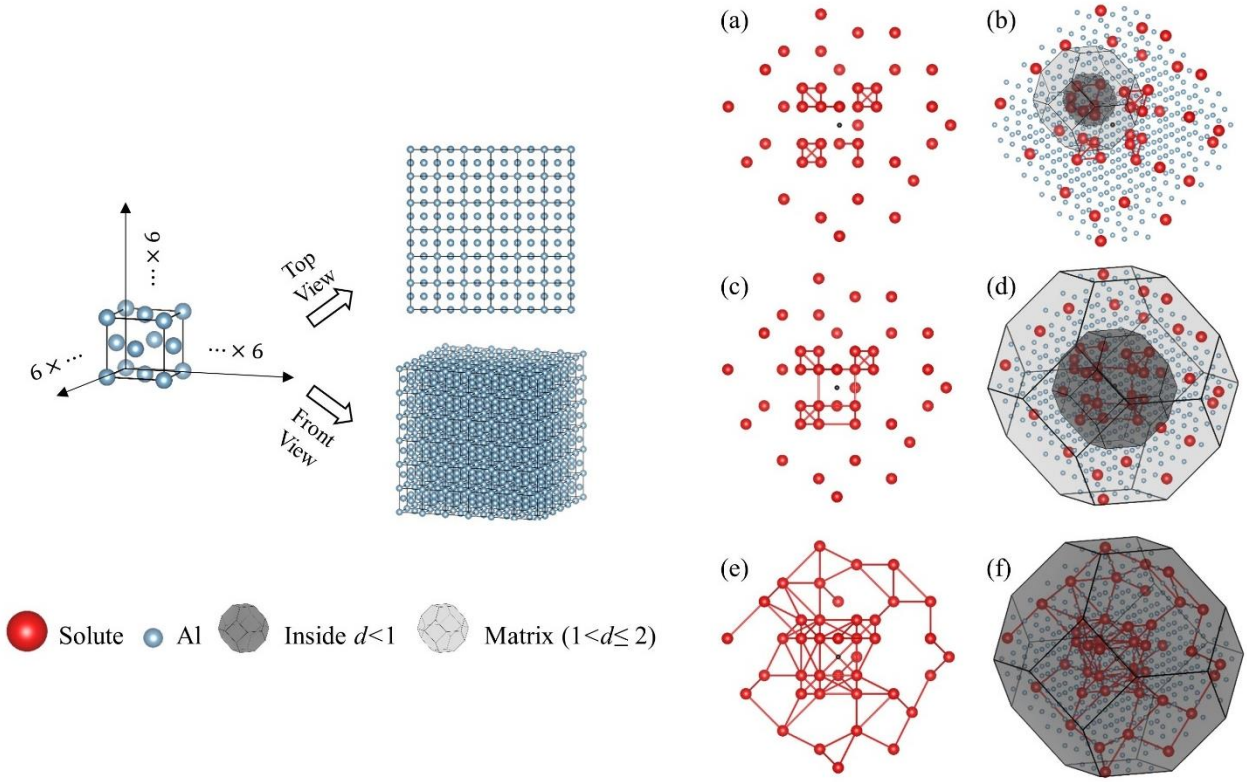


Figure 2.10 Schematic diagram of examples of the (a, b) under-fitted, (c, d) physical and (e, f) over-fitted cluster. (a, c, e) Top and (b, d, f) front views are prepared.. Only solute atoms are shown in top view to clearly show the bonds (red solid line) between solute atomsThe dark and light polyhedrons represent inside of a cluster ($d$<1) and matrix (1<$d$≤2), respectively.

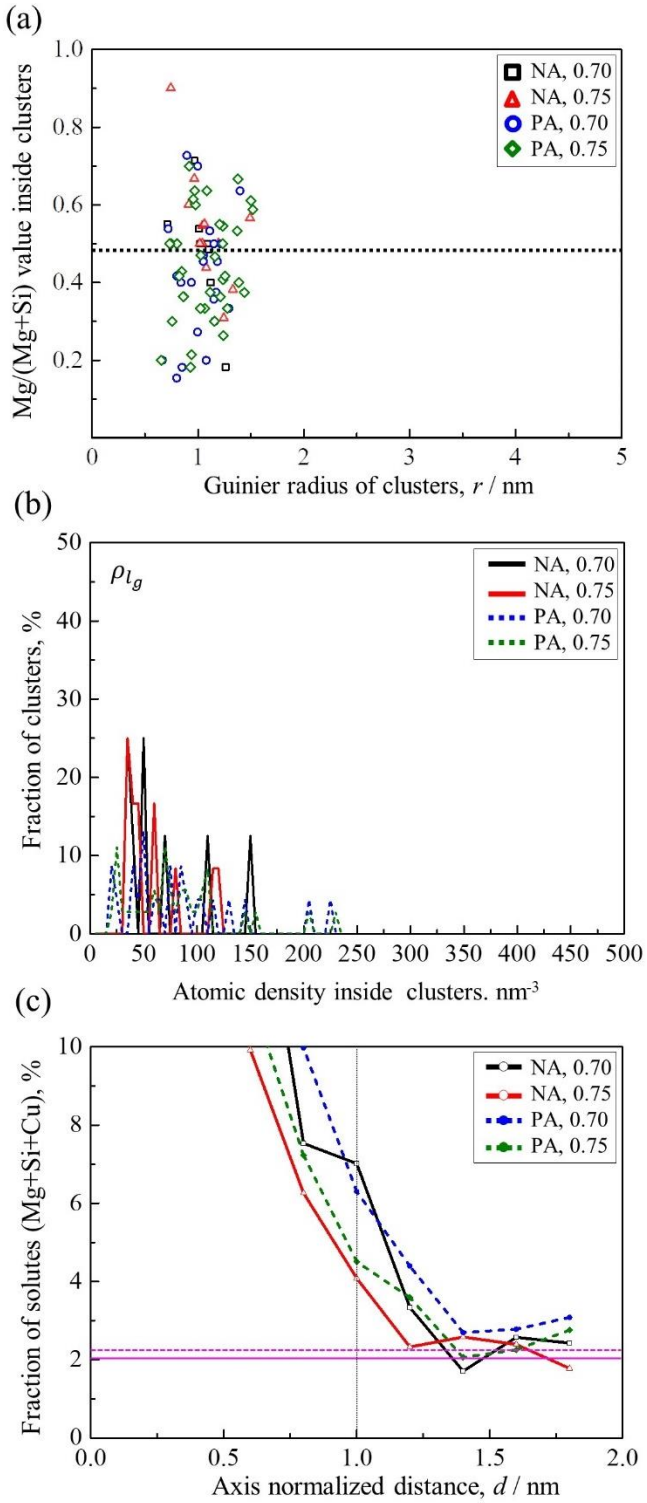


Figure 2.11 (a) Composition with size, (b) atomic density ($\rho_{l_g}$) and (c) concentration profile of NA and PA samples under $D_{max}$ = 0.70, 0.75 nm conditions in Table 4. (a), (b) and (c) are equal to the Fig. 4 c/f, Fig. 5 a/c and Fig. 6, respectively. The magenta lines indicate the measured fraction of solutes (Mg+Si+Cu) in NA (solid) and PA (dashed) samples.

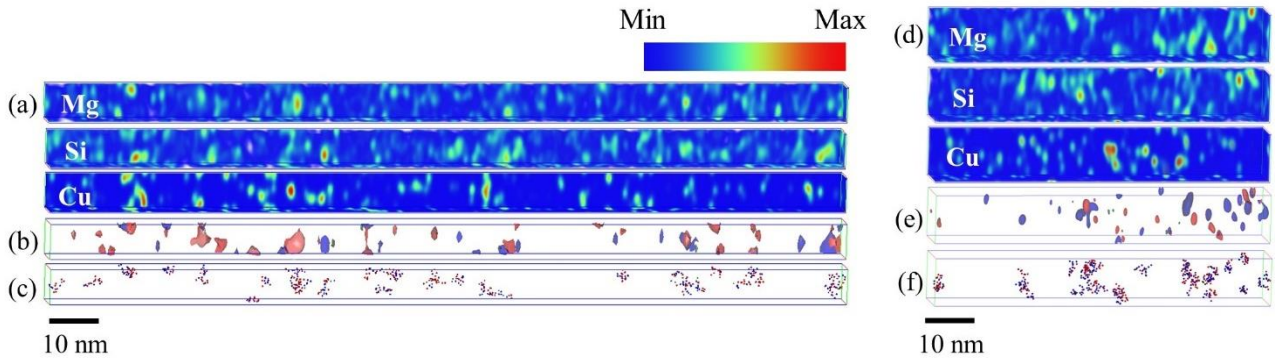


Figure 2.12 Comparison between (a, d) 3D volume render maps including Mg, Si and Cu, (b, e) isoconcentration surface and identified clusters by (c, f) DBSACN in (a, b, c) NA and (d, e, f) PA samples. The color scale represents concentration of each solute (Mg, Si, Cu) in a and d. The red, blue and green surfaces in b (e) are the isoconcentration surfaces at 2.2 (3.4) at.% Mg, 2.2 (3.4) at.% Si and 0.9 (1.2) at.% Cu, respectively. The values in blankets indicate the threshold values used to generate the isoconcentration surfaces of PA sample. The DBSCAN results come from 2nd order condition.

# Chapter 3

# Transition behavior of nanoclusters under sufficient low-temperature aging time in Al-Mg-Si alloy

## 3.1 Introduction

As discussed in Section 1.3.3, the two types of nanoclusters have different transition behavior. However, their transition behavior has not been fully understood yet. In the following, a new challenge for better understanding of the transition behavior of those nanoclusters is introduced.

Transmission electron microscope (TEM) is a powerful tool for analyzing the structure of fine precipitates in an Al-Mg-Si alloy. Studies on the analysis of fine precipitates by TEM have been reported [1–10]. However, the nanoclusters are hardly observable by TEM [1]. For this reason, various analyses using an atom probe tomography (APT) have been reported [11–27]. Torsæter et al. [16] confirmed that the Mg/Si ratio of the cluster formed at 100 °C is close to 1, and the cluster formed during natural aging has a Mg/Si ratio similar to the alloy composition. Fallah et al. [12] introduced that a certain level of composition must be reached for cluster growth, and their study indicated that cluster growth depends on aging temperature. So far, it is known that the cluster formed above and below at 70 °C have positive and negative effects on the two-step aging behavior, respectively [1,28]. Researchers have confirmed the formation temperature range of those nanoclusters based on the exothermal peak from differential scanning calorimetry (DSC) analysis [29–33]. The peaks of Cluster (1) and Cluster (2) were identified by separating the nanocluster formation peak in the DSC curve [31,34]. Figure 3.1

shows the peak separation using the Gaussian function. An as-quenched sample of Al-0.6% Mg-0.6% Si (mass%) alloy was analyzed with a heating rate of 10 °C/min. The peak temperatures of Cluster (1) and Cluster (2) were 41.5 and 78.0 °C, respectively. The peaks crossed at around 50 °C were confirmed. We therefore selected the pre-aging temperature as 50 °C, which is higher than the Cluster (1) peak temperature and overlaps with the Cluster (2) peak. Cluster is formed through binding the solute atoms and vacancies after migration of solute atoms, and diffusion is a function of temperature. The following equation [29] was used to normalize the aging time between at room temperature (25 °C), 50 and 100 °C.

$$T_1 = exp\left\{\frac{Q}{R}\left(\frac{1}{T_1} - \frac{1}{T_2}\right)\right\} \cdot T_2 \tag{3.1}$$

where $R$ is the gas constant, $T$ is the given temperature in Kelvin, and $Q$ is the activation energy for diffusion of Mg and Si atoms in Al. Serizawa et al. [29] used the reported activation energy for Mg ($Q$ = 130 kJ/mol [35,36]) since the activation energy value of Mg and Si are similar. We also applied the value for the activation energy for Mg in this study. Meanwhile, Cluster (2) was formed after pre-aging at 100 °C for 0.3 ks [37]. Provided the enough aging time on the basis of the normalized time is given, is the Cluster (2) able to form below 70 °C? When the aging temperature is low and the aging time is long enough, it is very important to reveal the cluster formation/transition behavior as a fundamental study. Previous studies focusing on such as effects of Mg/Si ratio of the alloys [16,22,24], solute content of the alloys [38], vacancy [8,39], microalloying element [20,27,40] on cluster evolution have been reported. However, so far, there is no attempt to investigate the transition behavior of clusters. Therefore, the cluster evolution during aging at 50 °C was investigated considering the normalized time.

### 3.2 Experimental procedure

We used Al-0.6% Mg-0.6% Si (mass%) alloys, which were provided by UACJ Corp. (Japan). In this study, the chemical composition is stated in mass%. The specimens were solution heat treated (ST) at 560 ℃ for 1.8 ks using a salt bath in which the powder of $KNO_3$ and $NaNO_3$ was mixed in a 1:1 ratio and then quenched in ice water at 0 ℃ for 0.06 ks. Artificial aging (AA) was carried out using an oil bath containing Silicone Oil (Shin-Etsu, KF-96 1000CS), and natural aging (NA) was conducted at around 25 ℃. The heat-treatment histories, namely, single aging (SA) and two-step aging (TSA), are summarized in Table 2. SA represents the artificial aging or natural aging after quenching. In this study, SA at room temperature, 50 and 170 ℃ is denoted as natural aging (NA), pre-aging (PA) and SA (170). The PA time was set to 0.06, 3.6 and 604.8 ks to investigate the clustering behavior with the different PA times. Two-step aging stands for the artificial aging at 170 ℃ after NA or PA. The two-step aging after NA and PA at 50 ℃ for 0.06, 3.6, and 604.8 ks are denoted as TSA (25, 604.8), TSA (50, 0.06), TSA (50, 3.6) and TSA (50, 604.8), respectively.

Differential scanning calorimetry (DSC 204 F1 phoenix, NETZSCH) was used to perform a thermal analysis under a nitrogen gas atmosphere using ultra high purity nitrogen (99.999%). DSC running started at -50 ℃ using liquid nitrogen to stabilize the data and was heated to 500 ℃ at a heating rate of 10 ℃/min. Specimens for DSC analysis were prepared with a weight of 40 ± 0.05 mg and a disc height of 1 mm. The prepared specimens were placed in a pure aluminum crucible with a pierced lid. The hardness measurements were performed by a micro Vickers hardness test (HV-113, Mitsutoyo Corp.) under a load of 200 g and a dwell time of 10 s. The average hardness results were obtained from five measurements excluding the minimum and maximum values in seven measurements. Specimens for hardness measurements were prepared with a size of 10 × 10 × 1 mm (height). Wires with a diameter of 1.0 mm and a gage

length of 300 mm were prepared for the electrical resistivity measurement. The electrical measurements were conducted by a four-probe method in a container filled with liquid nitrogen (-196 °C) so that the scattering from lattice vibration (the so-called thermal scattering effect) could be ignored. The electrical resistivity is obtained by the following equation:

$$\rho = \frac{V_m}{I_{st}} \times \frac{A}{L} [\Omega m] \tag{3.2}$$

where $\rho$, $V_m$, $I_{st}$, $A$ and $L$ represent the electrical resistivity, electric potential difference (measurement value, mV), applied constant current, cross section area of a specimen and the gage length, respectively. The specimens for the atom probe tomography (APT) were prepared by a focused ion beam (Helios NanoLab 600, FEI). The cryo-focused ion beam (FIB) with a liquid nitrogen was utilized to prevent room temperature exposure of the specimen and a temperature increase during operation of the FIB. The ion source for FIB milling was conducted by gallium ions, which may lead to intermixing of phases and regions of different compositions or even turn crystalline regions amorphous [41,42]. A capping process with platinum was performed during FIB milling to minimize gallium implantation. The clustering analysis was conducted using an atom probe tomography (LEAP 4000X HR™, CAMECA instruments Inc.) in the voltage pulsed mode with a voltage pulse fraction of 20% and an operation temperature of about -223 °C in a vacuum of up to 3.8 x $10^{-11}$. Data reconstruction and visualization were carried out using the analysis software Integrated Visualization and Analysis Software (IVAS 3.8.0). Crystallographic artifacts in APT reconstructions create regions of low and/or high atomic densities [43]. A technique based on the k-th nearest neighbor (*k*NN) point density has been studied to remove such artifacts [44]. However, a clear solution has not yet been presented. Therefore, the crystallographic poles and zone lines were excluded. The maximum separation method [45,46] was applied for the cluster analysis. The maximum

separation distance between atoms ($D_{max}$) and the minimum number of atoms ($N_{min}$) were chosen as 0.75 nm and 10 solute atoms, respectively.

## 3.3 Results

### 3.3.1 Indirect analyses with the PA time

In this study, for the convenience of classifying clusters, clusters formed at a specific temperature and time are expressed as $Cluster_{time(ks)}^{temp.}$. For example, clusters formed during NA are represented as $Cluster^{25}$, and clusters formed by NA for 604.8 ks are represented as $Cluster_{604.8}^{25}$. Figure 3.2 shows the DSC results for as-quenched (AQ) specimens and different PA times, 0.06 to 604.8 ks. The peak for nanocluster formation, nanocluster dissolution, β″ and β′ were previously reported [47–49]. The peak area of nanocluster formation in the range 0-150 ℃ decreased due to the cluster formation with an increasing PA time, and the peak area of the nanocluster dissolution around at 220 ℃ increased as the PA time increased. The area of the endothermal peak was proportional to the amount of cluster dissolution. Thus, the amount of cluster formation increased with an increasing PA time and those clusters easily dissolved during DSC running as the PA time increased.

Figure 3.3(a) shows the hardness results of single aging (SA) and two-step aging (TSA) at 170 ℃ with different PA times. The hardness increased during PA due to the $Cluster^{50}$ formation. The hardness after PA at 50 ℃ for 0.06, 3.6 and 604.8 ks was 44.5, 49.9 and 67.9 HV, respectively. The hardness after PA at 50 ℃ increased as the PA time increased. The different values of the obtained hardness during the two-step aging from before isothermal aging at 170 ℃, ΔHV, are shown in Fig. 3.3(b) to investigate the effect of PA time on the early stage of two-step aging behavior. We confirmed the hardness decrease at the early stage of two-

step aging when PA was carried out for 604.8 ks. This decrease in hardness was due to the fact that the decrease in hardness due to the dissolution of $Cluster^{50}$ was greater than the increase in hardness due to the formation of precipitates. Meanwhile, the hardness increased after two-step aging for 1.2 ks since the precipitate formation was more pronounced than that of dissolution of $Cluster^{50}$. $\Delta$HV represents the difference values of the obtained hardness during the two-step aging from before isothermal aging at 170 °C. $\Delta$HV at the two-step aging for 1.2 ks TSA (50, 0.06), TSA (50, 3.6) and TSA (50, 604.8) are identified as 4.6, 3.2 and -3.2 HV, respectively. Meanwhile, the hardness increases of 14.1 HV were confirmed for the single aging at 170 °C for 1.2 ks. That is, the degree of hardness increased during aging at 170 °C for 1.2 ks, and the age-hardening response decreased with an increasing PA time. This indicated that $Cluster^{50}$ suppressed the precipitate formation during two-step aging.

The results of electrical resistivity with the different heat-treatment histories are displayed in Fig. 3.4. Electrical resistivity increases during PA due to formation of the $Cluster^{50}$. Electrical resistivity during PA increases with an increasing PA time. These results confirm that the decrease in electrical resistivity at the early stage of isothermal aging at 170 °C occurs only in the case of TSA (50, 604.8). This phenomenon is related to dissolution of the $Cluster^{50}$ and is in good agreement with the hardness results of Fig. 3.3.

### 3.3.2 Comparison of NA and PA for 604.8 ks

Figure 3.5 shows the hardness results during NA and PA at 50 °C. Black and red lines represent the NA and PA at 50 °C, respectively. The hardness increased due to the cluster formation during NA and PA regardless of the temperature. The hardness of PA was always higher than that of NA. The increased hardness values for NA and PA at 50 °C for 604.8 ks

were confirmed as 20.9 and 27.7 HV, respectively. Note that the cluster formation accelerated during PA at 50 ℃.

Figure 3.6 shows the DSC results after NA and PA at 50 ℃ for 604.8 ks. The nanocluster dissolution peak was observed in both results. We calculated this area of the endothermal peak. The peak areas marked as dashed lines after NA and PA at 50 ℃ for 604.8 ks were 0.07 and 0.15 $J \cdot g^{-1}$, respectively. The peak area after PA at 50 ℃ for 604.8 ks was two times larger than that after NA for 604.8 ks. We confirmed a greater amount of dissolution for $Cluster^{50}$ than for $Cluster^{25}$.

Figure 3.7(a) shows the two-step aging (TSA) behavior after NA and PA at 50 ℃ for 604.8 ks. The black and red lines are TSA (25, 604.8) and TSA (50, 604.8), respectively. TSA (50, 604.8) is the same as in Fig. 3.3, and it was used to compare with TSA (25, 604.8). The hardness increased due to cluster formation during NA and PA at 50 ℃ for 604.8 ks and the increase in hardness during PA at 50 ℃ over that of NA was clarified. Figure 3.7(b) is the result of $\Delta$HV, and $\Delta$HV was obtained in the same way as in Fig. 3.3(b). The different values of the minimum hardness during the two-step aging from before isothermal aging at 170 ℃ and $\Delta HV_m$, for TSA (25, 604.8) and TSA (50, 604.8) are identified as 0.1 and -17.2 HV, respectively. At the early stage of two-step aging, TSA (25, 604.8) delayed the hardness increase, but TSA (50, 604.8) decreased the hardness. The details of the different phenomena are elaborated in the discussion session.

### 3.3.3 Cluster characteristics formed during NA and PA for 604.8 ks

The characteristics of $Cluster^{25}_{604.8}$ and $Cluster^{50}_{604.8}$ are presented as visualization and statistical data using APT. Figure 3.8 shows the APT maps of $Cluster^{25}_{604.8}$ and $Cluster^{50}_{604.8}$.

Figure 3.8(a) shows the distribution of all solute atoms in the region of interest. The red and blue spheres are Mg and Si atoms, respectively. All spheres were equalized to the same size. Figure 3.8(b) shows the distribution of clusters analyzed by applying the maximum separation method. The x,y and z axis lengths of the analyzed regions for all solute atoms and clusters are about 7 ×13 × 51 and 6 × 13 × 45 (nm), respectively. The analyzed area for all solute atoms and clusters are slightly different since the regions where the clusters have not been analyzed were excluded. We analyzed the size distribution, chemical composition and atomic density of the clusters. Cluster size is expressed as the Guinier radius ($r_G$) [50]. Number density is the number of clusters per unit volume (1 $nm^3$). For the convenience of checking the Mg/Si ratio of the clusters, it was represented as Mg/(Mg+Si) value to show symmetry based on Mg:Si = 1:1. The atomic density is a value obtained by dividing the number of clusters by the volume of the cluster. Figure 3.9 shows the results of the APT analysis of $Cluster_{604.8}^{25}$ and $Cluster_{604.8}^{50}$. Figure 3.9(a) represents the fraction of clusters with the cluster size. There is no significant difference in the size distribution between $Cluster_{604.8}^{25}$ and $Cluster_{604.8}^{50}$, and more than 95% of both clusters are distributed in 0.4-1.0 nm. Note that clusters corresponding to $r_G \leq 1$ nm are mainly formed at low temperature aging below 50 °C. Figure 3.9(b) displays the atomic density inside clusters with the cluster size. The atomic density of $Cluster_{604.8}^{25}$ and $Cluster_{604.8}^{50}$ is distributed in the range 4.5-47.4 and 4.9-31.4 $nm^{-3}$, respectively. Regardless of the aging temperature, as the cluster size increases, the atomic density tends to decrease and is observed to approach below 10 $nm^{-3}$. Figure 3.9(c) shows the accumulated fraction of clusters with the Mg/(Mg+Si) value inside the clusters. In this study, Mg/(Mg+Si) < 0.4 is expressed as a Si-rich cluster, 0.4 ≤ Mg/(Mg+Si) ≤ 0.6 is a Balanced cluster, and Mg/(Mg+Si) is a Mg-rich cluster. Both $Cluster_{604.8}^{25}$ and $Cluster_{604.8}^{50}$ have the highest proportion of Balanced clusters.

The Si-rich cluster fraction is similar, but the Mg-rich cluster fraction of $Cluster_{604.8}^{50}$ is higher than that of $Cluster_{604.8}^{25}$. Figure 3.9(d) is the Mg/(Mg+Si) value with the cluster size. Mg/(Mg+Si) of $Cluster_{604.8}^{25}$ and $Cluster_{604.8}^{50}$ are distributed in the range 0.20-0.90 and 0.33-1.00, respectively. Overall, the Mg/(Mg+Si) of $Cluster_{604.8}^{50}$ is higher than that of $Cluster_{604.8}^{25}$. In particular, the Mg-enriched cluster (Mg/(Mg+Si) ≥ 0.7) in Fig. 3.9(d) was analyzed only in $Cluster_{604.8}^{50}$ when the size of the cluster was over the average size of 0.6 nm. Table 3.3 presents the statistical data of the characteristics of $Cluster_{604.8}^{25}$ and $Cluster_{604.8}^{50}$. The statistical data are the average values of all the clusters. The average size, number density, atomic density, and Mg/(Mg+Si) of $Cluster_{604.8}^{25}$ were 0.63 nm, 18.9 $10^{23}$ $m^{-3}$, 26.5 $nm^{-3}$, and 0.54, respectively. The average size, number density, atomic density, and Mg/(Mg+Si) of $Cluster_{604.8}^{50}$ were 0.68 nm, 38.6 $10^{23}$ $m^{-3}$, 21.1 $nm^{-3}$, and 0.58, respectively. The number density and Mg/(Mg+Si) of $Cluster_{604.8}^{50}$ are higher than that of $Cluster_{604.8}^{25}$ and the cluster sizes are similar.

## 3.4 Discussion

### 3.4.1 Clusters formed during PA

Cluster (1) is formed during natural aging and does not transform to the main strengthening phase, β″ [29,51,52], which causes a '*negative effect of the two-step aging*' phenomenon and reduces the mechanical properties during the two-step aging [52–54]. The effect of Cluster (1) on the two-step aging changes with the NA time. As the NA time increases, the age-hardening response at the early stage of two-step aging decreases and NA longer than a specific time causes a decrease in the hardness at the early stage of two-step aging [55,56]. Meanwhile, according to a DSC analysis of the Al-Mg-Si alloy, an exothermal peak is formed at around 0-

150 ℃ due to the nanocluster formation [29–33]. Reduction of this exothermal peak area is caused by the decrease in the amount of solute atoms and vacancies due to nanocluster formation [32,57]. The hardness decrease at the early stage of two-step aging is related to the dissolution of Cluster (1) [22]. Dissolution of Cluster (1) causes the endothermal peak before the β″ peak during DSC analysis [49]. Those change in hardness and DSC with NA time is also confirmed in PA at 50 ℃. As the PA time increases, the peak area of nanocluster formation decreases and the endothermal peak area increases (see Fig. 3.2). The hardness during PA at 50 ℃ increases, and the age-hardening response at the early stage of two-step aging declines with an increasing PA time (see Fig. 3.3). The hardness of TSA (50, 604.8) decreases at the early stage of two-step aging (see Fig. 3.3). Our results also confirm that the electrical resistivity decreases at the initial stage of two-step aging (see Fig. 3.4). The electrical resistivity of an age-hardenable alloy is affected by three kinds of scattering mechanisms, namely, thermal scattering ($\rho_0$), solute atom scattering ($\rho_m$), which is controlled by solute concentration in the matrix, and precipitate scattering ($\rho_p$) [57]. Among them, $\rho_p$ is strongly affected by a variance in precipitates with the number density and size during isothermal aging [57]. Consequently, $\rho_p$ can be simply expressed as follows.

$$\rho_p = N_p \times G_p(\mu, \sigma) \tag{3.3}$$

where $N_p$ and $G_p(\mu, \sigma)$ represent the number density of precipitates per unit volume and the average scattering power resulting from one precipitate, respectively. $G_p(\mu, \sigma)$ is proportional to the average size of the precipitates. A previous study [13] confirmed a decrease in both the number density and the average size of the clusters during two-step aging after NA for one month. Referring back to Fig. 3.4, the decrease in electrical resistivity at the early stage of isothermal aging clearly indicates the dissolution of $Cluster^{50}$. Therefore, we conclude that Cluster (1) is dominantly formed during the PA at 50 ℃. On the other hand, as shown in Fig.

3.1, when the cluster peak was separated by the method of the Gaussian function, we assumed that Cluster (1) and Cluster (2) could be generated simultaneously near 50 °C. Therefore, in the analysis of cluster formation, the limitation of peak separation using Gaussian functions will be discussed in depth.

DSC analysis is generally accepted for characterizing the clustering behavior in Al-Mg-Si alloys [32,34,58–63]. The shape of the peak is affected by the heating rate, thermal conductivity and the mass of the specimen, etc. [64]. Since the peak area is not affected even if the shape of the peak changes [64], it is suitable for nanocluster analysis. The Gaussian function was utilized to investigate the peaks of Cluster (1) and Cluster (2) [31,34]. The nanocluster formation peak was separated using the Gaussian function (see Fig. 3.1), and the Gaussian function is as follows.

$$y = y_0 + \frac{A}{\omega\sqrt{2/\pi}} e^{-\frac{2(x-x_0)^2}{\omega^2}} \tag{3.4}$$

where $y_0$ is the baseline offset, $A$ is the area under the curve from the baseline, $x_0$ is the center of the peak, and $\omega$ is the width of the peak at half height. The Gaussian function shows a symmetrical bell-like shape centering around $x_0$. The curve shape is controlled by determination of the shape-controlling parameters, namely, $A$, $x_0$ and $\omega$. The peaks of Cluster (1) and Cluster (2) were identified as a result of peak separation (see Fig. 3.1). We calculated the peak area up to 50 °C. The peak areas of Cluster (1) and Cluster (2) up to 50 °C were 0.044 and 0.021 $J \cdot g^{-1}$, respectively. The area of the exothermal peak is related to the volume fraction of the formed phase. It seems that Cluster (2), which has half the volume fraction compared with Cluster (1), is formed during PA at 50 °C based on the peak separation from the DSC result. However, Cluster (1) is dominantly formed during the PA at 50 °C according to hardness and electrical resistivity measurements. That discrepancy comes from the following two points.

Firstly, there is a limitation to determining the type of cluster through peak separation by applying the Gaussian function from the DSC result. The Gaussian function assumes a symmetrical curve regardless of shape-controlling parameters. Moreover, curve fitting using the Gaussian function is performed based on non-linear least squares. The shape-controlling parameters are determined by an iterative process such as the Levenberg-Marquardt method, which minimizes a figure-of-merit function [65]. However, that process finds locally suitable parameters, not necessarily exact values [65]. For those reasons, it is difficult to divide the type of clusters with quantitative information through the peak separation using the Gaussian function.

### 3.4.2 Difference in clustering evolution between NA and PA

We analyzed the number density, size and Mg/(Mg+Si) of Cluster (1) after natural aging using APT by several authors for the Al-Mg-Si alloy, and their results are displayed in Table 3.4. Among them, a summary of the results with NA time and alloy composition are as follows. Rometsch et al. [17] analyzed the clustering behavior with the different NA times in the Al-Mg-Si-Cu alloy with Mg/(Mg+Si) = 0.31. Their results confirmed that as the NA time increased, the number density of Cluster (1) increased and the size was similar [17]. Moreover, Mg/(Mg+Si) was highest at the early stage of two-step aging [17]. Zandbergen et al. [11] analyzed the formation of Cluster (1) formed during different NA times in the Al-Mg-Si alloy with Mg/(Mg+Si) = 0.49. They found that as the NA time increased, the number density of Cluster (1) increased and the size was similar [11]. Mg/(Mg+Si) did not significantly differ from the NA time [11]. Aruga et al. [22] analyzed the clustering behavior with different NA times in the Al-Mg-Si alloy with Mg/(Mg+Si) = 0.40 and 0.53 [22]. They confirmed that as the NA time increased, the number density of Cluster (1) increased and the size was similar [22].

It can be seen that Mg/(Mg+Si) was affected by the alloy composition in a short NA time and close to Mg:Si = 1:1 in a long NA time [22]. Generally, the literature confirms that the number density of Cluster (1) increased as the NA time increased, whereas the size was similar regardless of the NA time. Meanwhile, the number density of $Cluster_{604.8}^{50}$ was two times higher than that of $Cluster_{604.8}^{25}$ and the size was similar (see Fig. 3.9 and Table 3.3). There is further discussion about the difference of clustering behavior during NA and PA at 50 ℃.

As shown in Fig. 3.5, hardness quickly increased during PA at 50 ℃ over that of NA. It seems that Cluster (1) formation was accelerated during PA at 50 ℃ compared to NA. Referring to several studies reported so far, Mg/(Mg+Si) of Cluster (1) with the NA time seemed to be different depending on the process (see Table 3.4). Chen et al. [66] insisted that the Si column, which provides the skeleton for the nanoparticles to evolve, is first formed, and then they grow by replacing Al as Mg and Si atoms. Gupta et al. [30] explained that the Si-rich cluster is formed at the early stage of NA, and as the NA time increases, Mg is incorporated. Fallah et al. [12] investigated the cluster evolution mechanism at room temperature and 170 ℃ using modeling and APT in Al-0.71% Mg-0.83% Si and Al-0.84% Mg-0.49% Si (mass%) alloys. They reported that Si-rich clusters are formed at the initial stage of aging, and then Mg-enrichment is essential for cluster evolution. Their results show that the Mg-enrichment for cluster evolution depends on aging temperature. In our APT results, Mg-enrichment is confirmed during PA at 50 ℃ for 604.8 ks versus NA for 604.8 ks (see Table 3.3). Such a distinction between variation in cluster composition during NA and PA at 50 ℃ is compared by normalization of aging time. Applying the normalized aging time for the different aging temperatures is useful to understanding the clustering behavior based on diffusivity of atoms. In order to normalize the aging time at 50 ℃ into the aging time at room temperature (about 25 ℃), Eq. (3.1) was used. Based on this equation, 604.8 ks at 50 ℃ was calculated as 35,105

ks (about 14 months) at room temperature. It is reasonable that the acceleration of diffusion due to the increase in temperature accelerated the Mg-enrichment of the clusters. Thus, we determined that formation of Mg-enriched Cluster (1) is accelerated more during PA at 50 ℃ than during NA. Meanwhile, normalization of aging time at 100 ℃ into the aging time at 50 ℃ for 604.8 ks is calculated as 0.9 ks using Eq. (3.1). Cluster (2) seems to be formed at 100 ℃ within 0.3 ks [37]. However, based on the experimentally obtained results in this study, there was no Cluster (2) found during PA at 50 ℃. It is noted that Cluster (1) does not evolve into Cluster (2) during aging below 50 ℃.

The time-temperature transformation (TTT) curve is obtained by calculating the fraction transformed with time at a given temperature. The fraction transformed at a given time and temperature can be obtained by various methods such as modeling, hardness, electrical conductivity and DSC [67–69]. The TTT curve is arbitrarily described in Fig. 3.10 by focusing only on the transition of the cluster discussed above. The red line represents the solvus temperature of each phase. The blue line represents the heat treatment history of NA and PA at 50 ℃. Figure 3.10 is oversimplified, but it is note that the TTT curve is drawn with a solid line for convenience. Those TTT curves show that the phase transition from Cluster (1) to Cluster (2) does not occur after PA at 50 ℃ for 604.8 ks, and PA at 50 ℃ is closer to the nose of the Cluster (1) curve than NA.

### 3.5 Conclusions

We investigated the clustering evolution of the nanoclusters at the initial stage of two-step aging in the Al-0.6% Mg-0.6% Si (mass%) alloy by hardness, electrical resistivity and DSC measurements and APT analyses. The summary of the main findings is as follows.

- The peak area of nanocluster dissolution generated during DSC increased as the PA time increased. A dramatic decrease in hardness and electrical resistivity at the early stage of two-step aging at 170 °C was identified in PA for 604.8 ks, which was due to the dissolution of clusters. Those experimental results show that there is a limitation to predicting the temperature ranges of cluster formation based on the peak separation using the Gaussian function.
- The average size of clusters for NA and PA was 0.63 and 0.68 nm, respectively. The highest proportion of Balanced clusters ($0.4 \leq Mg/(Mg+Si) \leq 0.6$) was confirmed in both the NA and PA specimens. Meanwhile, the Mg-enriched clusters ($Mg/(Mg+Si) \geq 0.7$) were analyzed only in PA when the size of clusters was over the average size of 0.6 nm. It was determined that the increase in aging temperature accelerated the Mg-enrichment of a cluster but did not contribute to the transition from Cluster (1) to Cluster (2).

**References**

[1] M. Murayama, K. Hono, Pre-precipitate clusters and precipitation processes in Al–Mg–Si alloys, Acta Mater. 47 (1999) 1537–1548. https://doi.org/10.1016/S1359-6454(99)00033-6.

[2] Q. Xiao, H. Liu, D. Yi, D. Yin, Y. Chen, Y. Zhang, B. Wang, Effect of Cu content on precipitation and age-hardening behavior in Al-Mg-Si-xCu alloys, J. Alloys Compd. 695 (2017) 1005–1013. https://doi.org/10.1016/j.jallcom.2016.10.221.

[3] Y. Chen, Q. Hu, S. Pan, H. Zhang, H. Liu, B. Zhu, X. Liu, W. Liu, Influences of Cu Content on the Microstructure and Strengthening Mechanisms of Al-Mg-Si-xCu Alloys, Metals (Basel). 9 (2019) 524. https://doi.org/10.3390/met9050524.

[4] H. Chen, J. Lu, Y. Kong, K. Li, T. Yang, A. Meingast, M. Yang, Q. Lu, Y. Du, Atomic scale investigation of the crystal structure and interfaces of the B′ precipitate in Al-Mg-Si alloys, Acta Mater. 185 (2020) 193–203. https://doi.org/10.1016/j.actamat.2019.11.059.

[5] J.K. Sunde, C.D. Marioara, R. Holmestad, The effect of low Cu additions on precipitate crystal structures in overaged Al-Mg-Si(-Cu) alloys, Mater. Charact. 160 (2020) 110087. https://doi.org/10.1016/j.matchar.2019.110087.

[6] Y.X. Lai, W. Fan, M.J. Yin, C.L. Wu, J.H. Chen, Structures and formation mechanisms of dislocation-induced precipitates in relation to the age-hardening responses of Al-Mg-Si alloys, J. Mater. Sci. Technol. 41 (2020) 127–138. https://doi.org/10.1016/j.jmst.2019.11.001.

[7] S. Jiang, R. Wang, Grain size-dependent Mg/Si ratio effect on the microstructure and mechanical/electrical properties of Al-Mg-Si-Sc alloys, J. Mater. Sci. Technol. 35 (2019) 1354–1363. https://doi.org/10.1016/j.jmst.2019.03.011.

[8] M. Liu, Q. Guo, X. Zhang, M. Wüstenhagen, J. Čížek, J. Banhart, Scripta Materialia Clustering phenomena in quenched Al, Al–Mg, Al–Si and Al–Mg–Si alloys, 177 (2020) 203–207. https://doi.org/10.1016/j.scriptamat.2019.10.034.

[9] N.N. Jiao, Y.X. Lai, S.L. Chen, P. Gao, J.H. Chen, Atomic-scale roles of Zn element in age-hardened AlMgSiZn alloys, J. Mater. Sci. Technol. 70 (2021) 105–112. https://doi.org/10.1016/j.jmst.2020.09.009.

[10] H. Jin, R. Guan, X. Huang, Y. Fu, J. Zhang, X. Chen, Y. Wang, F. Gao, D. Tie, Understanding the precipitation mechanism of copper-bearing phases in Al-Mg-Si system during thermo-mechanical treatment, J. Mater. Sci. Technol. 96 (2022) 226–232. https://doi.org/10.1016/j.jmst.2021.04.026.

[11] M.W. Zandbergen, Q. Xu, A. Cerezo, G.D.W. Smith, Study of precipitation in Al–Mg–Si alloys by Atom Probe Tomography I. Microstructural changes as a function of ageing temperature, Acta Mater. 101 (2015) 136–148. https://doi.org/10.1016/j.actamat.2015.08.017.

[12] V. Fallah, B. Langelier, N. Ofori-Opoku, B. Raeisinia, N. Provatas, S. Esmaeili, Cluster evolution mechanisms during aging in Al-Mg-Si alloys, Acta Mater. 103 (2016) 290–300. https://doi.org/10.1016/j.actamat.2015.09.027.

[13] M.Y. Song, J.H. Kim, Microstructural evolution at the initial stage of two-step aging in an Al-Mg-Si alloy characterized by a three dimensional atom probe, Mater. Sci. Eng. A. 815 (2021) 141301. https://doi.org/10.1016/j.msea.2021.141301.

[14] C.S.T. Chang, I. Wieler, N. Wanderka, J. Banhart, Positive effect of natural pre-ageing on precipitation hardening in Al–0.44 at% Mg–0.38 at% Si alloy, Ultramicroscopy. 109 (2009) 585–592. https://doi.org/10.1016/j.ultramic.2008.12.002.

[15] A. Serizawa, T. Sato, W.J. Poole, The characterization of dislocation-nanocluster interactions in Al-Mg-Si(-Cu/Ag) alloys, Philos. Mag. Lett. 90 (2010) 279–287. https://doi.org/10.1080/09500831003633231.

[16] M. Torster, H.S. Hasting, W. Lefebvre, C.D. Marioara, J.C. Walmsley, S.J. Andersen, R. Holmestad, The influence of composition and natural aging on clustering during preaging in Al-Mg-Si alloys, J. Appl. Phys. 108 (2010) 1–9. https://doi.org/10.1063/1.3481090.

[17] P.A. Rometsch, L.F. Cao, X.Y. Xiong, B.C. Muddle, Atom probe analysis of early-stage strengthening behaviour in an Al-Mg-Si-Cu alloy, Ultramicroscopy. 111 (2011) 690–694. https://doi.org/10.1016/j.ultramic.2010.11.009.

[18] N. Wanderka, N. Lazarev, C.S.T. Chang, J. Banhart, Analysis of clustering in Al–Mg–Si alloy by density spectrum analysis of atom probe data, Ultramicroscopy. 111 (2011) 701–705. https://doi.org/10.1016/j.ultramic.2010.11.022.

[19] Y. Aruga, M. Kozuka, Y. Takaki, T. Sato, Evaluation of Solute Clusters Associated with Bake-Hardening Response in Isothermal Aged Al-Mg-Si Alloys Using a Three-Dimensional Atom Probe, Metall. Mater. Trans. A. 45 (2014) 5906–5913. https://doi.org/10.1007/s11661-014-2548-y.

[20] Z. Jia, L. Ding, L. Cao, R. Sanders, S. Li, Q. Liu, The Influence of Composition on the Clustering and Precipitation Behavior of Al-Mg-Si-Cu Alloys, Metall. Mater. Trans. A. 48 (2017) 459–473. https://doi.org/10.1007/s11661-016-3850-7.

[21] H. Zhong, P.A. Rometsch, X. Wu, L. Cao, Y. Estrin, Influence of pre-ageing on the stretch formability of Al-Mg-Si automotive sheet alloys, Mater. Sci. Eng. A. 697 (2017) 79–85. https://doi.org/10.1016/j.msea.2017.05.009.

[22] Y. Aruga, S.N. Kim, M. Kozuka, E. Kobayashi, T. Sato, Effects of cluster characteristics on two-step aging behavior in Al-Mg-Si alloys with different Mg/Si ratios and natural aging periods, Mater. Sci. Eng. A. 718 (2018) 371–376. https://doi.org/10.1016/j.msea.2018.01.086.

[23] Y. Aruga, M. Kozuka, T. Sato, Formulation of initial artificial age-hardening response in an Al-Mg-Si alloy based on the cluster classification using a high-detection-efficiency atom probe, J. Alloys Compd. 739 (2018) 1115–1123. https://doi.org/10.1016/j.jallcom.2017.10.220.

[24] A. Poznak, R.K.W. Marceau, P.G. Sanders, Composition dependent thermal stability and evolution of solute clusters in Al-Mg-Si analyzed using atom probe tomography, Mater. Sci. Eng. A. 721 (2018) 47–60. https://doi.org/10.1016/j.msea.2018.02.074.

[25] O. Engler, C.D. Marioara, Y. Aruga, M. Kozuka, O.R. Myhr, Effect of natural ageing or pre-ageing on the evolution of precipitate structure and strength during age hardening of Al–Mg–Si alloy AA 6016, Mater. Sci. Eng. A. 759 (2019) 520–529. https://doi.org/10.1016/j.msea.2019.05.073.

[26] W. Yu, H. He, W. Zhang, L. Li, C. Sun, Modulation of the natural aging effect on subsequent artificial aging in Al–Mg–Si aluminum alloys with alloying content～1wt% through temperature tuning, J. Alloys Compd. 814 (2020) 152277. https://doi.org/10.1016/j.jallcom.2019.152277.

[27] W. Tu, J. Tang, L. Ye, L. Cao, Y. Zeng, Q. Zhu, Y. Zhang, S. Liu, L. Ma, J. Lu, B. Yang, Effect of the natural aging time on the age-hardening response and precipitation behavior of the Al-0.4Mg-1.0Si-(Sn) alloy, Mater. Des. 198 (2021) 109307. https://doi.org/10.1016/j.matdes.2020.109307.

[28] T. Sato, High strength and high ductility aluminum alloys with controlled nano-clusters, J. Japan Inst. Light Met. 56 (2006) 592–601. https://doi.org/10.2464/jilm.56.592.

[29] A. Serizawa, S. Hirosawa, T. Sato, Three-Dimensional Atom Probe Characterization of Nanoclusters Responsible for Multistep Aging Behavior of an Al-Mg-Si Alloy, Metall. Mater. Trans. A. 39 (2008) 243–251. https://doi.org/10.1007/s11661-007-9438-5.

[30] A.K. Gupta, D.J. Lloyd, Study of precipitation kinetics in a super purity Al-0.8 pct Mg-0.9 pct Si alloy using differential scanning calorimetry, Metall. Mater. Trans. A. 30 (1999) 879–884. https://doi.org/10.1007/s11661-999-0081-1.

[31] J. Banhart, C.S.T. Chang, Z. Liang, N. Wanderka, M.D.H. Lay, A.J. Hill, Natural Aging in Al-Mg-Si Alloys - A Process of Unexpected Complexity, Adv. Eng. Mater. 12 (2010) 559–571. https://doi.org/10.1002/adem.201000041.

[32] C.S.T. Chang, J. Banhart, Low-Temperature Differential Scanning Calorimetry of an Al-Mg-Si Alloy, Metall. Mater. Trans. A. 42 (2011) 1960–1964. https://doi.org/10.1007/s11661-010-0596-5.

[33] J. Kim, J. Im, M. Song, I. Kim, Effects of Mg Addition and Pre-Aging on the Age-Hardening Behavior in Al-Mg-Si, Metals (Basel). 8 (2018) 1046.

https://doi.org/10.3390/met8121046.

[34] S. Kim, J. Kim, H. Tezuka, E. Kobayashi, T. Sato, Formation Behavior of Nanoclusters in Al-Mg-Si Alloys with Different Mg and Si Concentration, Mater. Trans. 54 (2013) 297–303. https://doi.org/10.2320/matertrans.MBW201208.

[35] G. Moreau, J.A. Cornet, D. Calais, Acceleration de la diffusion chimique sous irradiation dans le systeme aluminium-magnesium, J. Nucl. Mater. 38 (1971) 197–202. https://doi.org/10.1016/0022-3115(71)90043-2.

[36] K. HIRANO, Diffusion in aluminum, J. Japan Inst. Light Met. 29 (1979) 249–262. https://doi.org/10.2464/jilm.29.249.

[37] H. Hatta, S. Matsuda, H. Tanaka, H. Yoshida, Effects of pre-aging at elevated temperature and natural aging on the bake hardenability of Al–Mg–Si alloy, J. Japan Inst. Light Met. 59 (2009) 248–253. https://doi.org/10.2464/jilm.59.248.

[38] S. Wenner, K. Nishimura, K. Matsuda, C.D. Marioara, R. Holmestad, Clustering and Vacancy Behavior in High- and Low-Solute Al-Mg-Si Alloys, 45 (2014) 5777–5781. https://doi.org/10.1007/s11661-014-2527-3.

[39] Z. Yang, J. Banhart, Acta Materialia Natural and artificial ageing in aluminium alloys – the role of excess vacancies, Acta Mater. 215 (2021) 117014. https://doi.org/10.1016/j.actamat.2021.117014.

[40] Y. Weng, Z. Jia, L. Ding, S. Muraishi, Q. Liu, Clustering behavior during natural aging and artificial aging in Al-Mg-Si alloys with different Ag and Cu addition, Mater. Sci. Eng. A. 732 (2018) 273–283. https://doi.org/10.1016/j.msea.2018.07.018.

[41] D.J. Larson, D.T. Foord, A.K. Petford-Long, T.C. Anthony, I.M. Rozdilsky, A. Cerezo, G.W.D. Smith, Focused ion-beam milling for field-ion specimen preparation: preliminary investigations, Ultramicroscopy. 75 (1998) 147–159.

https://doi.org/10.1016/S0304-3991(98)00058-8.

[42] D.J. Larson, D.T. Foord, A.K. Petford-Long, A. Cerezo, G.D.W. Smith, Focused ion-beam specimen preparation for atom probe field-ion microscopy characterization of multilayer film structures, Nanotechnology. 10 (1999) 45–50. https://doi.org/10.1088/0957-4484/10/1/010.

[43] B. Gault, M.P. Moody, J.M. Cairney, S.P. Ringer, Atom Probe Microscopy, 1st ed., Springer US, 2012.

[44] L.T. Stephenson, M.P. Moody, P. V. Liddicoat, S.P. Ringer, New Techniques for the Analysis of Fine-Scaled Clustering Phenomena within Atom Probe Tomography (APT) Data, Microsc. Microanal. 13 (2007) 448–463. https://doi.org/10.1017/S1431927607070900.

[45] D. Vaumousse, A. Cerezo, P.J. Warren, A procedure for quantification of precipitate microstructures from three-dimensional atom probe data, Ultramicroscopy. 95 (2003) 215–221. https://doi.org/10.1016/S0304-3991(02)00319-4.

[46] J.M. Hyde, E.A. Marquis, K.B. Wilford, T.J. Williams, A sensitivity analysis of the maximum separation method for the characterisation of solute clusters, Ultramicroscopy. 111 (2011) 440–447. https://doi.org/10.1016/j.ultramic.2010.12.015.

[47] G.A. Edwards, K. Stiller, G.L. Dunlop, M.J. Couper, The precipitation sequence in Al–Mg–Si alloys, Acta Mater. 46 (1998) 3893–3904. https://doi.org/10.1016/S1359-6454(98)00059-7.

[48] N. Maruyama, R. Uemori, N. Hashimoto, M. Saga, M. Kikuchi, Effect of silicon addition on the composition and structure of fine-scale precipitates in Al-Mg-Si alloys, Scr. Mater. 36 (1997) 89–93. https://doi.org/10.1016/S1359-6462(96)00358-2.

[49] W.F. Miao, D.E. Laughlin, Precipitation hardening in aluminum alloy 6022, Scr. Mater. 40 (1999) 873–878. https://doi.org/10.1016/S1359-6462(99)00046-9.

[50] M.K. Miller, R.G. Forbes, Atom-Probe Tomography, 1st ed., Springer US, Boston, MA, 2014. https://doi.org/10.1007/978-1-4899-7430-3.

[51] A. Serizawa, S. Hirosawa, T. Sato, 3DAP Characterization and Thermal Stability of Nano-Scale Clusters in Al-Mg-Si Alloys, Mater. Sci. Forum. 519–521 (2006) 245–250. https://doi.org/10.4028/www.scientific.net/MSF.519-521.245.

[52] K. Yamada, T. Sato, A. Kamio, Effects of Quenching Conditions on Two-Step Aging Behavior of Al-Mg-Si Alloys, Mater. Sci. Forum. 331–337 (2000) 669–674. https://doi.org/10.4028/www.scientific.net/MSF.331-337.669.

[53] D.W. Pashley, M.H. Jacobs, J.T. Vietz, The basic processes affecting two-step ageing in an Al-Mg-Si alloy, Philos. Mag. 16 (1967) 51–76. https://doi.org/10.1080/14786436708229257.

[54] D.W. Pashley, J.W. Rohdes, A. Sendorek, Delayed Ageing in Aluminium-Magnesium-Silicon Alloys: Effect on Structure and Mechanical Properties, J. Institue Met. 94 (1966) 41–49.

[55] J. Im, J. Jeon, M. Song, S. Hong, J. Kim, Influence of Natural Aging Time and Mg/Si Ratio (Mg + Si = 1.3 mass%) on the Two-Step Aging Behavior in Al–Mg–Si Alloys, Met. Mater. Int. 25 (2019) 860–868. https://doi.org/10.1007/s12540-019-00257-8.

[56] L. Zhen, S.B. Kang, DSC analyses of the precipitation behavior of two Al-Mg-Si alloys naturally aged for different times, Mater. Lett. 37 (1998) 349–353. https://doi.org/10.1016/S0167-577X(98)00118-9.

[57] K. Osamura, Y. Hiraoka, Y. Murakami, The resistivity maximum during Guinier-Preston zone formation in Al-Zn alloys, Philos. Mag. 28 (1973) 809–825. https://doi.org/10.1080/14786437308220985.

[58] Y. Takaki, T. Masuda, E. Kobayashi, T. Sato, Effects of Natural Aging on Bake Hardening Behavior of Al-Mg-Si Alloys with Multi-Step Aging Process, Mater. Trans. 55 (2014) 1257–1265. https://doi.org/10.2320/matertrans.L-M2014827.

[59] M. Liu, Z. Wu, R. Yang, J. Wei, Y. Yu, P.C. Skaret, H.J. Roven, DSC analyses of static and dynamic precipitation of an Al–Mg–Si–Cu aluminum alloy, Prog. Nat. Sci. Mater. Int. 25 (2015) 153–158. https://doi.org/10.1016/j.pnsc.2015.02.004.

[60] G.H. Tao, C.H. Liu, J.H. Chen, Y.X. Lai, P.P. Ma, L.M. Liu, The influence of Mg/Si ratio on the negative natural aging effect in Al-Mg-Si-Cu alloys, Mater. Sci. Eng. A. 642 (2015) 241–248. https://doi.org/10.1016/j.msea.2015.06.090.

[61] M. Madanat, M. Liu, J. Banhart, Reversion of natural ageing in Al-Mg-Si alloys, Acta Mater. 159 (2018) 163–172. https://doi.org/10.1016/j.actamat.2018.07.066.

[62] L. He, H. Zhang, J. Cui, Effects of Pre-Ageing Treatment on Subsequent Artificial Ageing Characteristics of an Al-1.01Mg-0.68Si-1.78Cu Alloy, J. Mater. Sci. Technol. 26 (2010) 141–145. https://doi.org/10.1016/S1005-0302(10)60023-0.

[63] C.-H. Shen, Pre-treatment to Improve the Bake-hardening Response in the Naturally Aged Al-Mg-Si Alloy, J. Mater. Sci. Technol. 27 (2011) 205–212. https://doi.org/10.1016/S1005-0302(11)60050-9.

[64] G.W.H. Höhne, W.F. Hemminger, H.-J. Flammersheim, Differential Scanning Calorimetry, Springer Berlin Heidelberg, Berlin, Heidelberg, 2003. https://doi.org/10.1007/978-3-662-06710-9.

[65] W.H. Press, S.A. Teukolsky, W.T. Vetterling, B.P. Flannery, Numerical recipes: The art of scientific computing, 3rd ed., Cambridge University Press, New York, NY, 2007.

[66] J.H. Chen, E. Costan, M.A. van Huis, Q. Xu, H.W. Zandbergen, Atomic Pillar-Based Nanoprecipitates Strengthen AlMgSi Alloys, Science (80-. ). 312 (2006) 416–419. https://doi.org/10.1126/science.1124199.

[67] B. Milkereit, L. Giersberg, O. Kessler, C. Schick, Isothermal Time-Temperature-Precipitation Diagram for an Aluminum Alloy 6005A by In Situ DSC Experiments, Materials (Basel). 7 (2014) 2631–2649. https://doi.org/10.3390/ma7042631.

[68] D. Lu, H. Ning, Y. Du, J. Li, D. Liu, Y. Guo, Y. Chen, X. Zhang, W. You, K. Zhang, R. Zhang, Detailed investigation of quench sensitivity of 2050 Al-Cu-Li alloy by interrupted quenching method and novel end quenching method, J. Alloys Compd. 888 (2021) 161450. https://doi.org/10.1016/j.jallcom.2021.161450.

[69] D. Liu, Y. Ma, J. Li, C. Liu, Y. Du, Y. Chen, X. Zhang, W. You, R. Zhang, Materials Characterization Quench sensitivity and microstructure evolution of the 2060 Al-Cu-Li alloy with a low Mg content, Mater. Charact. 177 (2021) 111156. https://doi.org/10.1016/j.matchar.2021.111156.

**Tables**

Table 3.1 The definition of the symbols used throughout this study.

| Symbol | Meaning |
|---|---|
| ST | Solution treatment |
| AQ | As-quenched |
| NA | Natural aging |
| PA | Pre-aging |
| AA | Artificial aging |
| SA | Single aging |
| SA(Temp.) | Single aging during a specific temperature |
| TSA(Temp.) | Two-step aging during a specific temperature |
| TSA (Temp., time (ks)) | Two-step aging during a specific time and temperature |
| DSC | Differential scanning calorimetry |
| FIB | Focused ion beam |
| APT | Atom probe tomography |
| $Cluster^{Temp.}$ | Clusters formed at a specific temperature |
| $Cluster^{Temp.}_{time\ (ks)}$ | Clusters formed at a specific time and temperature |
| $l_g$ | Gyration radius |
| $r_G$ | Guinier radius |

Table 3.2 Summary of the heat-treatment process. ST, NA, PA, AA and TSA are the solution treatment, natural aging, pre-aging, artificial aging and two-step aging, respectively.

| Type | Process | Mark |
|---|---|---|
| SA | NA | |
| | PA at 50 ℃ | |
| | ST-AA (170 ℃) | SA (170) |
| TSA | ST-NA(604.8 ks)-AA (170 ℃) | TSA (NA) |
| | ST-PA(50 ℃, 0.06 ks)-AA (170 ℃) | TSA (0.06) |
| | ST-PA(50 ℃, 3.6 ks)-AA (170 ℃) | TSA (3.6) |
| | ST-PA(50 ℃, 604.8 ks)-AA (170 ℃) | TSA (604.8) |

Table 3.3 Statistical data of clusters formed after natural aging and pre-aging at 50 °C for 604.8 ks analyzed by a $N_{min}$ of 10 atoms and $D_{max}$ 0.75 nm of atom probe measurements.

| | $Cluster_{604.8}^{25}$ | $Cluster_{604.8}^{50}$ |
|---|---|---|
| Avg. Guinier radius (nm) | 0.63 | 0.68 |
| Number density ($10^{23}$ $m^{-3}$) | 18.9 | 38.6 |
| Avg. atomic density ($nm^{-3}$) | 26.5 | 21.1 |
| Avg. Mg/(Mg+Si) | 0.54 | 0.58 |

Table 3.4 Summary of the number density, size and Mg/(Mg+Si) of $Cluster^{25}$ with the natural aging time and alloy composition, investigated by several authors.

| Equipment | Chemical composition of alloys (mass%) | | | Natural aging time (ks) | Characteristics of clusters | | | | Reference |
|---|---|---|---|---|---|---|---|---|---|
| | Mg | Si | Mg/(Mg+Si) | | Mg/(Mg+Si) (mass%) | Guinier radius (nm) | Number of solute atoms | Number density ($10^{23}$ $m^{-3}$) | |
| ECAP[a] | 0.58 | 0.73 | 0.44 | 6048 | 0.5 | - | - | - | [8] |
| ECAP[a] | 0.93 | 0.81 | 0.54 | ~ 605 | - | - | - | - | [10] |
| DLD[a] | 0.95 | 0.81 | 0.54 | 605 | - | - | - | 16.0 | [5] |
| Unknown | 0.44 | 0.38 | 0.54 | 605 | - | - | - | - | [24] |
| DLD[a] | 0.91 | 0.80 | 0.53 | ~ 7258 | - | - | - | - | [25] |
| ECAP[a] | 0.48 | 1.07 | 0.31 | 13 | 0.50 | - | 31 | 2.0 | [27] |
| | | | | 605 | 0.41 | - | 25 | 25.0 | |
| | | | | 2592 | 0.41 | - | 35 | 44.0 | |
| Unknown | 0.59 | 0.82 | 0.42 | 605 | - | - | - | - | [28] |
| LEAP[c] 3000 | 0.62 | 0.93 | 0.40 | 108 | - | 1.20 | - | 15.0 | [29] |
| | | | | 28000 | - | 1.20 | - | 19.0 | |
| LEAP[c] 3000 | 0.62 | 0.93 | 0.40 | 11 | 0.55 | 1.30 | - | 11.0 | [6] |
| | | | | 108 | 0.50 | 1.20 | - | 15.0 | |
| | | | | 360 | 0.50 | 1.30 | - | 17.0 | |
| | | | | 1080 | 0.52 | 1.20 | - | 14.0 | |
| | | | | 7200 | 0.50 | 1.40 | - | 21.0 | |
| | | | | 28000 | 0.55 | 1.30 | - | 19.0 | |
| LEAP[c] | 0.46 | 0.98 | 0.49 | 6 | 0.42 | - | 12 | 2.4 | [21] |
| | | | | 60 | 0.39 | - | 13 | 6.7 | |
| | | | | 605 | 0.40 | - | 14 | 11.6 | |
| | 0.71 | 0.83 | 0.46 | 173 | - | - | - | 9.3 | [22] |

| | | | | | | | | | |
|---|---|---|---|---|---|---|---|---|---|
| LEAP[c] 4000 | 0.84 | 0.49 | 0.63 | | - | - | - | 3.7 | |
| LEAP[c] 4000 | 0.62 | 1.11 | 0.36 | 1210 | 0.53 | - | 63 | 0.024 | [30] |
| | 1.17 | 0.59 | 0.66 | | 0.73 | - | 47 | 0.005 | |
| LEAP[c] 4000 | 1.06 | 0.50 | 0.68 | 605 | - | - | - | - | [31] |
| | 0.70 | 0.80 | 0.47 | | - | - | - | - | |
| | 0.41 | 1.26 | 0.25 | | - | - | - | - | |
| LEAP[c] 3000 | 0.62 | 0.93 | 0.40 | 360 | 0.45 | 1.26 | - | 16.8 | [33] |
| | | | | 28000 | 0.49 | 1.25 | - | 19.3 | |
| LEAP[c] 5000 | 0.62 | 0.93 | 0.40 | 360 | 0.50 | 1.44 | - | 21.4 | |
| | | | | 100000 | 0.50 | 1.44 | - | 36.6 | |
| LEAP[c] 3000 | 0.62 | 0.93 | 0.40 | 108 | 0.46 | 1.24 | - | 15.1 | [32] |
| | 0.78 | 0.70 | 0.53 | | 0.60 | 1.26 | - | 15.0 | |
| | 0.62 | 0.93 | 0.40 | 7200 | 0.52 | 1.21 | - | 17.2 | |
| | 0.78 | 0.70 | 0.53 | | 0.54 | 1.22 | - | 17.2 | |
| LEAP[c] 4000 | 0.99 | 0.42 | 0.70 | 2419 | 0.64 | - | 8 | 18.1 | [34] |
| | 0.28 | 1.13 | 0.20 | 2419 | 0.35 | - | 9 | 21.3 | |
| LEAP[c] 3000 | 0.30 | 1.23 | 0.20 | 2419 | 0.44 | 1.21 | - | 7.4 | [35] |
| LEAP[c] 5000 | 0.55 | 0.43 | 0.56 | 1555 | 0.35 | 1.35 | - | 6.6 | [36] |
| LEAP[c] 4000 | 0.41 | 1.06 | 0.28 | 87 | 0.52 | 0.54[d] | - | 5.5 | [37] |
| LEAP[c] 4000 | 0.90 | 1.00 | 0.47 | 2419 | 0.46 | 0.91 | - | 235.0 | [23] |

[a] Energy compensated atom probe (ECAP)

[b] Imago Scientific Instruments (Madison, WI) 3DAP with a delay-line detector (DLD)

[c] Local electrode atom probe (LEAP)

[d] Calculated by an unspecified method other than Guinier radius

**Figures**

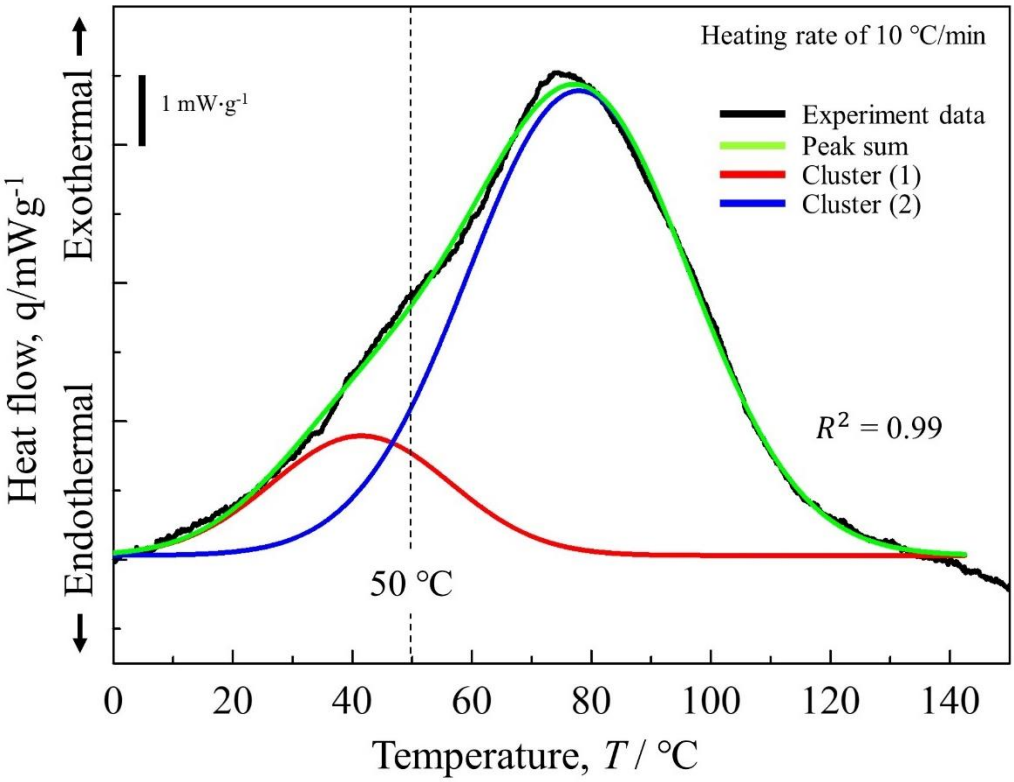


Figure 3.1 Peak separation of DSC corresponding to Cluster (1) and Cluster (2) using Gaussian function. Red, blue and green line are the peak of Cluster (1), Cluster (2) and sum, respectively. Black solid line represents the experiment data. Black dotted line indicates 50 °C at which pre-aging was performed in this study.

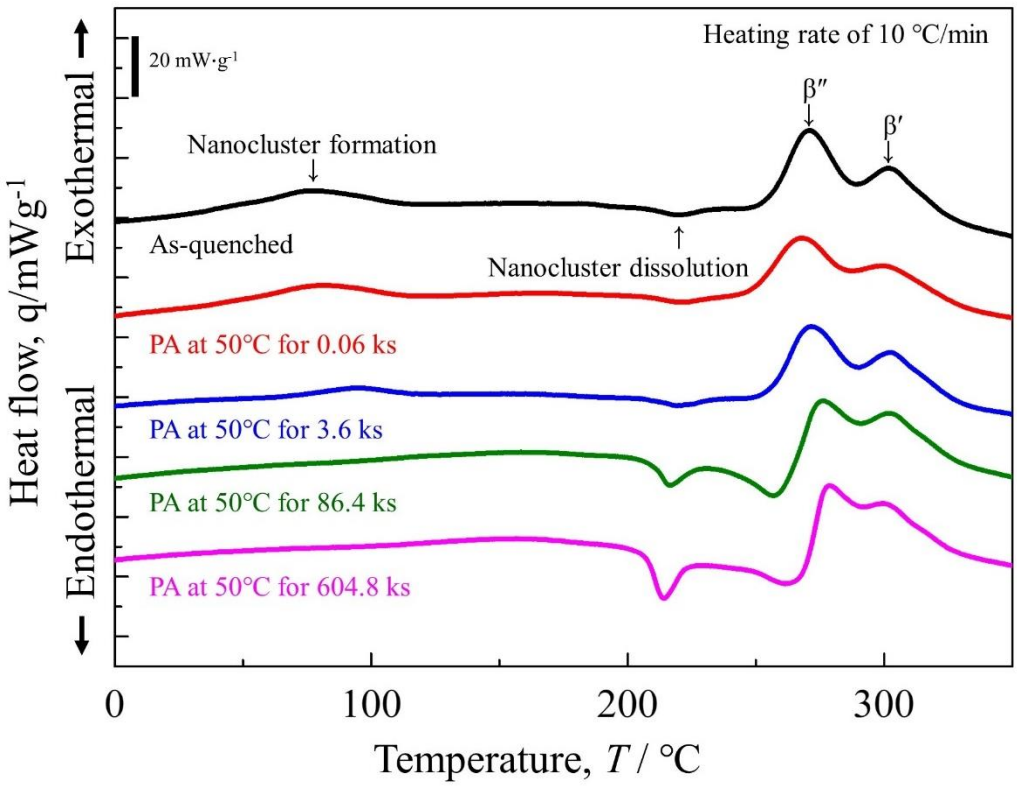


Figure 3.2 The DSC thermograms for the samples aged with the different pre-aging time at 50 °C. From low temperature, it represents nanocluster formation, nanocluster dissolution, β″ and β′.

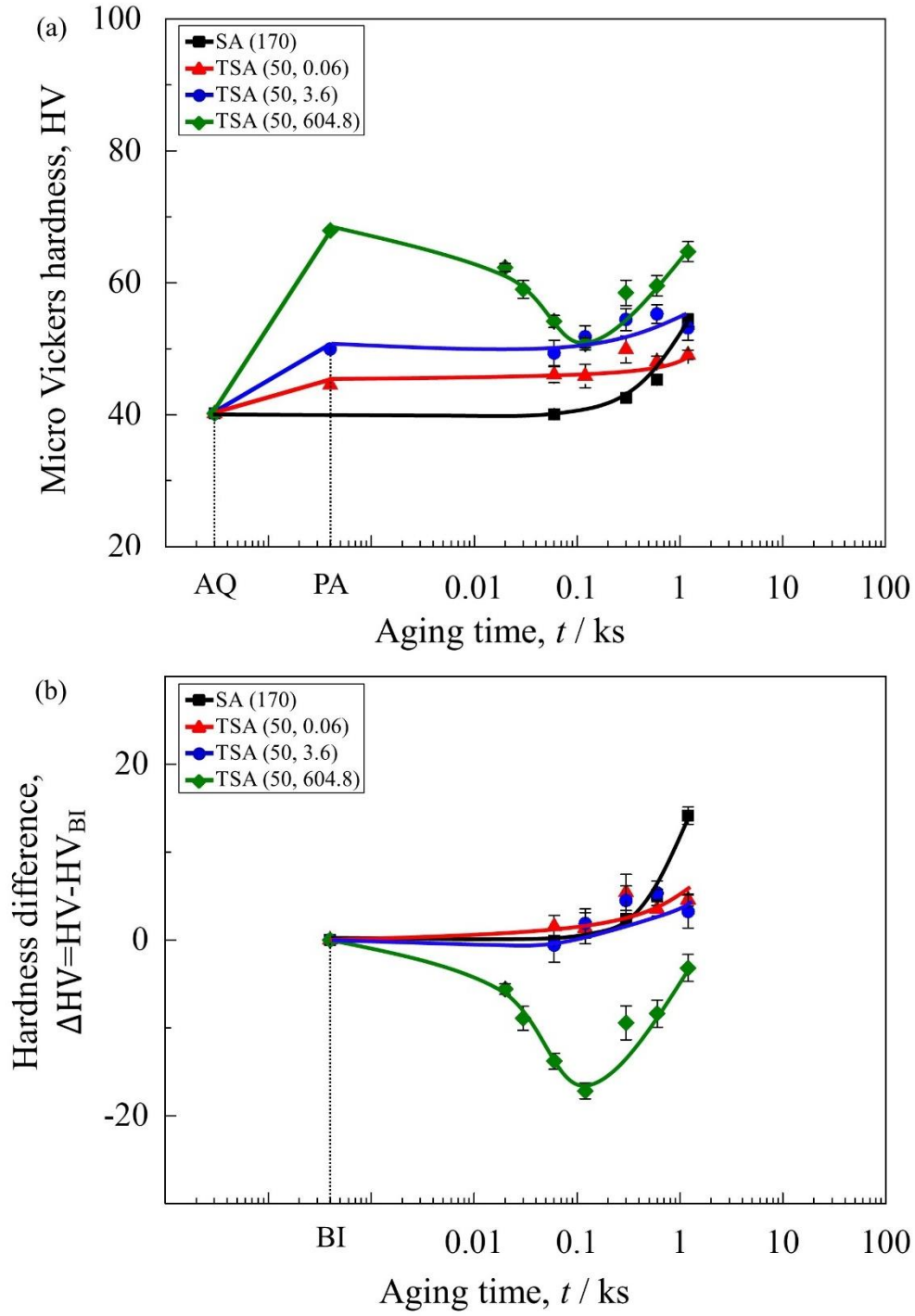


Figure 3.3 (a) The hardness changes and (b) hardness difference (ΔHV) during the early stage of two-step aging at 170 ℃ with the different heat treatments. ΔHV is obtained as the difference value of the obtained hardness during the two-step aging from before isothermal aging at 170 ℃.

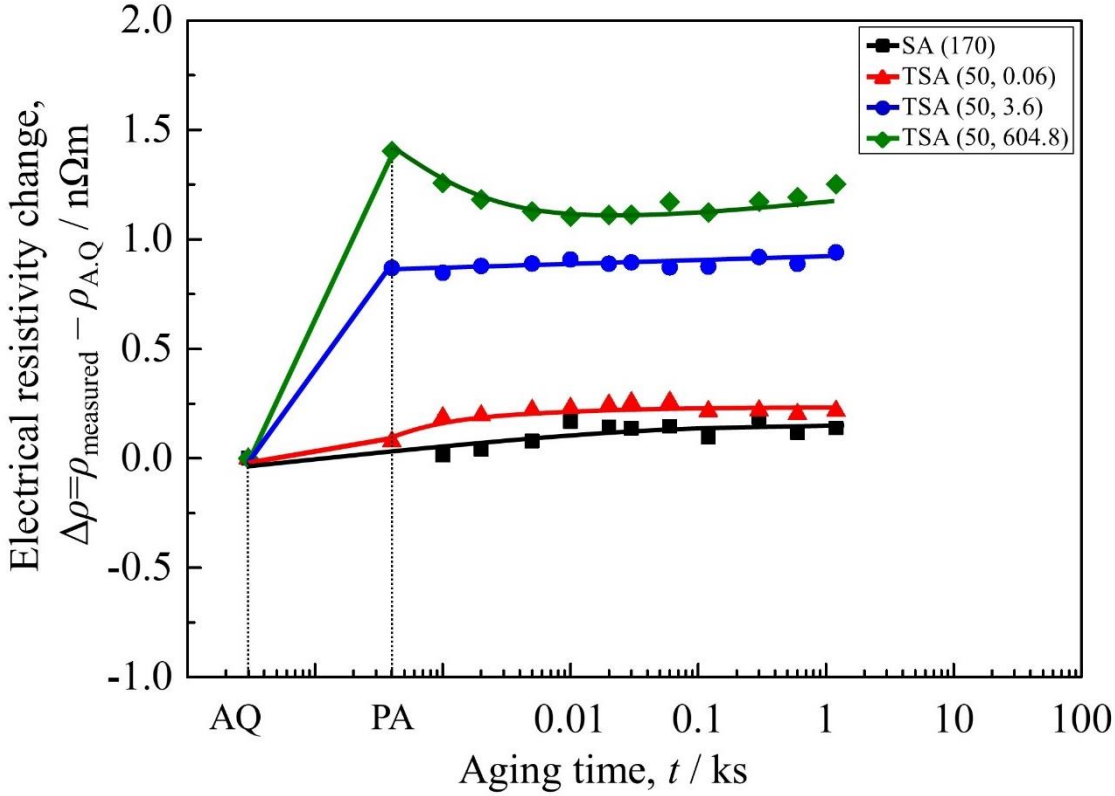


Figure 3.4 Changes of electrical resistivity from as-quenched (AQ) state during isothermal aging at 170 °C after different pre-aging (PA) times; heat-treatment histories and symbols as in Fig. 3.

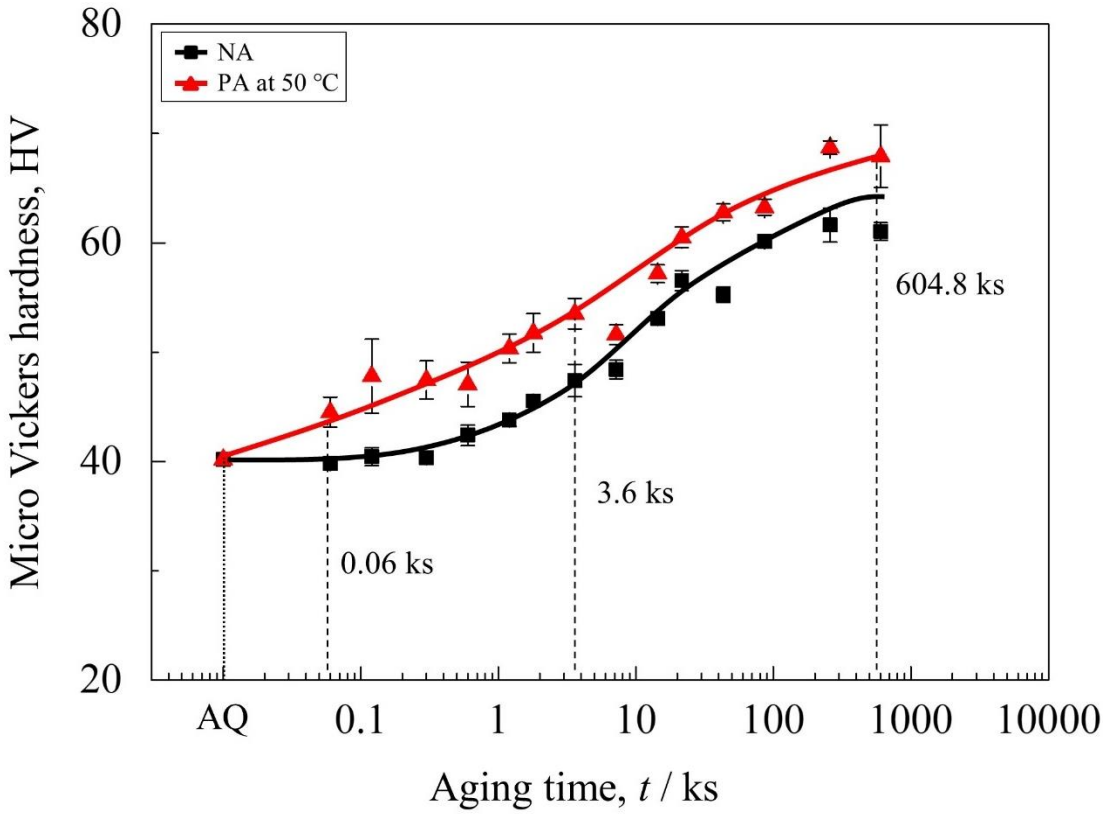


Figure 3.5 Age-hardening curves during single aging at room temperature and 50 °C.

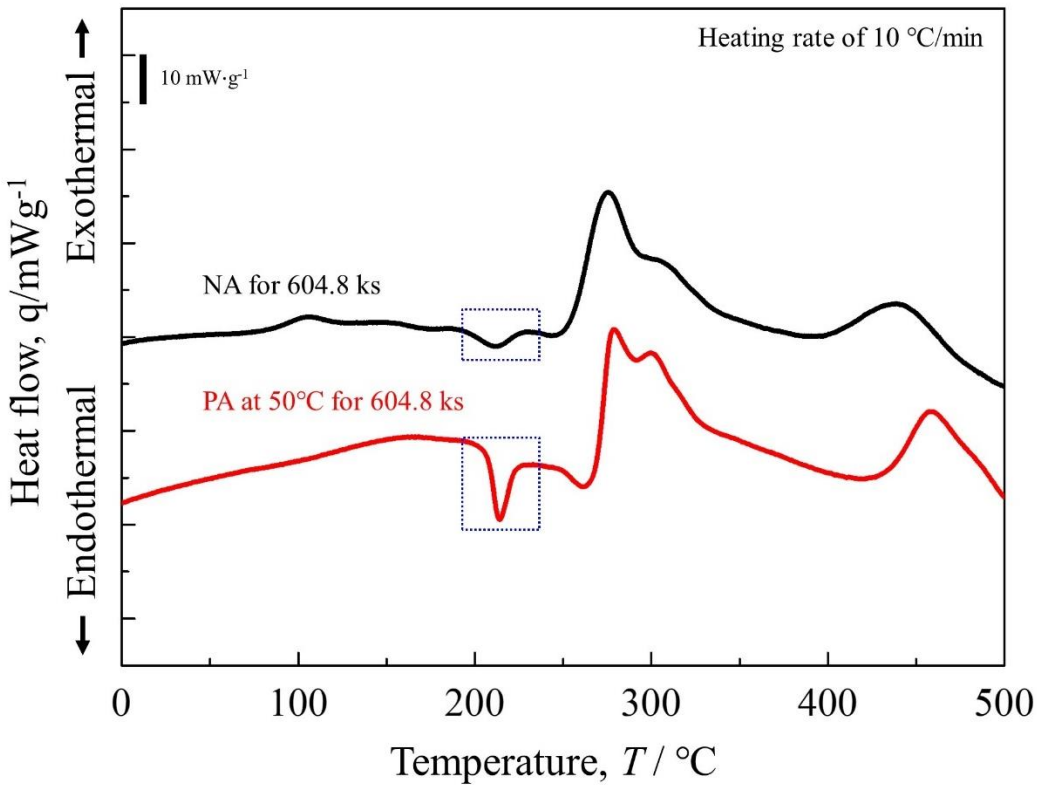


Figure 3.6 The DSC thermograms for the samples aged with different heat treatment. The nanocluster dissolution peaks are marked as blue dotted square.

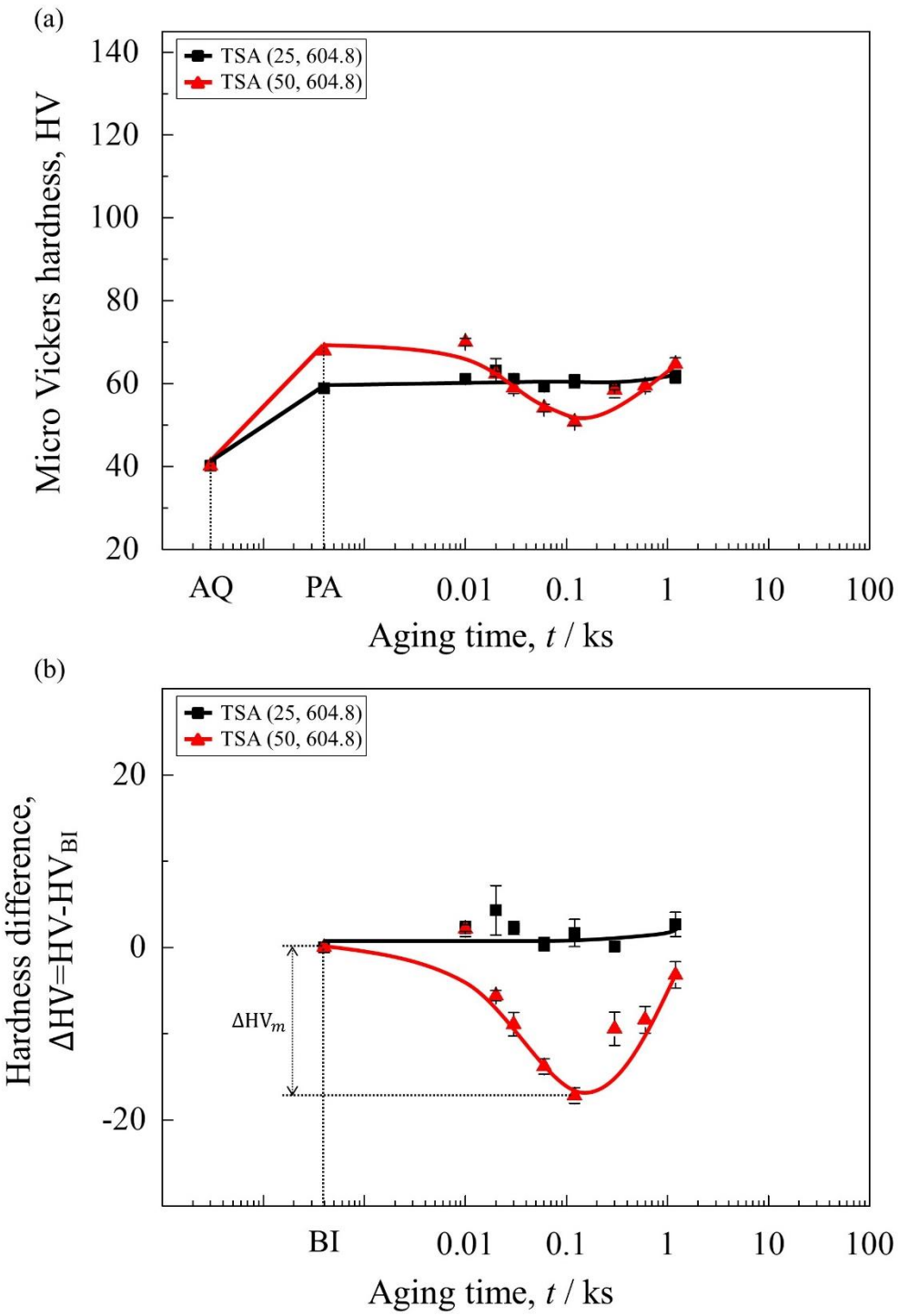


Figure 3.7 (a) The hardness changes and (b) hardness difference (ΔHV) at the early stage of two-step aging at 170 ℃ after natural aging for 604.8 ks and pre-aging at 50 ℃ for 604.8 ks. ΔHV is obtained as the difference value of the obtained hardness during the two-step aging from before isothermal aging at 170 ℃.

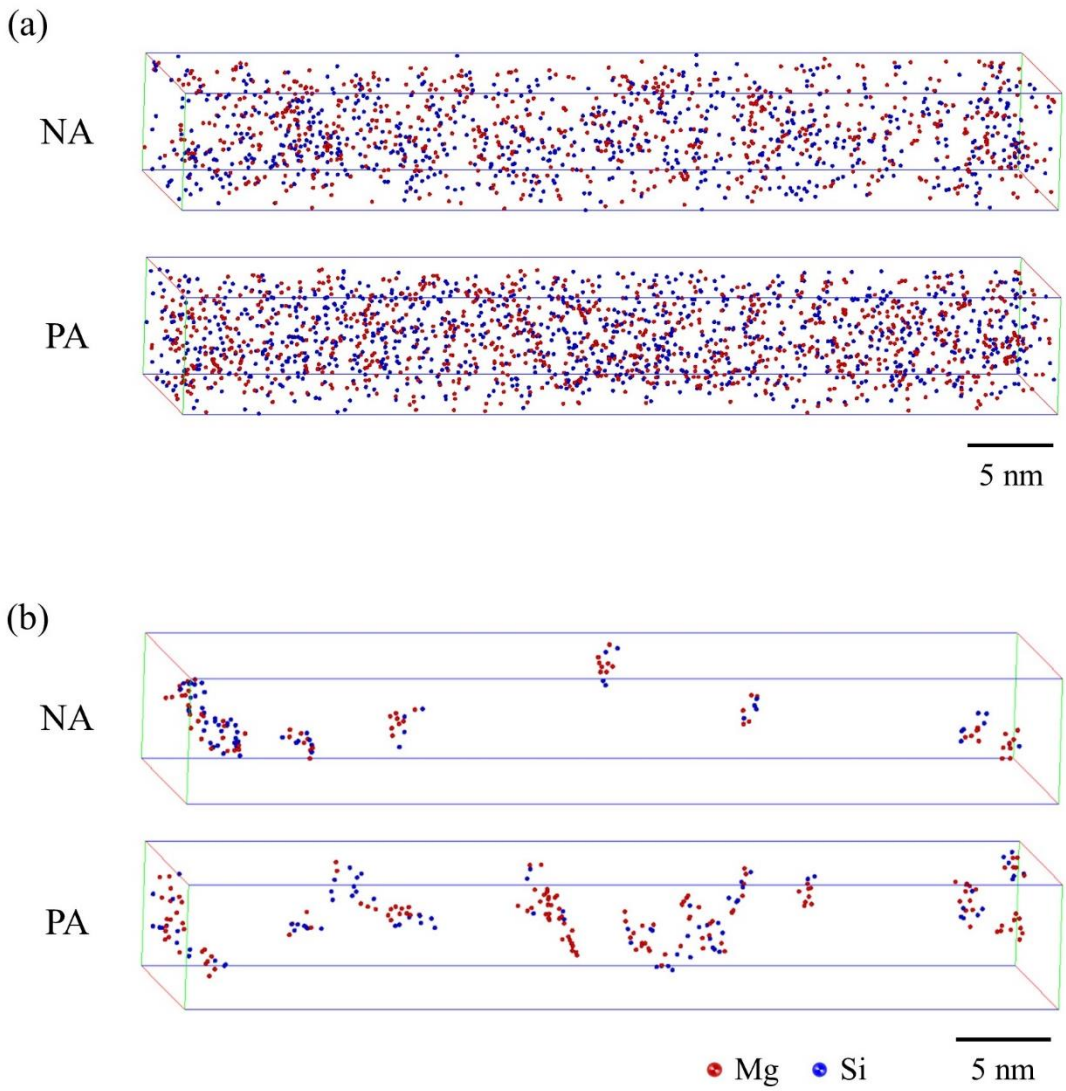


Figure 3.8 . APT maps showing the distribution of (a) all solute atoms in the region of interest, and (b) clusters analyzed by applying the maximum separation method [58,59] after natural aging and pre-aging at 50 ℃ for 604.8 ks. The maximum separation distance between atoms ($D_{max}$) and the minimum number of atoms ($N_{min}$) were chosen as 0.75 nm and 10 solute atoms, respectively. Red and blue spheres represent the Mg and Si atoms, respectively. The analyzed area for (a) all solute atoms and (b) clusters are slightly different since the regions where the clusters have not been analyzed were excluded.

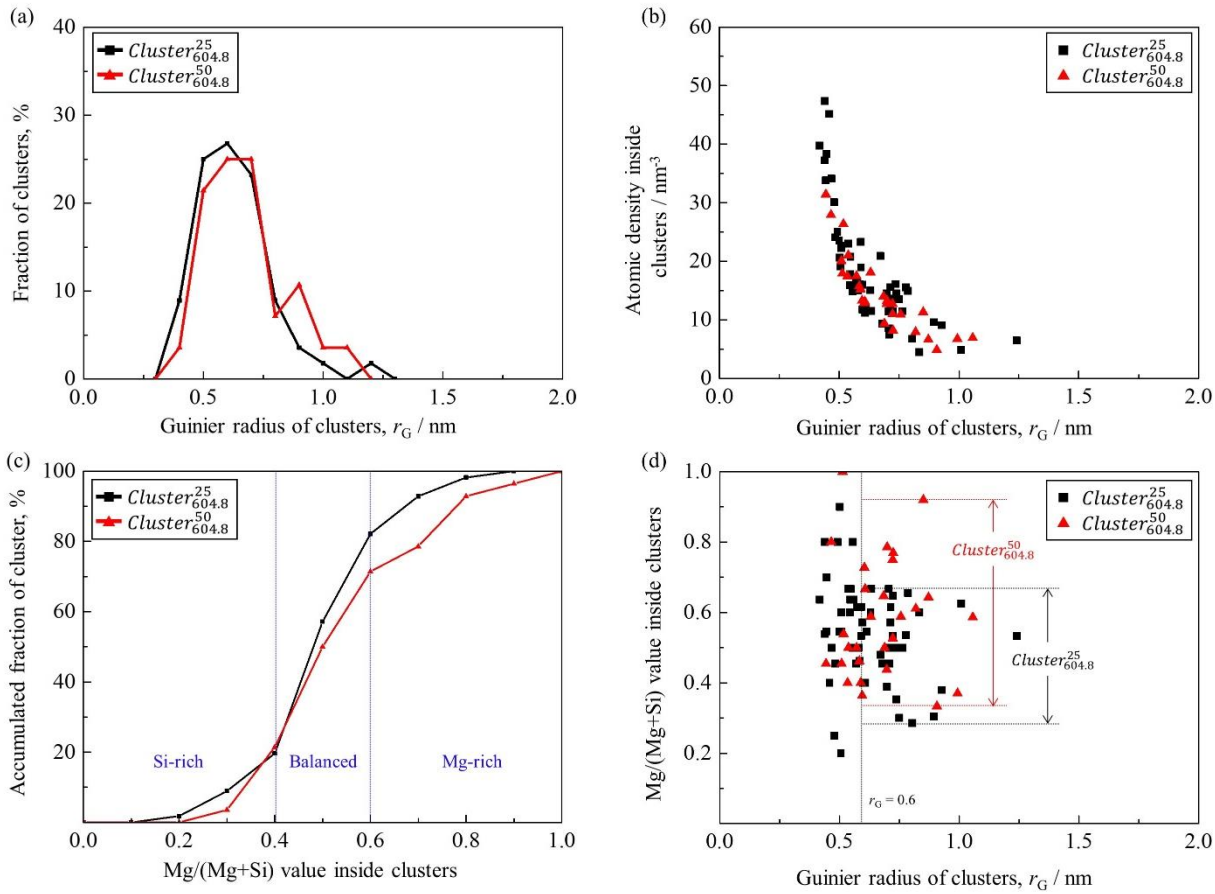


Figure 3.9 APT analysis result after natural aging and pre-aging at 50 ℃. The characteristics of clusters [(a) fraction with size, (b) atomic density with size, (c) accumulated fraction with Mg/(Mg+Si) and (d) Mg/(Mg+Si) with size] are visualized. The Si-rich, Balanced and Mg-rich in (c) represent Mg/(Mg+Si) < 0.4, 0.4 ≤ Mg/(Mg+Si) ≤ 0.6 and Mg/(Mg+Si) > 0.6, respectively. The range of Mg/(Mg+Si) distribution of $Cluster^{25}_{604.8}$ and $Cluster^{50}_{604.8}$ corresponding to $r_G \geq 0.6$ nm are marked in (d).

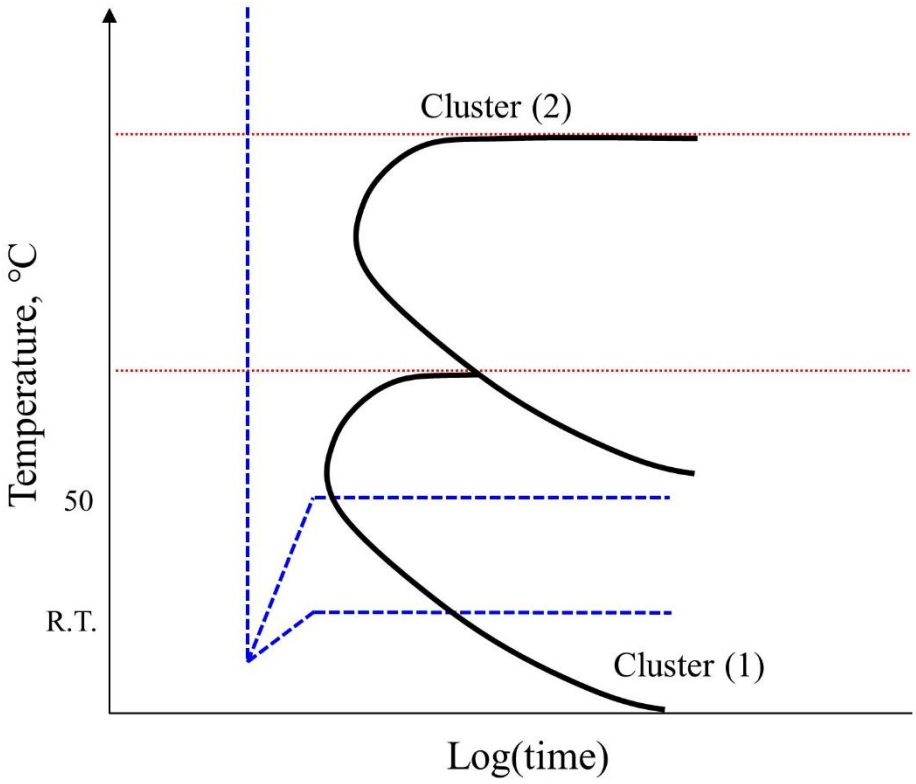


Figure 3.10 Schematic diagram of time-temperature transformation (TTT) curve only for clusters in Al-Mg-Si alloy. The TTT curve shows the transformation taken place in two distinct stages. The red line represents the solvus temperature of each phase. The blue line represents heat treatment history of natural aging and pre-aging at 50 ℃.

# Chapter 4

# Interatomic structure as a determining factor of thermal stability of nanoclusters in Al-Mg-Si alloy

## 4.1 Introduction

The two-step aging behavior was strongly affected by the nanocluster formation during pre-aging before artificial aging [1]. The effect of pre-aging on the early stage of two-step aging is related to the thermal stability of the cluster in Al-Mg-Si alloys. A model for reversion of GP zone based on the critical size, was introduced in aluminum alloy [2]. Clusters smaller than critical size were dissolved, but clusters lager than critical size transform into more stable phase. Some reference studies with similar idea were introduced [3,4]. Meanwhile, many studies mentioned the thermal stability of clusters in Al-Mg-Si alloys [5–10]. Kim et al. [6] confirmed that the thermal stability of the nanoclusters in the Al-Mg-Si alloy changes with the NA time, and they proposed that the thermal stability of nanoclusters is not fully dependent on the size of the nanoclusters but is strongly influenced by the internal structure of the nanoclusters [6]. However, direct experimental evidence was not sufficiently presented. Aruga et al. [8] introduced that Mg-enriched clusters based on direct observation using APT are thermally unstable regardless of alloy composition. On the other hand, Poznak et al. [9] reported that even Mg-enriched clusters in excess-Mg alloy were thermally stable unlike in excess-Si alloy. It means that there is limitation to conclude the thermal stability of cluster based on the information for chemical composition of the cluster. In this study, therefore, we investigated the cluster evolution during low temperature pre-aging at 50 °C and the role of those clusters

in the early stage of two-step aging through elaborating the atomic distribution using advanced analytical method.

## 4.2 Experimental procedure

As described in Section 3.2.

## 4.3 Results

As described in Section 3.3.

## 4.4 Discussion

Serizawa et al. [5] investigated the dissolution of $Cluster_{3.6}^{25}$ in the Al-1.05% Mg-0.78% Si (mass%) alloy using electrical resistivity and APT. They confirmed that the $Cluster_{3.6}^{25}$ was stable and not dissolved at temperatures below 180 ℃, and was unstable at temperatures above 200 ℃ and dissolved [5]. Kim et al. [11] studied the two-step aging behavior with the NA time up to 31,536 ks (approximately 1 year) in the Al-0.6% Mg-1.0% Si (mass%) alloy based on the hardness and electrical resistivity results. Cluster (1) formed after middle stage was dissolved at 170 ℃, and the amount of dissolution increased as the NA time increased [11]. The nanocluster dissolution peaks were observed after NA and PA for 604.8 ks (see Fig. 3.6). The peak area of this peak after PA for 604.8 ks is two times wider than that after NA for 604.8 ks (see Fig. 3.6). At the early stage of two-step aging, there is an increase in hardness of the TSA (25, 604.8) delay, whereas the hardness of TSA (50, 604.8) decreases (see Fig. 3.7). The decrease in hardness at the early stage of two-step aging occurs when the decrease in hardness due to nanocluster dissolution is greater than the increase in hardness due to newly formed

precipitates. Namely, clusters formed after NA for 604.8 ks are thermally stable, but clusters formed after PA for 604.8 ks are thermally unstable at the initial stage of two-step aging. Generally, researchers believe that the dissolution of the precipitate is dependent on the critical size ($r^*$) of the nucleus [12]. Also, the dissolution behavior of the GP zone in Al-Mg-Si alloys has been explained based on their critical size [2–4]. The $Cluster_{604.8}^{25}$ and $Cluster_{604.8}^{50}$ are similar in size, but it was found that the number density of the $Cluster_{604.8}^{50}$ was about twice as high as that of the $Cluster_{604.8}^{25}$ (see Table 3.3). It draws that thermal stability is not fully affected by the number density and size of clusters. Kim et al. [11] proposed that the Si-rich cluster is thermally stable and does not dissolve, while the Mg-Si co-cluster is thermally unstable and dissolves in two-step aging at 170 ℃. Aruga et al. [8] described the thermal stability of a cluster by comparison of composition change inside the cluster using APT and Mg-enriched cluster is easy to be dissolved during two-step aging. On the other hand, Mg-enriched cluster in excess-Mg alloy is thermally stable. Namely, there was limitation to explain the thermal stability of clusters based on chemical composition of the cluster. Therefore, it is necessary to investigate the relationship between the interatomic structure of cluster and thermal stability.

We investigated the details of atomic arrangement by applying normalization based on the gyration radius ($l_g$) [13] of the cluster at which the distribution of solute atoms from center of the cluster to the aluminum matrix can be understood. We analyzed the solute atom concentration profile of $Cluster_{604.8}^{25}$ and $Cluster_{604.8}^{50}$ to investigate the atomic arrangement of clusters. To help understand the concentration profile method, the schematic diagram is shown in Fig. 4.1. The maximum extent of each cluster is normalized to x=1.0 nm based on the $l_g$. It was analyzed with a step size of 0.2 nm up to the maximum extent that 2 nm. x<1.0 nm is the inside of the cluster, x=1 nm is the matrix-cluster interface, and x>1 nm is the

matrix. In order to investigate whether there is a difference in internal structure depending on the size of the cluster, additional analysis was conducted by separating the large radius from the small radius. Large and small clusters correspond to the upper 36% of $r_G$ ($r_G \geq 0.80$ nm) and the lower 36% of $r_G$ ($r_G \leq 0.53$ nm), respectively. The number of analyzed clusters for 36% $Cluster_{604.8}^{25}$ and $Cluster_{604.8}^{50}$ are 10 and 20, respectively. Figure 4.2 shows the results of the solute atoms concentration profile of $Cluster_{604.8}^{25}$ and $Cluster_{604.8}^{50}$. Figures 4.2(a), (b) and (c) give the results of all the clusters, large clusters and small clusters, respectively. The solid line is $Cluster_{604.8}^{25}$, and the dotted line is $Cluster_{604.8}^{50}$. The red dashed square represents the balanced region. In Fig. 4.2(a), Mg/(Mg+Si) inside $Cluster_{604.8}^{25}$ and $Cluster_{604.8}^{50}$ are distributed in the range of 0.34-0.67 and 0.44-0.65, respectively. In Fig. 4.2(b), Mg/(Mg+Si) inside $Cluster_{604.8}^{25}$ and $Cluster_{604.8}^{50}$ are distributed in the range of 0.40-0.63 and 0.40-0.80, respectively. In Fig. 4.2(c), Mg/(Mg+Si) inside $Cluster_{604.8}^{25}$ and $Cluster_{604.8}^{50}$ are distributed in the range of 0.17-0.79 and 0.33-0.71, respectively. The distribution of Mg/(Mg+Si) inside the cluster with the cluster size is visualized in Fig. 4.3. This schematic diagram was drawn based on the results of Figs. 4.2(b) and (c). Each saturation represents the Mg/(Mg+Si) value. In the case of large clusters, Mg/(Mg+Si) inside $Cluster_{604.8}^{25}$ are distributed in the balanced, while Mg/(Mg+Si) inside $Cluster_{604.8}^{50}$ near the matrix-cluster interface are distributed in the Mg-rich. It is first finding to clearly show the Mg-rich cluster with the core-shell structure after long aging time at the low aging temperature in Al-Mg-Si alloys. Meanwhile, it is good agreement with the literatures reporting that Si-rich clusters are formed at the early stage of aging and followed by Mg-enrichment [14–19]. Therefore, we concluded that the Mg-rich clusters with core-shell structure cause dissolution at the initial

stage of two-step aging. Namely, the thermal stability of a cluster depends on the atomic arrangement inside the cluster rather than the size of the cluster.

## 4.5 Conclusions

We investigated the determining factor of thermal stability of the nanoclusters at the initial stage of two-step aging in the Al-0.6% Mg-0.6% Si (mass%) alloy by hardness, DSC measurements and APT analyses. The summary of the main findings is as follows.

- The atomic arrangement of a cluster was further analyzed normalization based on the gyration radius of a cluster. Composition distribution of solute atoms from the center of a cluster to the cluster-matrix interface could be elaborated. In the case of large clusters (upper 36% of $r_G$), the Balanced clusters were confirmed in NA specimen, while the Mg-rich clusters with core-shell structure were confirmed in PA specimen. Initially formed clusters evolve into Mg-rich clusters with core-shell structure after long aging time at the low aging temperature such as aging at 50 ℃ for 604.8 ks, resulting in a thermally unstable at the initial stage of two-step aging. The thermal stability of a cluster at the early stage of two-step aging depends on the atomic arrangement, namely, the composition distribution inside the cluster rather than the size of the cluster. Those results are direct experimental evidence that the thermal stability of the nanoclusters depend not only on the Mg/Si ratio, but also on the position of atoms inside clusters.

## References

[1] J. Kim, Effects of Microalloying Elements on Nanocluster Formation and Age-hardening Behavior during Multi-step Aging in Al-Mg-Si alloys, Tokyo Institute of Technology, 2012.

[2] G.W. Lorimer, R.B. Nicholson, Further results on the nucleation of precipitates in the Al-Zn-Mg system, Acta Metall. 14 (1966) 1009–1013. https://doi.org/10.1016/0001-6160(66)90229-X.

[3] D.W. Pashley, M.H. Jacobs, J.T. Vietz, The basic processes affecting two-step ageing in an Al-Mg-Si alloy, Philos. Mag. 16 (1967) 51–76. https://doi.org/10.1080/14786436708229257.

[4] M. Murayama, K. Hono, Pre-precipitate clusters and precipitation processes in Al–Mg–Si alloys, Acta Mater. 47 (1999) 1537–1548. https://doi.org/10.1016/S1359-6454(99)00033-6.

[5] A. Serizawa, S. Hirosawa, T. Sato, 3DAP Characterization and Thermal Stability of Nano-Scale Clusters in Al-Mg-Si Alloys, Mater. Sci. Forum. 519–521 (2006) 245–250. https://doi.org/10.4028/www.scientific.net/MSF.519-521.245.

[6] J. Kim, S. Kim, E. Kobayashi, T. Sato, Thermal stability and transition behavior of nanoclusters during two-step aging at 250 °C in Al-Mg-Si(-Cu) alloys, Mater. Trans. 55 (2014) 768–773. https://doi.org/10.2320/matertrans.M2013411.

[7] Y. Aruga, M. Kozuka, Y. Takaki, T. Sato, Formation and reversion of clusters during natural aging and subsequent artificial aging in an Al–Mg–Si alloy, Mater. Sci. Eng. A. 631 (2015) 86–96. https://doi.org/10.1016/j.msea.2015.02.035.

[8] Y. Aruga, S.N. Kim, M. Kozuka, E. Kobayashi, T. Sato, Effects of cluster characteristics on two-step aging behavior in Al-Mg-Si alloys with different Mg/Si ratios and natural aging periods, Mater. Sci. Eng. A. 718 (2018) 371–376. https://doi.org/10.1016/j.msea.2018.01.086.

[9] A. Poznak, R.K.W. Marceau, P.G. Sanders, Composition dependent thermal stability and evolution of solute clusters in Al-Mg-Si analyzed using atom probe tomography, Mater. Sci. Eng. A. 721 (2018) 47–60. https://doi.org/10.1016/j.msea.2018.02.074.

[10] M.Y. Song, J.H. Kim, Microstructural evolution at the initial stage of two-step aging in an Al-Mg-Si alloy characterized by a three dimensional atom probe, Mater. Sci. Eng. A. 815 (2021) 141301. https://doi.org/10.1016/j.msea.2021.141301.

[11] J. Kim, E. Kobayashi, T. Sato, Influence of Natural Aging Time on Two-Step Aging Behavior of Al-Mg-Si(-Cu) Alloys, Mater. Trans. 56 (2015) 1771–1780. https://doi.org/10.2320/matertrans.L-M2015824.

[12] D.A. Porter, K.E. Easterling, M.Y. Sherif, Phase Transformations in Metals and Alloys, third ed., Taylor & Francis Group, Boca Raton, FL., 2009.

[13] M.K. Miller, R.G. Forbes, Atom-Probe Tomography, 1st ed., Springer US, Boston, MA, 2014. https://doi.org/10.1007/978-1-4899-7430-3.

[14] A.K. Gupta, D.J. Lloyd, Study of precipitation kinetics in a super purity Al-0.8 pct Mg-0.9 pct Si alloy using differential scanning calorimetry, Metall. Mater. Trans. A. 30 (1999) 879–884. https://doi.org/10.1007/s11661-999-0081-1.

[15] J. Banhart, M.D.H. Lay, C.S.T. Chang, A.J. Hill, Kinetics of natural aging in Al-Mg-Si alloys studied by positron annihilation lifetime spectroscopy, 014101 (2011) 1–13. https://doi.org/10.1103/PhysRevB.83.014101.

[16] C.S.T. Chang, J. Banhart, Low-Temperature Differential Scanning Calorimetry of an Al-Mg-Si Alloy, Metall. Mater. Trans. A. 42 (2011) 1960–1964. https://doi.org/10.1007/s11661-010-0596-5.

[17] M.D.H. Lay, H.S. Zurob, C.R. Hutchinson, T.J. Bastow, A.J. Hill, Vacancy Behavior and Solute Cluster Growth During Natural Aging of an Al-Mg-Si Alloy, (2012). https://doi.org/10.1007/s11661-012-1257-7.

[18] Y. Aruga, M. Kozuka, Y. Takaki, T. Sato, Evaluation of Solute Clusters Associated with Bake-Hardening Response in Isothermal Aged Al-Mg-Si Alloys Using a Three-Dimensional Atom Probe, Metall. Mater. Trans. A. 45 (2014) 5906–5913. https://doi.org/10.1007/s11661-014-2548-y.

[19] V. Fallah, B. Langelier, N. Ofori-Opoku, B. Raeisinia, N. Provatas, S. Esmaeili, Cluster evolution mechanisms during aging in Al-Mg-Si alloys, Acta Mater. 103 (2016) 290–300. https://doi.org/10.1016/j.actamat.2015.09.027.

## Tables

## Figures

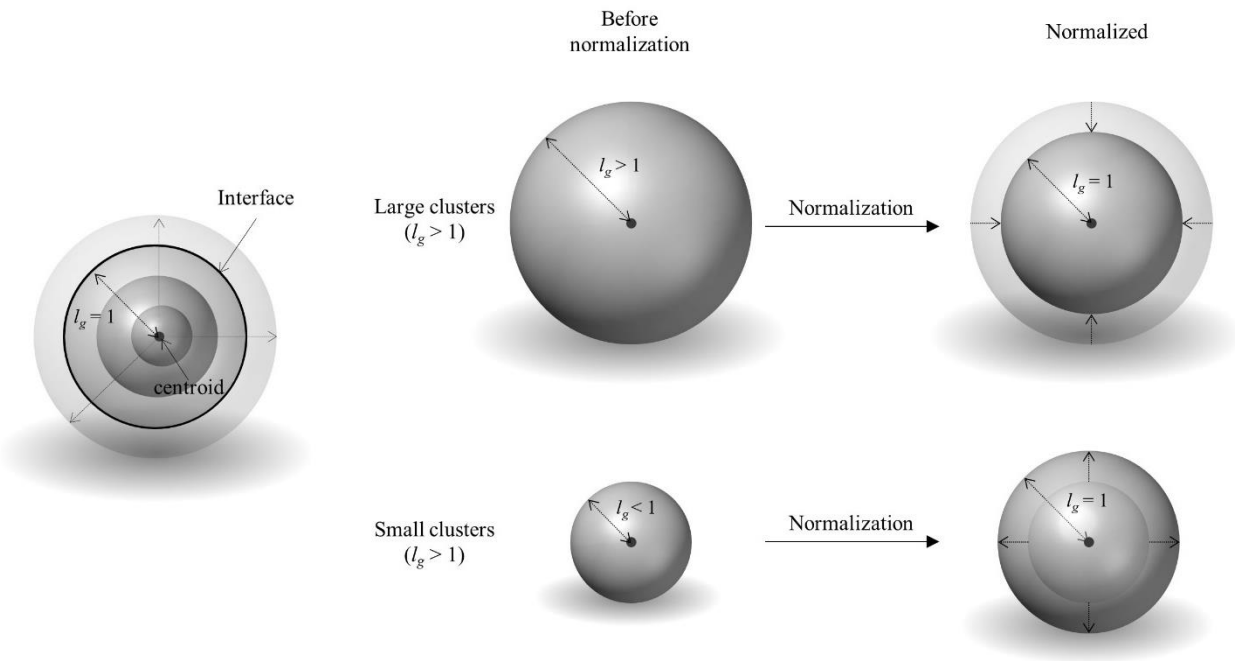


Figure 4.1 Schematic diagram of the concentration profile method from the center of a cluster to matrix. The maximum extent of each cluster is normalized to x=1.0 nm based on the gyration radius ($l_g$). Axis normalized distance of 0, 1.0 and 2.0 nm represent the center of a cluster, cluster-matrix interface and the two times of the cluster radius, respectively.

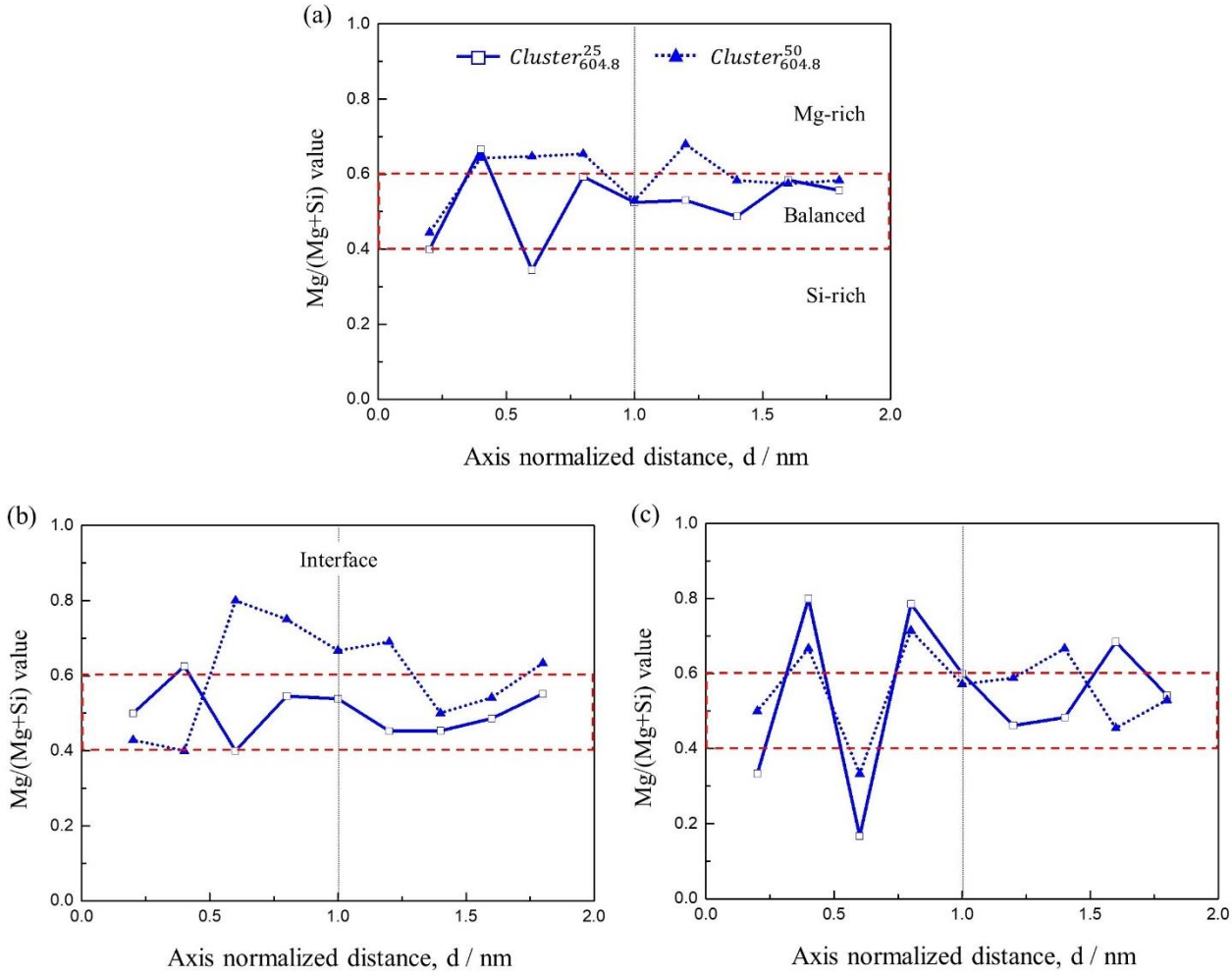


Figure 4.2 Concentration profile of the (a) all, (b) large and (c) small clusters formed during natural aging and pre-aging at 50 °C. Solid and dotted line are $Cluster_{604.8}^{25}$ and $Cluster_{604.8}^{50}$, respectively. Large and small clusters correspond to the upper 36% of $r_G$ ($r_G \geq 0.80$ nm) and lower 36% of $r_G$ ($r_G \leq 0.53$ nm), respectively. The number of analyzed clusters for 36% $Cluster_{604.8}^{25}$ and $Cluster_{604.8}^{50}$ are 10 and 20, respectively. The red dashed square represents the balanced region.

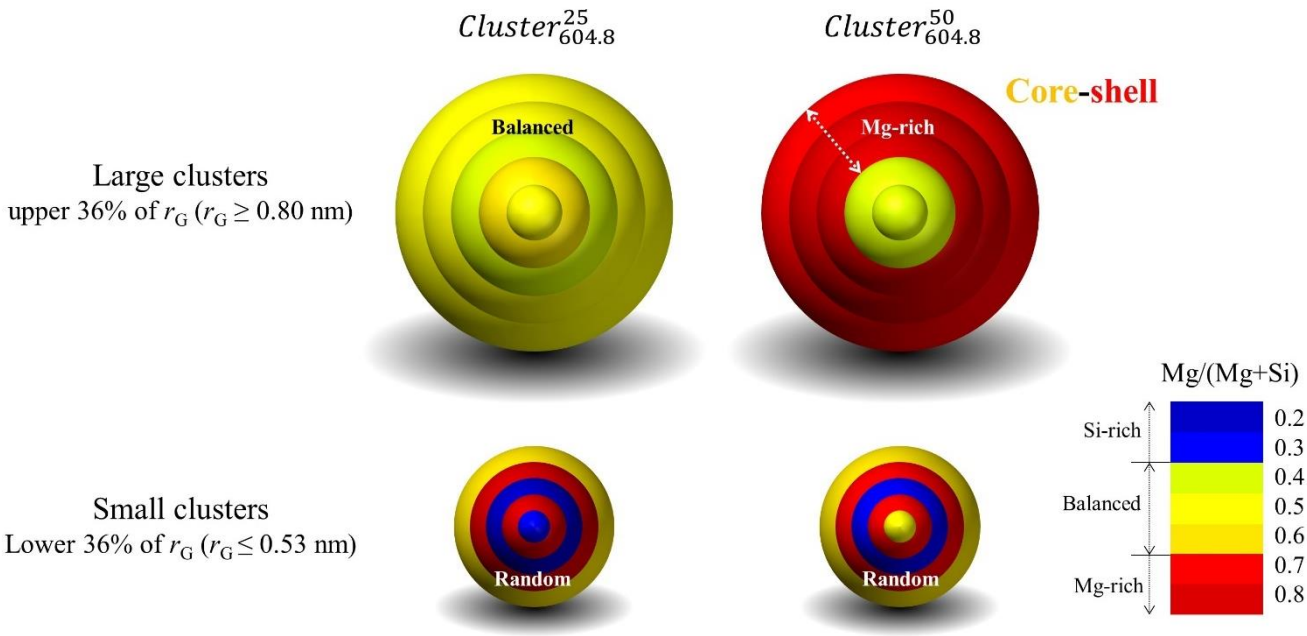


Figure 4.3 Visualization of Mg/(Mg+Si) distribution inside $Cluster_{604.8}^{25}$ and $Cluster_{604.8}^{50}$ with cluster size. This schematic diagram is drawn based on the results of Fig. 11(b) and (c). Each saturation represents the Mg/(Mg+Si) value based on Fig. 11(b) and (c). Top, bottom, left and right side represent the large cluster, small cluster, $Cluster_{604.8}^{25}$ and $Cluster_{604.8}^{50}$, respectively. It can be seen that the large $Cluster_{604.8}^{50}$ are the Mg-rich clusters with core-shell structure.

# Chapter 5

# Correlation between nanocluster evolution and aging temperature in Al-Mg-Si alloy

## 5.1 Introduction

As introduced in Section 1.3.3, nanoclusters formed at the early stage of phase decomposition in Al-Mg-Si alloys have two distinct clustering pathways depending on the temperature. The clusters formed at low temperatures (e.g. natural aging) cannot directly transition, whereas clusters formed at relatively high temperatures (e.g. 100 ℃) are precursors that can continuously evolve [1,2]. This means that two distinct types of clusters with their own characteristics are formed depending on the aging temperature. The differential scanning calorimetry (DSC) is useful for determining the formation temperature of precipitates. Figure 5.1(a) shows the DSC thermogram of the as-quenched Al-0.9% Mg-1.0% Si (mass %) alloy. In the DSC thermogram of the Al-Mg-Si alloys, the heat evolution due to the formation of nanoclusters, that is, the nanocluster formation peak, is confirmed [2–6]. Figure 5.1(b) shows the result of peak separation of nanocluster formation peak, indicated by the red dashed line in Fig. 5.1(a), using a Gaussian function. Peak 1 formed at low temperature (about 50 ℃) and peak 2 formed at high temperature (about 80 ℃) can be confirmed. There are different perspectives to explain the origins of these peaks. Serizawa et al. [2] reported that peaks 1 and 2 are related to the formation of Cluster (1) and Cluster (2), respectively, and that they are formed competitively. Their study suggests that peak 1 and peak 2 are heat evolution by independent reactions. On the other hand, Gupta et al. [3] reported that peaks 1 and 2 are

derived from the formation of Si-rich clusters and Mg incorporation into Si-rich clusters, respectively. Chang et al. [5,7] introduced that the peak 1 and peak 2 are related to Si-related and Mg-related reactions. From the studies of Gupta et al. [3] and Chang et al. [5,7], it is noted that the peak 2 corresponds to a subsequent reaction following Peak 1. This controversial issues regarding peak 1 and peak 2 arise from the limitations of analyzing the characteristics of the nanoclusters formed at different aging temperatures. So far, various studies [2,8–10] have reported differences in the size, composition, and vacancy concentration of the nanoclusters. However, despite these attempts, the difference in the characteristics of nanoclusters that explain the distinct clustering evolution are not clearly understood. New approach other than the existing characterization methods is needed.

It is well known that there are numerous metastable phases in Al-Mg-Si alloys. These precipitates have structure relation such as Si-network [11–13] and Mg-eye [14–16]. It is considered that the atomic structure of the precipitates is essential in understanding their transition behavior. Ravi and Wolverton [17] investigated the thermodynamic phase stability of metastable phases in Al-Mg-Si by performing first-principles calculations to calculate the energies of structures with different Mg/Si ratios. It is noted that there exists a proper structure, i.e. energetically favorable, which enables the precedent phase to evolve into a more stable phase. Nanoclusters are also assumed to have specific interatomic structures, which will be useful for understanding their clustering evolution. Referring back to the Fig. 5.1, at 40 and 70 ℃, both the reactions corresponding to peak 1 and peak 2 are dominant, distinguishing them from room temperature and 100 ℃ where only one of the reactions is present. The reaction peak 1 seems to be completed within 3.6 ks at room temperature [2,3,5]. Therefore, it is necessary to investigate the clustering evolution at given aging temperatures (room temperature,

40, 70, and 100 ℃) and the difference in characteristics of clusters formed during 3.6 ks at these temperatures focused on their interatomic structure analysis.

## 5.2 Experimental procedure

1.0 mm thick sheets with Al-0.9Mg-1.0Si (mass %) alloy provided by UACJ Corp. (Japan) were used. The sheets were fabricated in size of 10×10 mm before heat treatment. The samples were solution heat treated (ST) at 560 ℃ for 1.8 ks in a salt bath containing a 1:1 mixture of $KNO_3$ and $NaNO_3$ powder, and then quenched in ice water at 0 ℃ for 0.06 ks. Each solution heat-treated alloy was undergone four separate heat treatment procedures; Final aging for 3.6 ks at room temperature, 40, 70 and 100 ℃ were performed using Silicone Oil (Shin-Etsu, KF-96 1000CS) bath. Those specimens are marked as NA (natural aging), 40, 70, and 100 ℃. After the final aging, the specimen was properly prepared according to the follow-up experiment, and the detailed preparation processes are as follows.

The thermal analysis of specimens was conducted using a differential scanning calorimeter (DSC 204 F1 phoenix, NETZSCH) under a nitrogen gas atmosphere with 99.999% purity. The DSC test began at -50 ℃ and was heated to 500 ℃ at a rate of 10 ℃/min, while liquid nitrogen was utilized to stabilize the data. The specimens were made with a weight of 40 ± 0.05 mg and a disc height of 1 mm, and placed in a pure aluminum crucible with a pierced lid.

The APT samples were prepared using a cryogenic-focused ion beam (Helios NanoLab 600, FEI) while keeping the specimens under liquid nitrogen to prevent them from being exposed to room temperature or any temperature increase during FIB milling. During the milling process, a platinum capping process was applied to the sample apex to avoid any gallium implantation that could result in incorrect composition or even amorphization of crystalline regions [18,19]. The APT experiments were performed using a local electrode atom probe

(LEAP 4000X HRTM, CAMECA Instruments Inc.) in the voltage pulsed mode with a pulse fraction of 20% at an operating temperature of approximately -223 °C and a vacuum pressure of up to 2.7 x $10^{-11}$.

The IVAS 3.8.12 software was utilized to process APT data, including reconstruction and visualization. It is important to perform a careful reconstruction to ensure data reliability and reproducibility since cluster analysis by APT relies on reconstruction. In this study, some key reconstruction methods are demonstrated. The low-index poles were deliberately excluded to maintain depth resolution integrity and avoid ion trajectory aberrations. The image compression factor and k-factor, which are key input parameters for tomographic reconstruction, were calibrated based on a crystallographic calibration method [20] that matches the theoretically and experimentally measured interplanar spacing. The spatial distribution maps [21] were utilized to measure the interplanar spacing. The measured Mg/(Mg+Si) of NA, 40, 70 and 100 °C samples are 0.52, 0.51, 0.52 and 0.54, respectively. The cluster analysis was performed using density-based application of spatial clustering (DBSCAN), one of the cluster identification algorithms introduced in Chapter 2. The user-defined parameters ($D_{max}$, $N_{min}$ and order) were determined by the method as mentioned in Section 2.2.2. Figure 5.2 shows the size distribution of clusters for all specimens with $D_{max}$ obtained on the basis of 1st-order. Since the number of identified clusters in the specimen at 100 °C was too small to analyze, the $D_{max}$ and $N_{min}$ for this specimen were determined based on 2nd-order, whereas those for the other specimens were decided based on 1st-order. Table 5.1 shows the user-defined parameters for all samples applied in the study.

## 5.3 Results

### 5.3.1 Thermal analysis

Figure 5.3 shows change in DSC thermograms after different aging temperatures for 3.6 ks. There are several exothermal and endothermal peaks derived from the sequential reactions during linear heating. From low temperature, it represents nanocluster formation (2), β″ nuclei (3), nanocluster dissolution (4), formation of β″ (5) and β′ (6). Since one of the nanocluster formation peaks (peak 1 as shown in Fig. 5.1) disappeared, it is not represented here. The relationship between peak 3 and the β″ nuclei will be elaborated in the discussion section. The peak 3 can be clearly seen in the 70 and 100 ℃ samples. As the aging temperature prior to DSC experiment increases, changes in the peak areas are observed: peak 2 decreases, peak 4 increases and then decreases, and peak 5 decreases. These change in amount of heat evolution and absorption are summarized in Table 5.2. The parts without any noticeable reaction (less than 0.01 $J \cdot g^{-1}$) are left blank.

### 5.3.2 APT analysis

Figure 5.4 illustrate the APT maps before and after applying DBSCAN algorithm with user-defined parameters described in Table 5.1. Only solute atoms are shown. The red and blue dots represent the Mg and Si atoms, respectively. The size of dots does not reflect the actual atomic size. The analyzed volume of R.T., 40, 70 and 100 ℃ specimens are 11282, 8282, 12858 and 13881 $nm^{-3}$, respectively. It can be confirmed that the identified clusters exist in all samples. The statistical data of these identified clusters are summarized in Table 5.3. Number of solute atoms and Mg/(Mg+Si) represent the size and Mg/Si ratio of clusters, respectively. Number density is given by number of clusters over analyzed volume ($nm^{-3}$). As the temperature increases, the size of clusters tends to increase, and Mg/Si ratio decreases and then increases.

Figure 5.5(a) shows fraction with size (i.e. size distribution) of clusters. The step size of number of solute atoms (x-axis) is 5. The sum of the numbers of clusters involved in each step

is represented as a fraction (y-axis). For example, the highest fraction of clusters with 6-10 solute atoms is confirmed in R.T. sample. In the case of the others, clusters with 11-15 solute atoms are the most frequently observed. Clusters with more than 20 solute atoms are observed only in the 70 and 100 ℃ samples. Figure 5.5(b) shows the accumulated fraction with Mg/(Mg+Si) inside clusters. Clusters with Mg/(Mg+Si) <0.4, 0.4≤ Mg/(Mg+Si)≤0.6 and Mg/(Mg+Si)>0.6 are expressed as Si-rich, Balanced and Mg-rich clusters, respectively. the fraction of Si-rich clusters is higher in the RT and 40 ℃ samples, while Mg-rich clusters are more predominant in the 70 ℃ and 100 ℃ samples. The fraction of Balanced clusters in R.T., 40, 70 and 100 ℃ samples are 50 50 36 and 70 %, respectively.

Figure 5.6 shows fraction of Al with Mg/(Mg+Si) inside clusters. Each dot represents a cluster. The size of a dot is proportional to number of solute atoms. The highest Al fraction among the clusters in the R.T. and 40 ℃ samples is 38 and 48 %, respectively. The clusters with Al fraction over 50% were observed only in the 70 and 100 ℃ samples.

Figure 5.7 shows concentration profile of clusters. The details of this analysis can be seen in the previous study [22]. It represents the fraction of solute atoms from the center of clusters ($d$=0) to the matrix-cluster interface ($d$=1). It is confirmed that a tendency of the fraction of solute atoms decreased as the region gets closer to the interface. It seems that clusters formed at lower temperatures have a higher solute atom fraction than clusters formed at higher temperatures. The pink arrows and numbering indicate the differences between the samples at 40 and 70 ℃ samples. The difference value decreases as the region approaches the interface.

Figure 5.8 shows accumulated frequency of first-nearest neighbor (1NN) distance of solute pairs (Mg-Mg and Si-Si). Only the solute atoms involved in clusters were considered. In the case of the R.T. and 40 ℃ samples, the frequency of two types of solute pairs is similar up to 0.55 nm, while Si-Si pairs become predominant beyond that distance. On the other hand, the

frequency of Mg-Mg pairs is consistently higher than that of Si-Si pairs in the 70 ℃ and 100 ℃ samples.

## 5.4 Discussion

### 5.4.1 Difference in clustering behavior with different temperatures

The DSC is powerful tool to analyze the clustering behavior. It enables predicting the clusters formed during heat-treatment prior to DSC running, and their evolution. We performed DSC experiments as shown in Figs. 5.1 and 5.3 and confirmed three key points that can elaborate the clustering behavior with different temperatures. To clearly show some small heat effects, the enlarged heat flow curve of Fig. 5.3 is provided in Fig. 5.9. In the following, these key points are introduced.

First, it was observed that area of peak 4 (nanocluster dissolution peak) increased up to aging temperature of 40 ℃ and then decreased as shown in Table 5.2. The heat absorption in 100 ℃ sample is negligible. The peak 4 is caused by the dissolution of thermally unstable clusters [23]. Thus, it is considered that clusters formed at room temperature and 40 ℃ are thermally unstable unlike the clusters formed at 70 and 100 ℃. Second, it is related to the broad peak 3. As shown inn Fig. 5.9, in the R.T. and 40 ℃ samples, a single exothermic peak 3 was observed, while in the 70 ℃ and 100 ℃ samples, a double exothermic peak 3 was confirmed. Referring from several literatures [24–26], it seems that the broad peak 3 observed before β″ peak is derived from variants of β″ nuclei. It can be inferred that one of the peaks in peak 3 is generated during linear heating (i.e., DSC measurement), while the other peak arises from the transformation of pre-existing clusters formed during aging at 70 and 100 ℃. Based on this result, unlike clusters formed at room temperature and 40 °C, clusters generated at 70 and

100 °C are believed to be capable of direct transition. Third, we confirmed the noticeable decrease in area of peak 5 in 70 and 100 ℃ samples as shown in Table 5.2. There are several kinds of β″ nuclei which energetically favorable to transform to β″ in Al-Mg-Si alloys [15–17]. The transformation of these β″ nuclei to β″ only involves a very small enthalpy change. As mentioned above, there are a lot of β″ nuclei in the 70 and 100 ℃ samples due to pre-existing clusters, resulting in a small amount of heat evolution attributed to β″. From the three key points introduced above, we confirmed two types of clusters with different clustering behaviors under different aging temperatures for 3.6 ks: clusters that are no longer capable of direct evolving were formed at room temperature and 40 ℃, while in contrast, clusters that can continue to evolve were formed at 70 ℃ and 100 ℃. This implies that there is a critical temperature with respect to determining the different clustering behavior. This kind of critical temperature can be seen in some literatures [27,28].

There are two distinct peaks (peak 1 and 2) in nanocluster formation peak as shown in Fig. 5.1. The peak 1 is disappeared in R.T. and 40 ℃ samples, and it is noted that the area of peak 2 in 40 ℃ samples is smaller than that of R.T. sample (see Fig. 5.11). Gupta et al. [3] and Chang et al. [5,7] introduced that the peak 1 and 2 are derived from formation of Si-rich clusters (Si-related activity) and Mg incorporation into the Si-rich clusters, respectively. However, considering that the clusters in the 40 °C sample are more Si-rich on average than the clusters in the R.T. sample (see Table 5.3), it is determined that the reduced areas of peaks 1 and 2 do not match the average composition of the clusters. Meanwhile, the dominant heat evolution at room temperature, 40, 70 and 100 ℃ are peak 1,1,2 and 2, respectively (see Fig. 5.1). This dominant heat evolution at different temperatures is good agreement with the fact that the Mg/(Mg+Si) of the clusters decreases and then increases as shown in Table 5.3. This finding is worth noting.

### 5.4.2 Transition temperature for the formation of interatomic structures

As introduced in Section 5.4.1, we confirmed a critical temperature with respect to determining the different clustering behavior. We found the reasons for their different transition behaviour with respect to the Al concentration and interatomic structure inside clusters. In the following, those reasons are elaborated.

Chen et al. [29] investigated the evolution of nucleus to β″ phase by analyzing the change in composition and atomic structure. The study involved calculations of the volume expansion ratio and formation enthalpy with respect to the solid solution, in addition to TEM analysis. They emphasized that the $Mg_2Si_2Al_7$ (nucleus) is initially formed and it undergoes 1D-growth by replacing the Al with Mg and Si to satisfy certain critical length to evolve to β″. And they introduced that the formation and further evolution of $Mg_2Si_2Al_7$ depends on the aging temperature. We confirmed the Al concentration inside clusters formed at different temperatures from Fig. 5.6. An interesting point is that clusters with Al concentration exceeding 48 % were observed only in the 70 and 100 ℃ samples. In other words, it is suggested that the clusters formed at room temperature and 40 ℃ do not have sufficient amounts of Al to grow further. Huis et al. [15,16] studied the change in formation enthalpies with respect to solid solution during the compositional evolution of $Mg_xSi_xAl_x$. Their calculation results indicate replacing the Al with Mg and Si is essential to become energetically favorable structure. Thus, it is considered that the Al concentration inside clusters is key factor to decide the transition behavior of clusters. However, the following questions arise: whether the clusters with low Al content identified in the 70°C and 100°C samples cannot evolve or if they differ from the clusters formed at RT and 40°C. In order to answer these questions, an introduction about the analysis of the bonding structure inside clusters will follow.

The bonding structure was analyzed by accumulated frequency of 1NN distance of solute pairs ($f_{Mg\text{-}Mg}$ and $f_{Si\text{-}Si}$) from Fig. 5.8. It was confirmed that difference in the bonding structure between the clusters formed at different temperatures. In order to clearly show this difference, the delta frequency ($\Delta f$) was presented as shown in Fig. 5.10. $\Delta f$ indicates difference between $f_{Mg\text{-}Mg}$ and $f_{Si\text{-}Si}$. As $|\Delta f|$ approaches zero, it means that the frequency of two types of solute pairs become similar. In the case of R.T. and 40 ℃ samples, $|\Delta f|$ is nearly zero up to 0.55 nm, then it increases. While, $|\Delta f|$ increases from the beginning in 70 and 100 ℃ samples. This result implies that there are two distinct structures. Moreover, as confirmed in Fig. 5.7, the difference in fraction of solute atoms between the 40 and 70 ℃ samples was confirmed, and it was the greatest in the vicinity of the centroid, despite the clusters in these samples having a similar fraction of solute atoms, as shown in Table 5.3. This discrepancy is thought to come from condensed solute atomic structure as it approaches the core. As a result, even if the clusters with low Al concentration in 70 and 100 ℃ samples, they are considered to have their own characteristics different from those formed in the R.T. and 40 ℃ samples due to the structural differences and are expected that they can evolve continuously. Therefore, we emphasize that there is a transition temperature for the formation of interatomic structure of clusters that determining their evolution.

## 5.5 Conclusions

We investigated the clustering evolution at different temperatures and the difference in nature of the formed clusters in Al-0.9% Mg-1.0% Si (mass %) alloy by DSC and APT. New analysis methods related to interatomic structure of nanoclusters were introduced to characterize them. The different clustering evolution with aging temperature have been well described by those methods. The main findings are as follows.

- DSC experiments were conducted on samples aged for 3.6 ks at different temperatures. In the R.T. and 40 ℃ samples, an increase in the area of the nanocluster dissolution peak and a single peak of β″ nuclei were observed. A double peak of β″ nuclei and a decrease in the area of β″ peak were observed in the 70 and 100 ℃ samples. The DSC experimental results indicate the transition temperatures between 40 and 70 ℃, where clustering evolution is determined.
- From the APT analysis, the average Mg/(Mg+Si) of R.T., 40, 70 and 100 100 ℃ samples were confirmed 0.48, 0.44, 0.53 and 0.56, respectively. The average composition of the clusters formed during a 3.6 ks aging period at different aging temperatures was found to be proportional to the dominant response observed at the corresponding temperature in the DSC curve, which corresponds to the two heat evolution peaks representing Si and Mg.
- Distinct interatomic structural differences were observed between the clusters formed at room temperature and 40 ℃, and those formed at 70 and 100 ℃, based on the analysis of Al concentration, frequency of 1NN distances, and concentration profiles: the clusters formed at room temperature and 40 ℃ had a low Al concentration and a condensed solute atomic structure as it approaches the core, whereas the clusters formed at 70 and 100 ℃ showed a high Al concentration and a evenly distributed solute atomic structure. Those results indicate that the two distinct clustering evolutions are determined by the interatomic structure of the clusters.

**References**

[1] K. Yamada, T. Sato, A. Kamio, Cluster formation and two-step aging behaviors of Al-Mg-Si alloys, Keikinzoku/Journal Japan Inst. Light Met. 51 (2001) 215–221. https://doi.org/10.2464/jilm.51.215.

[2] A. Serizawa, S. Hirosawa, T. Sato, Three-Dimensional Atom Probe Characterization of Nanoclusters Responsible for Multistep Aging Behavior of an Al-Mg-Si Alloy, Metall. Mater. Trans. A. 39 (2008) 243–251. https://doi.org/10.1007/s11661-007-9438-5.

[3] A.K. Gupta, D.J. Lloyd, Study of precipitation kinetics in a super purity Al-0.8 pct Mg-0.9 pct Si alloy using differential scanning calorimetry, Metall. Mater. Trans. A. 30 (1999) 879–884. https://doi.org/10.1007/s11661-999-0081-1.

[4] J. Banhart, C.S.T. Chang, Z. Liang, N. Wanderka, M.D.H. Lay, A.J. Hill, Natural aging in Al-Mg-Si alloys - A process of unexpected complexity, Adv. Eng. Mater. 12 (2010) 559–571. https://doi.org/10.1002/adem.201000041.

[5] C.S.T. Chang, J. Banhart, Low-Temperature Differential Scanning Calorimetry of an Al-Mg-Si Alloy, Metall. Mater. Trans. A. 42 (2011) 1960–1964. https://doi.org/10.1007/s11661-010-0596-5.

[6] J. Kim, J. Im, M. Song, I. Kim, Effects of Mg Addition and Pre-Aging on the Age-Hardening Behavior in Al-Mg-Si, Metals (Basel). 8 (2018) 1046. https://doi.org/10.3390/met8121046.

[7] C. Sin, T. Chang, Z. Liang, E. Schmidt, J. Banhart, Influence of Mg / Si ratio on the clustering kinetics in Al – Mg – Si alloys, 103 (2012) 955–961.

[8] M. Torster, H.S. Hasting, W. Lefebvre, C.D. Marioara, J.C. Walmsley, S.J. Andersen, R. Holmestad, The influence of composition and natural aging on clustering during preaging in Al-Mg-Si alloys, J. Appl. Phys. 108 (2010) 1–9. https://doi.org/10.1063/1.3481090.

[9] M.W. Zandbergen, Q. Xu, A. Cerezo, G.D.W. Smith, Study of precipitation in Al–Mg–Si alloys by Atom Probe Tomography I. Microstructural changes as a function of ageing temperature, Acta Mater. 101 (2015) 136–148. https://doi.org/10.1016/j.actamat.2015.08.017.

[10] A. Poznak, R.K.W. Marceau, P.G. Sanders, Composition dependent thermal stability and evolution of solute clusters in Al-Mg-Si analyzed using atom probe tomography, Mater. Sci. Eng. A. 721 (2018) 47–60. https://doi.org/10.1016/j.msea.2018.02.074.

[11] S.J. Andersen, C.D. Marioara, R. Vissers, A. Frøseth, H.W. Zandbergen, The structural relation between precipitates in Al-Mg-Si alloys, the Al-matrix and diamond silicon, with emphasis on the trigonal phase U1-$MgAl_2Si_2$, Mater. Sci. Eng. A. 444 (2007) 157–169. https://doi.org/10.1016/j.msea.2006.08.084.

[12] H.S. Hasting, A.G. Frøseth, S.J. Andersen, R. Vissers, J.C. Walmsley, C.D. Marioara, F. Danoix, W. Lefebvre, R. Holmestad, Composition of β″ precipitates in Al-Mg-Si alloys by atom probe tomography and first principles calculations, J. Appl. Phys. 106 (2009). https://doi.org/10.1063/1.3269714.

[13] M. Torsaeter, W. Lefebvre, C.D. Marioara, S.J. Andersen, J.C. Walmsley, Study of intergrown L and Q′ precipitates in Al–Mg–Si–Cu alloys, 64 (2011) 817–820. https://doi.org/10.1016/j.scriptamat.2011.01.008.

[14] H.W. Zandbergen, S.J. Andersen, J. Jansen, Structure determination of $Mg_5Si_6$ particles in Al by dynamic electron diffraction studies, Science 277 (1997) 1221–1225. https://doi.org/10.1126/science.277.5330.1221.

[15] M.A. Van Huis, J.H. Chen, Phase stability and structural relations of nanometer-sized , matrix-embedded precipitate phases in Al – Mg – Si alloys in the late stages of evolution, 54 (2006) 2945–2955. https://doi.org/10.1016/j.actamat.2006.02.034.

[16] M.A. Van Huis, J.H. Chen, H.W. Zandbergen, Phase stability and structural features of matrix-embedded hardening precipitates in Al – Mg – Si alloys in the early stages of evolution, 55 (2007) 2183–2199. https://doi.org/10.1016/j.actamat.2006.11.019.

[17] C. Ravi, C. Wolverton, First-principles study of crystal structure and stability of Al–Mg–Si–(Cu) precipitates, 52 (2004) 4213–4227. https://doi.org/10.1016/j.actamat.2004.05.037.

[18] D.J. Larson, D.T. Foord, A.K. Petford-Long, T.C. Anthony, I.M. Rozdilsky, A. Cerezo, G.W.D. Smith, Focused ion-beam milling for field-ion specimen preparation: Preliminary investigations, Ultramicroscopy. 75 (1998) 147–159. https://doi.org/10.1016/S0304-3991(98)00058-8.

[19] D.J. Larson, D.T. Foord, A.K. Petford-Long, A. Cerezo, G.D.W. Smith, Focused ion-beam specimen preparation for atom probe field-ion microscopy characterization of multilayer film structures, Nanotechnology. 10 (1999) 45–50. https://doi.org/10.1088/0957-4484/10/1/010.

[20] B. Gault, M.P. Moody, F. De Geuser, G. Tsafnat, A. La Fontaine, L.T. Stephenson, D. Haley, S.P. Ringer, Advances in the calibration of atom probe tomographic reconstruction, J. Appl. Phys. 105 (2009). https://doi.org/10.1063/1.3068197.

[21] B.P. Geiser, T.F. Kelly, D.J. Larson, J. Schneir, J.P. Roberts, M icroscopy M icroanalysis Spatial Distribution Maps for Atom Probe Tomography, (2007) 437–447.

[22] M. Song, E. Kobayashi, J. Kim, Clustering evolution during low temperature aging and thermal stability during two-step aging in Al-Mg-Si alloys, J. Alloys Compd. 946 (2023) 169291. https://doi.org/10.1016/j.jallcom.2023.169291.

[23] W.F. Miao, D.E. Laughlin, Precipitation hardening in aluminum alloy 6022, Scr. Mater. 40 (1999) 873–878. https://doi.org/10.1016/S1359-6462(99)00046-9.

[24] G.A. Edwards, K. Stiller, G.L. Dunlop, M.J. Couper, The precipitation sequence in Al–Mg–Si alloys, Acta Mater. 46 (1998) 3893–3904. https://doi.org/10.1016/S1359-6454(98)00059-7.

[25] J.D. Bryant, The Effects of Preaging Treatments on Aging Kinetics and Mechanical Properties in AA6111 Aluminum Autobody Sheet, 30 (1999).

[26] A. Gaber, A.M. Ali, K. Matsuda, T. Kawabata, T. Yamazaki, S. Ikeno, Study of the developed precipitates in Al-0.63Mg-0.37Si-0.5Cu (wt.%) alloy by using DSC and TEM techniques, J. Alloys Compd. 432 (2007) 149–155. https://doi.org/10.1016/j.jallcom.2006.06.004.

[27] M. Saga, Y. Sasaki, M. Kikuchi, Z. Yan, M. Matsuo, Effect of pre-aging temperature on the behavior in the early stage of aging at high temperature for Al-Mg-Si alloy, Mater. Sci. Forum. 217–222 (1996) 821–826. https://doi.org/10.4028/www.scientific.net/msf.217-222.821.

[28] T. Sato, High strength and high ductility aluminum alloys with controlled nano-clusters, J. Japan Inst. Light Met. 56 (2006) 592–601. https://doi.org/10.2464/jilm.56.592.

[29] J.H. Chen, E. Costan, M.A. van Huis, Q. Xu, H.W. Zandbergen, Atomic Pillar-Based Nanoprecipitates Strengthen AlMgSi Alloys, Science 312 (2006) 416–419. https://doi.org/10.1126/science.1124199.

**Tables**

Table 5.1 The user-defined parameters ($D_{max}$ and $N_{min}$) at a given order determined from Figs. 1-3.

| Condition | Order | $D_{max}$ | $N_{min}$ |
|---|---|---|---|
| R.T. | 1 | 0.63 | 8 |
| 40 ℃ | 1 | 0.70 | 10 |
| 70 ℃ | 1 | 0.67 | 10 |
| 100 ℃ | 2 | 0.87 | 15 |

Table 5.2 Summary of amount of heat evolution and absorption associated with the nanocluster and β″ phase from Fig. 4. To measure the area of β″ peak, the peaks of β″ and β′ were deconvoluted using Gaussian function. The peak area indicates the area between base line and DSC curve.

| Specimen | Peak area ($J \cdot g^{-1}$) | | |
|---|---|---|---|
| | Nanocluster formation | Nanocluster dissolution | β″ |
| A.Q. | 0.61 | 0.10 | 0.95 |
| R.T. | 0.43 | 0.13 | 0.95 |
| 40℃ | 0.26 | 0.14 | 0.81 |
| 70℃ | - | 0.02 | 0.69 |
| 100℃ | - | - | 0.30 |

Table 5.3 Statistical data of clusters formed at different temperatures. Number density is given by number of clusters over analyzed volume ($nm^{-3}$).

| Condition | Size | | Chemical composition | | Number density ($10^{23}$ $m^{-3}$) |
|---|---|---|---|---|---|
| | Number of solute atoms | Guinier radius (nm) | Mg/(Mg+Si) | Solutes/All (%) | |
| R.T. | 9 | 0.81 | 0.48 | 78.8 | 10.6 |
| 40 ℃ | 13 | 0.99 | 0.44 | 70.2 | 31.4 |
| 70 ℃ | 13 | 1.01 | 0.53 | 69.9 | 19.4 |
| 100 ℃ | 23 | 1.55 | 0.56 | 48.8 | 16.6 |

**Figures**

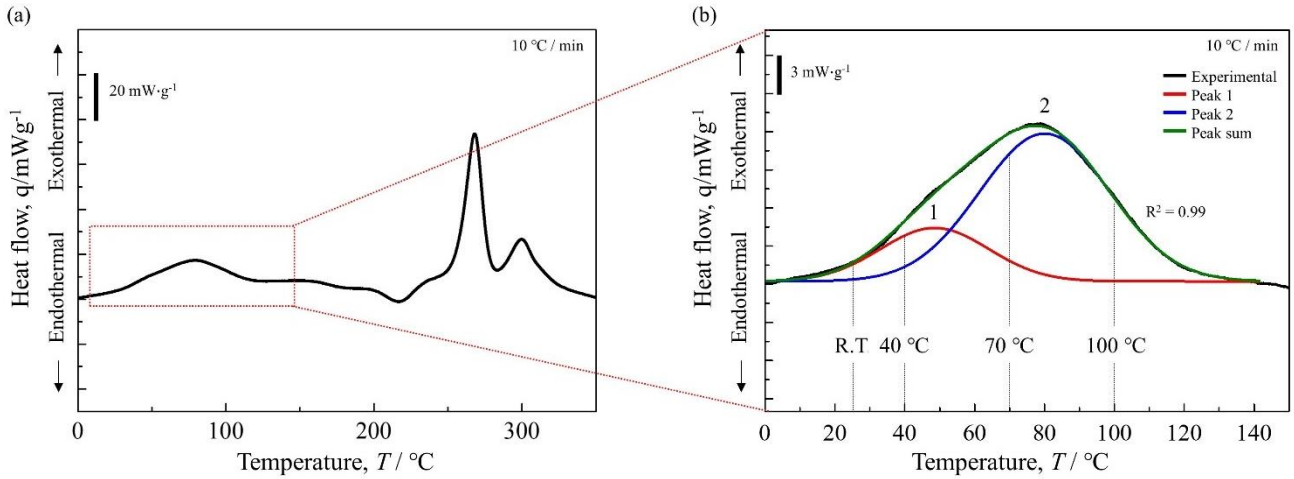


Figure 5.1 Gaussian function was used to separate the nanocluster formation peak in the DSC curve of the as-quenched Al-0.9% Mg-1.0% Si sample. The dotted lines indicate the temperatures where the final aging was performed in this study.

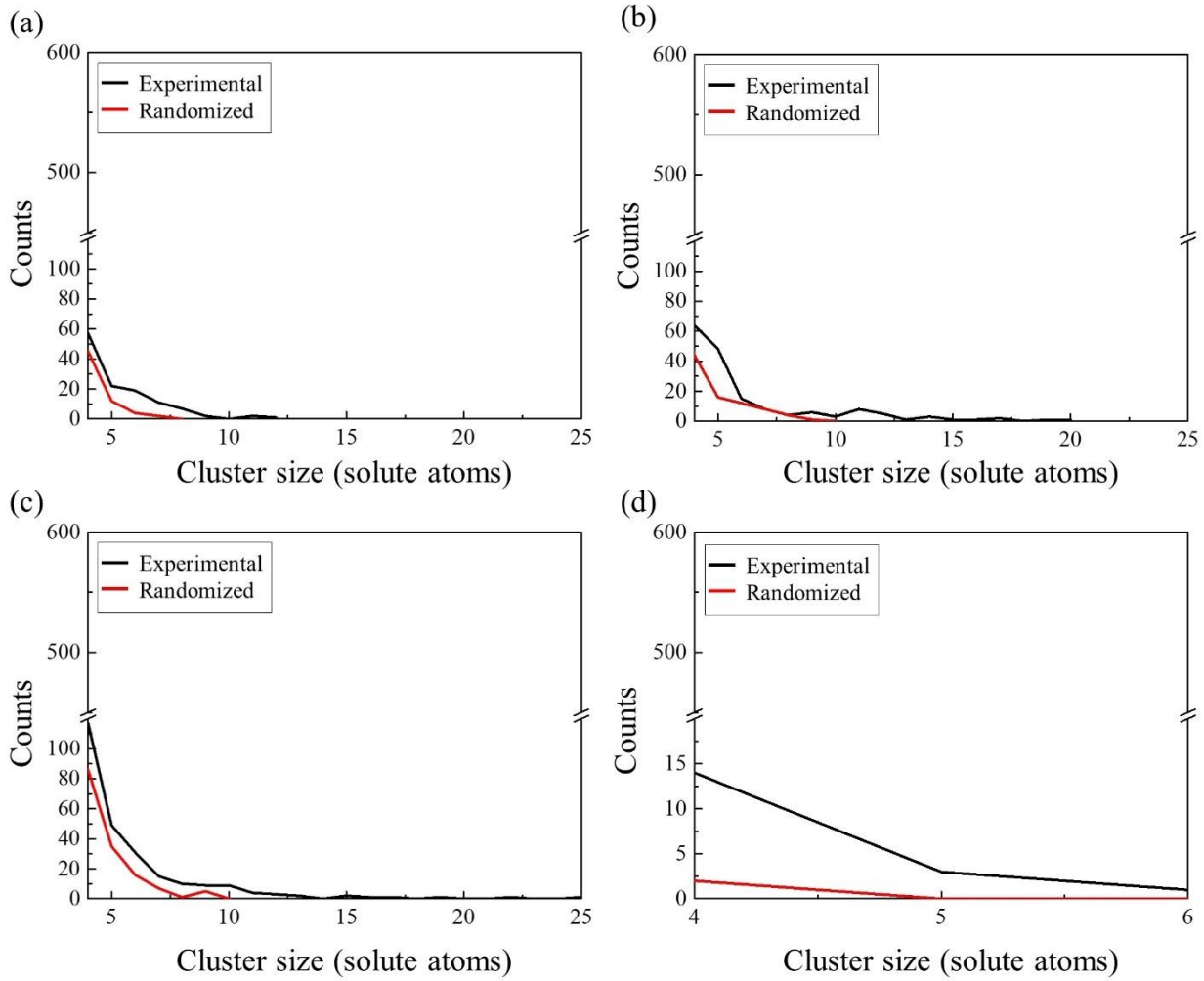


Figure 5.2 The size distribution of clusters for (a) R.T., (b) 40 ℃, (c) 70 ℃, and (d) 100 ℃ was determined using the $D_{max}$ values obtained from Fig. 1 based on the 1st-order. Black and red lines represent experimental and randomized datasets, respectively.

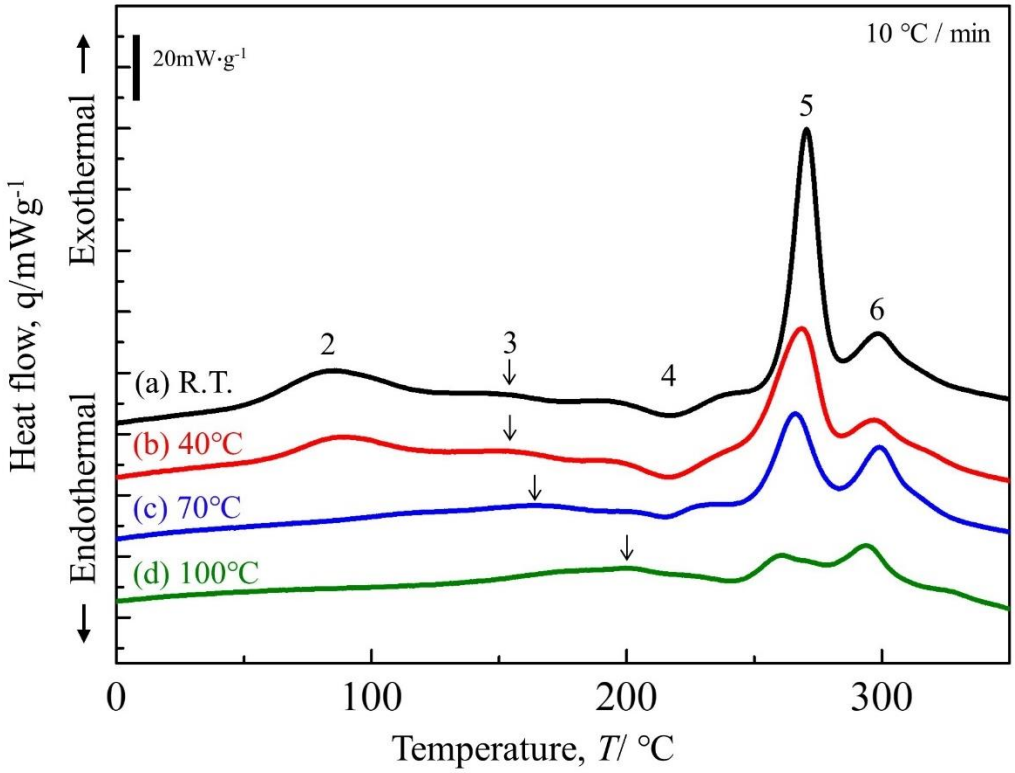


Figure 5.3 Change in DSC thermograms after different aging temperatures for 3.6 ks; (a) R.T., (b) 40 °C, (c) 70 °C and (d) 100 °C. Various stages of reactions occur, including the nanocluster formation (I) and nanocluster dissolution (III), as well as the formation of β″ (IV) and β′ (V) phases. The peak II is related to the GP zone/variants of β″ nuclei.

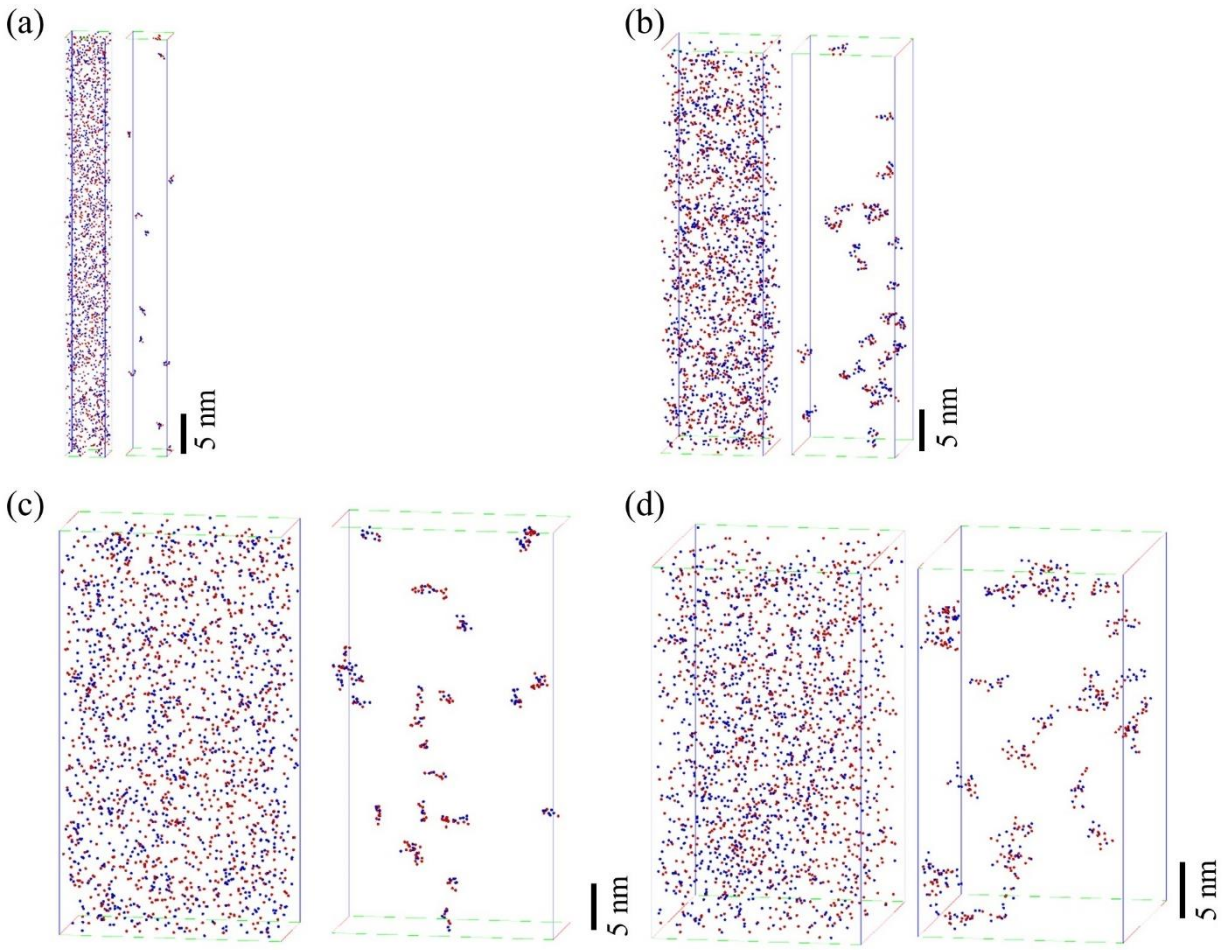


Figure 5.4 APT maps of (a) R.T., (b) 40 ℃, (c) 70 ℃ and (d) 100 ℃ before (left) and after (right) applying DBSCAN algorithm. Only solute atoms are shown. The red and blue dots represent the Mg and Si atoms, respectively. The size of dots does not reflect the actual atomic size.

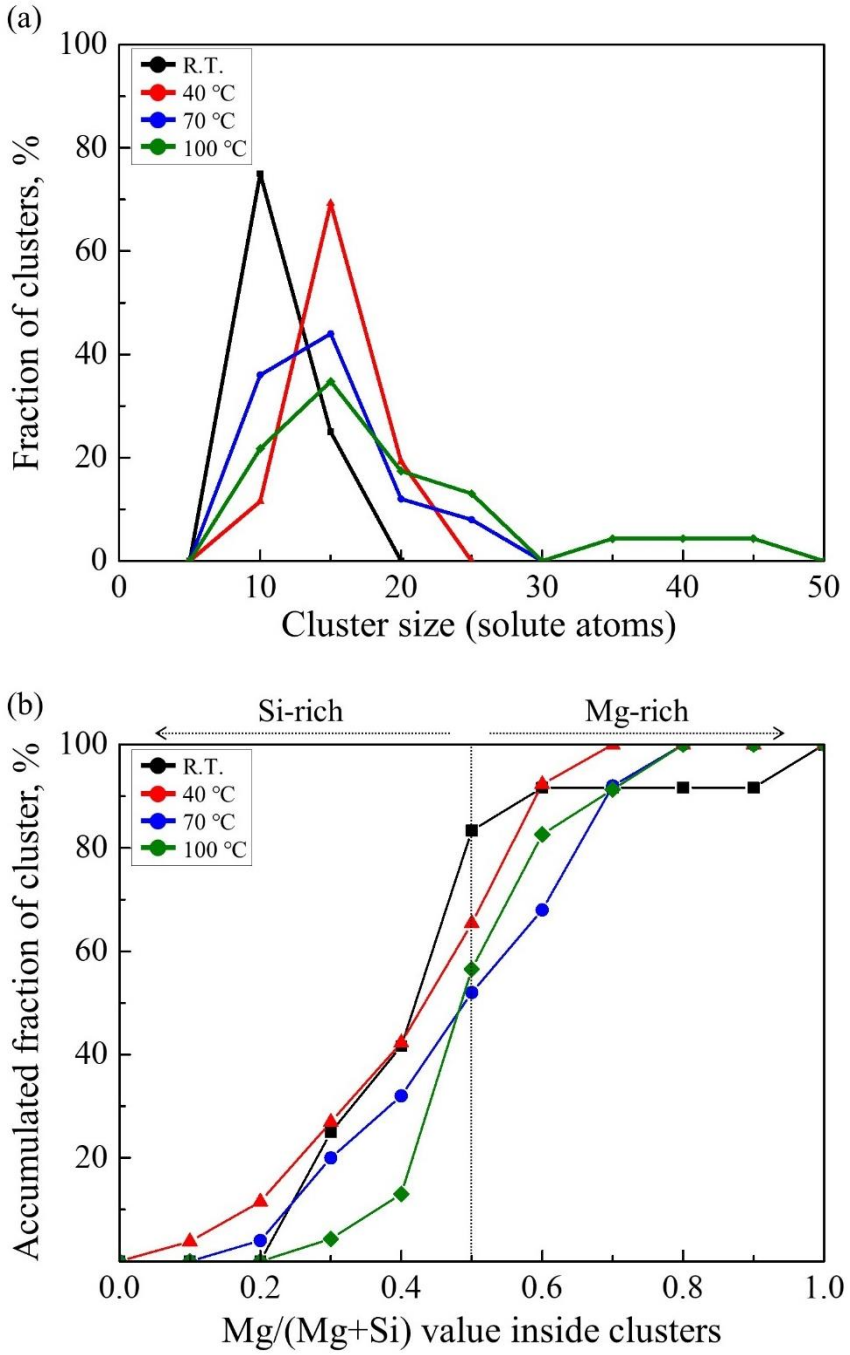


Figure 5.5 The characteristics of clusters [(a) fraction with size and (b) accumulated fraction with Mg/(Mg+Si)] formed at different temperatures.

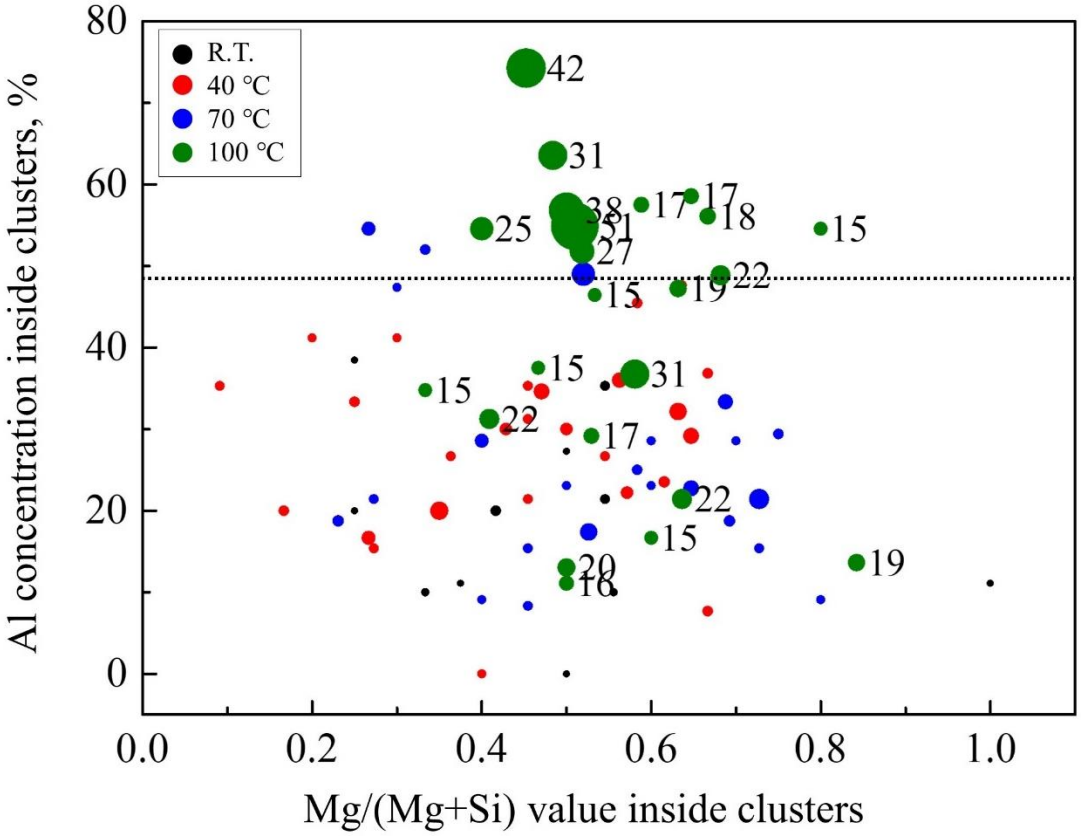


Figure 5.6 Al concentration with Mg/(Mg+Si) inside clusters. The size of a dot is proportional to number of solute atoms. The numbering next to the green dots indicates the number of solute atoms inside each cluster formed at 100 °C. The dotted line represents the 50 % Al fraction.

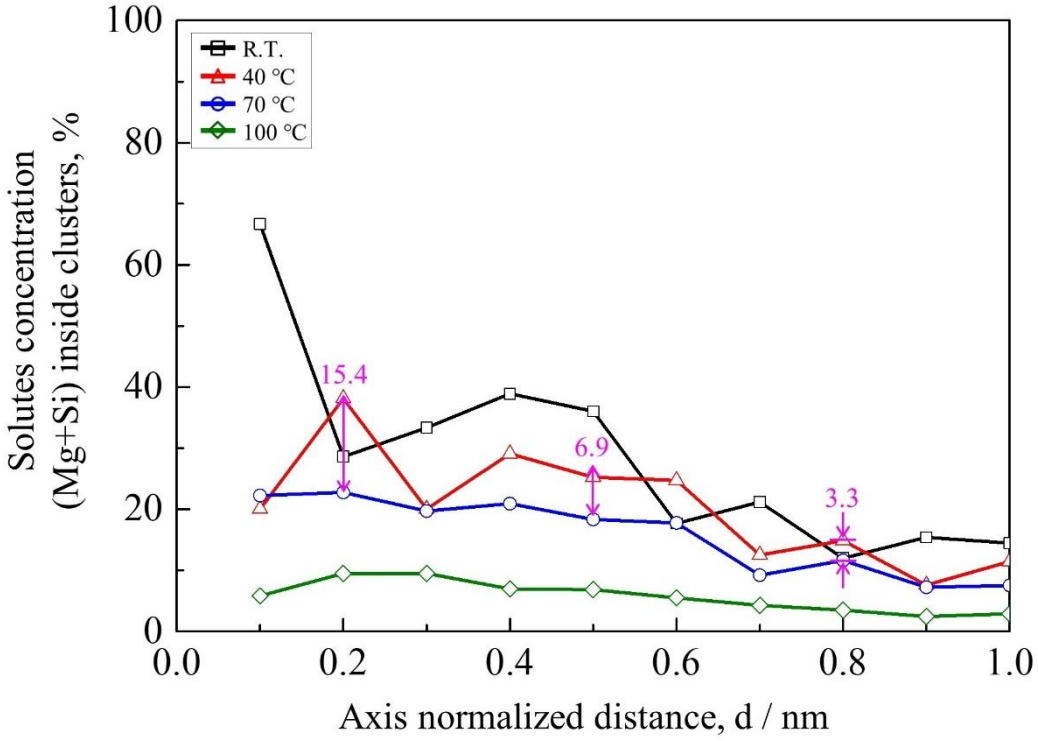


Figure 5.7 Concentration profile of clusters. The size of each cluster is normalized to *d*=1.0 nm based on maximum delta. Based on cluster-matrix interface (*d*=1.0), *d*=0 and *d*<1.0 represent the center and the inside of a cluster, respectively. The pink arrows and numbering indicate the differences between the samples at 40 and 70 ℃ samples.

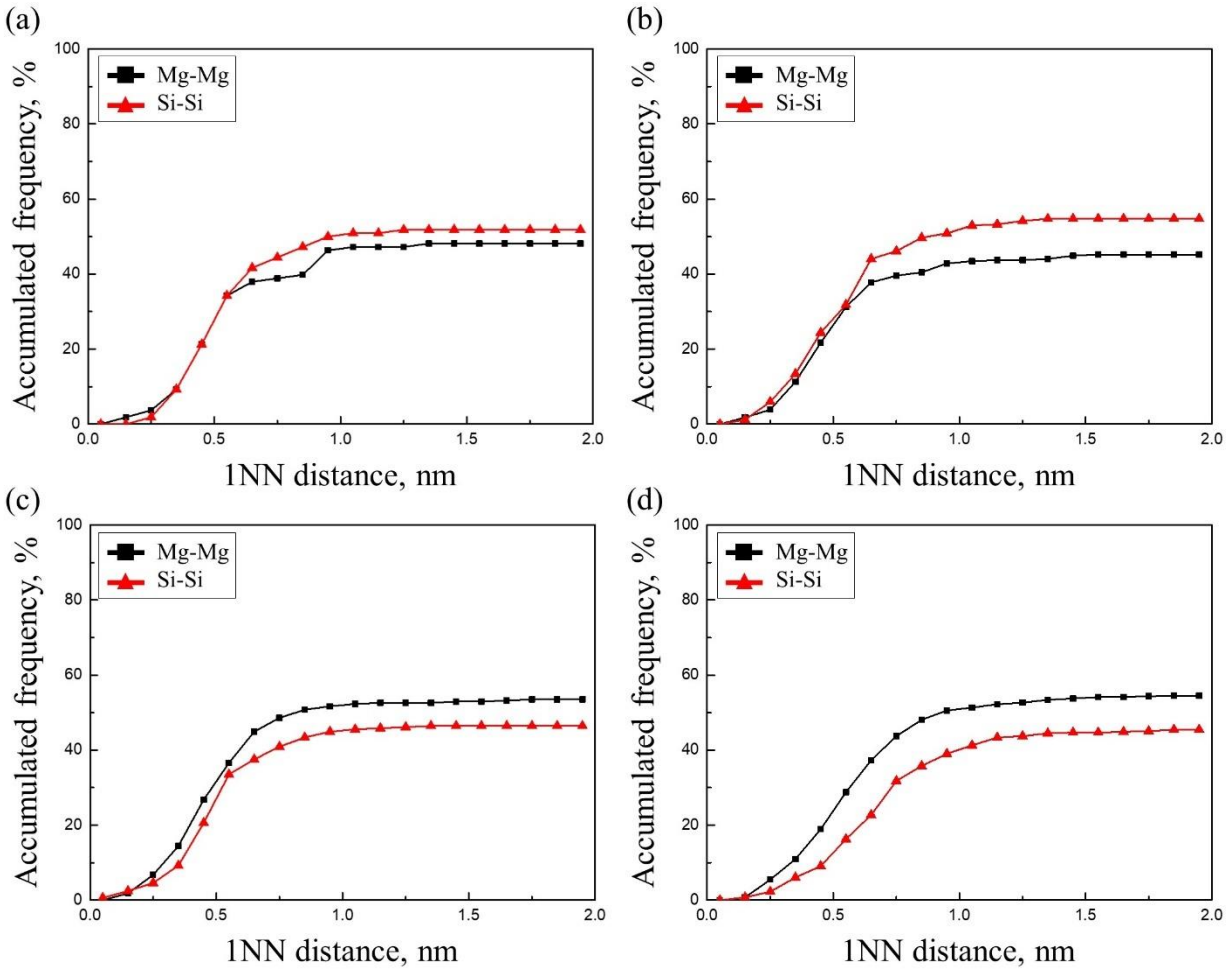


Figure 5.8 Accumulated frequency of first-nearest neighbor (1NN) distance of solute pairs [(a) R.T. (b) 40 ℃, (c) 70 ℃ and (d) 100 ℃]. Only the solute atoms involved in clusters were considered.

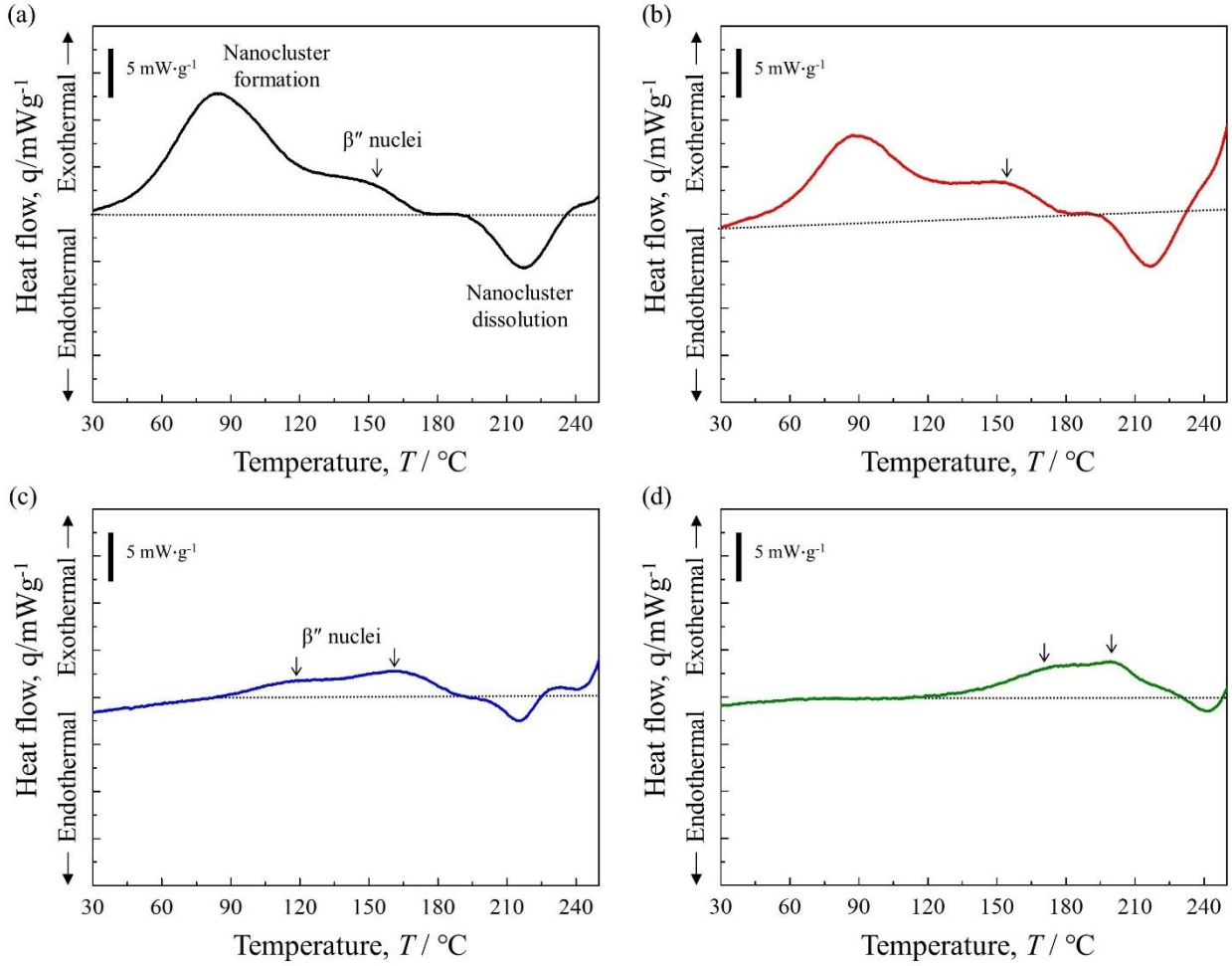


Figure 5.9 Enlarged heat flow curves of peak I to III for all samples [(a) R.T. (b) 40 °C, (c) 70 °C and (d) 100 °C] in Fig. 5. The arrow marks indicate the exothermic peaks associated with the β″ nuclei.

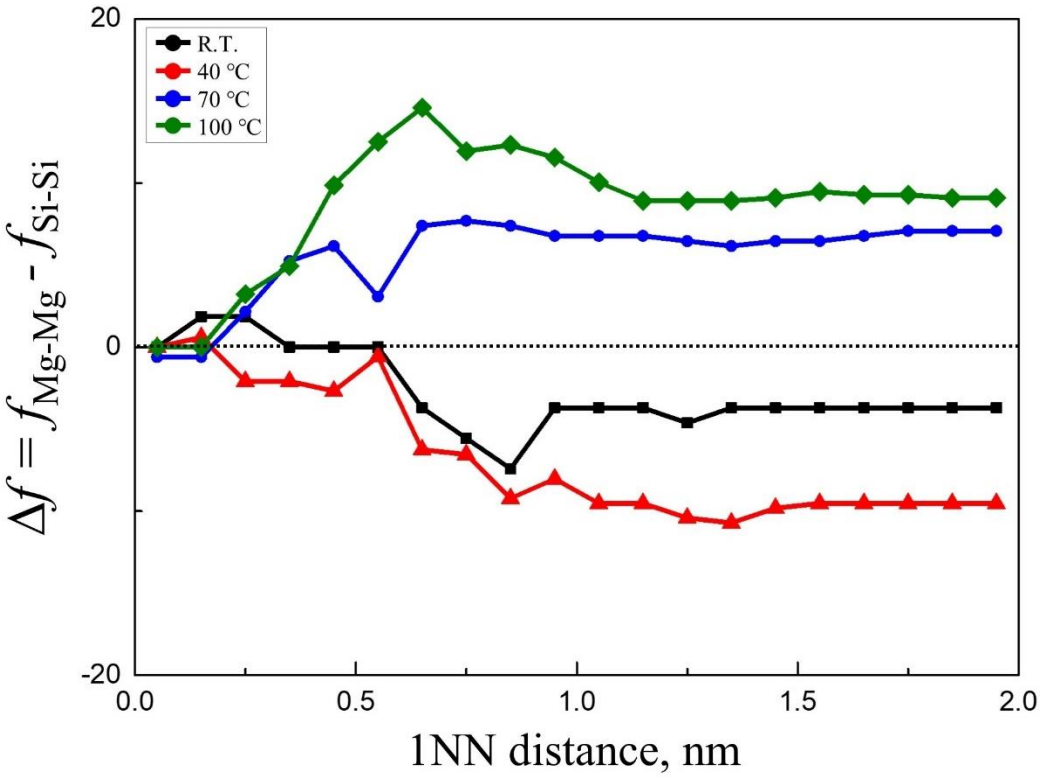


Figure 5.10 Delta frequency ($\Delta f$) of first-nearest neighbor (1NN) distance of solute pairs obtained from Fig. 8. $\Delta f$ is difference in frequency between Mg-Mg and Si-Si pairs. The dotted line indicates same frequency ($\Delta f = 0$) of two-types of solute pairs. Negative and positive values of $\Delta f$ indicate the high frequency of Si-Si and Mg-Mg pairs, respectively.

# Chapter 6

# Microstructural evolution at the initial stage of two-step aging in an Al-Mg-Si alloy

## 6.1 Introduction

The Al body panels is made by two-step aging process as mentioned in Section 1.3.2. Considerable research on the two-step aging process has been conducted. In Al-Mg-Si alloys, exposure to room temperature prior to artificial aging i.e., bake hardening causing a '*Negative effect of two-step aging*' phenomenon occurs in which the mechanical properties of the precipitate are degraded due to coarsening of the β″ [1,2]. This phenomenon is known to occur because the nanoclusters formed at room temperature do not transfer to the strengthening β″ phase at the elevated two-step aging [3–5]. Meanwhile, the role of clusters formed during natural aging in the formation of the precipitate at the initial stage of two-step aging has become interesting to researchers. Dissolution of nanoclusters formed during natural aging in Al-Mg-Si alloys has been reported based on hardness, electrical resistivity and thermal analysis [3,6–9]. Some researchers have introduced the hardness decrease phenomenon at the initial stage of two-step aging due to the dissolution of nanoclusters [7,10–17]. Atomic rearrangements of nanoclusters at the early stage of two-step aging were also introduced [17], and nucleation and growth of precipitation-reinforced phases were confirmed [18]. It seems that the internal structure of nanoclusters changes and the nucleation of precipitation strengthening phases occurs simultaneously. In order to analyze this phenomenon, it is important to directly observe the internal structure of the cluster. Transmission electron microscope (TEM) is mainly used to

observe the fine precipitates in Al-Mg-Si alloys. Structural analysis of precipitates using high resolution-TEM (HR-TEM) has also been carried out [19–21]. Nanoclusters are fully coherent with the Al matrix [22], and Al-Mg-Si alloys consist of consecutive atomic number elements (i.e., atomic sizes are similar) with the atomic numbers 12, 13, and 14 for Mg, Al, and Si, respectively, making it difficult to distinguish the chemical composition by TEM. Murayama et al. [22] found that no contrast by clusters was observed using HRTEM for a specimen naturally aged for 70 days in Al-Mg-Si alloys. For this reason, microstructural evolution at the initial stage of two-step aging requires analysis using a three dimensional atom probe (APT) to investigate the atomic distribution. Resolution of APT in the lateral (x and y axis) and depth directions is about 0.04 and 0.20 nm [23–27], respectively, which facilitates nanocluster analysis. Clustering behavior using APT in Al-Mg-Si alloys has been conducted in Al-Mg-Si alloys [28–32]. So far, simultaneous consideration of the nucleation of precipitation-reinforced phases and the dissolution of nanoclusters at an atomic scale has rarely been reported, and the internal structure changes under the initial stage of the two-step aging in Al-Mg-Si alloys are still unclear. The aim of this study was to investigate the microstructural evolution based on APT analyses such as cluster formation, dissolution of nanoclusters and nucleation of precipitates at an atomic scale.

## 6.2 Experimental procedure

Al-0.9Mg-1.0Si (mass %) alloys provided by UACJ Corp. (Japan) were used. The chemical composition quoted in this paper is mass% unless otherwise stated. In this study, the specimens were solution treated using a salt bath made of mixed powder using $KNO_3$ and NaOH in a 1:1 ratio at 560 °C for 1.8 ks and then quenched in ice water at 0 °C for 0.06 ks. Natural aging was performed at room temperature around 25 °C for 2419.2 ks. Artificial aging was carried out

using an oil bath containing Silicone Oil (Shin-Etsu, KF-96 1000CS) at 170 °C up to 604.8 ks. In order to investigate the microstructural evolution, namely, nanocluster dissolution and precipitate formation at the initial stage of two-step aging, two-step aging was conducted at 170 °C after natural aging for 2419.2 ks. Figure 6.1 shows the heat treatment history of the two-step aging process used in this study. Natural aging for 2419.2 ks and artificial aging for 0.6 and 1.2 ks after natural aging are referred to as NA (2419.2 ks), Two (0.6 ks) and Two (1.2 ks), respectively.

The hardness measurements were conducted using a micro Vickers hardness test (HV-113, Mitsutoyo Corp.) under a load of 200 g and a dwell time of 10 s. The average hardness results were calculated from five measurements excluding the maximum and minimum values in seven measurements. All specimens used for hardness measurements were fabricated with a size of 10 x 10 x 1 mm (height). Thermal analyses were performed using a differential scanning calorimetry (DSC 204 F1 phoenix, NETZSCH) in a nitrogen gas atmosphere at a heating rate of 10 °C/min. DSC running started from -50 °C using liquid nitrogen to obtain the stabilized data at a low temperature. Specimens for DSC analysis were made by fabricating a plate of 1 mm thickness. All specimens were prepared with a weight of 40 ±0.05 mg and a disc height of 1 mm. The specimens for APT were prepared using a focused ion beam (Helios NanoLab 600, FEI). The cryo-focused ion beam (cryo-FIB) milling with liquid nitrogen was utilized to prevent room temperature exposure of the specimen and a temperature increase during operation of the FIB. The clustering analysis was conducted using a three dimensional atom probe (LEAP 4000X HR™, CAMECA instruments Inc.) in the voltage pulsed mode with a voltage pulse fraction of 20% and an operation temperature of about -223 °C in a vacuum of up to 6.5 x $10^{-11}$. Data reconstruction and visualization were carried out using IVAS 3.8.0 software. The lateral resolution of APT is mainly controlled by the aberrations of the ion

trajectories. The low index pole is known as a region of non-uniform atom distribution that causes ion trajectory aberrations [33,34]. Therefore, low index poles with regions of non-uniform atom distribution were excluded. The maximum separation method [35] was applied for the cluster analysis. The maximum separation distance between atoms ($D_{max}$) and the minimum number of atoms ($N_{min}$) were chosen as 0.75 nm and 10 solute atoms, respectively.

## 6.3 Results

### 6.3.1 Thermal analysis

Figure 6.2 shows the DSC results of the as-quenching and NA (2419.2 ks). In order to clarify the the nanocluster formation peak, a temperature range from 0 to 200 °C was selected. The formation temperatures of the nanoclusters were 79.4 and 117.0 °C in the as-quenched and NA (2419.2 ks), respectively. In addition, the nanocluster peak areas of as-quenched and NA (2419.2 ks) were 0.75 and 0.37 J/g, respectively. The formation of the nanocluster during natural aging caused a decrease in the amount of solute atoms (Mg and Si) and the number of vacancies, in which case the nanocluster peak temperature shifted to the higher temperature.

### 6.3.2 Hardness measurement

Figure 6.3 shows the hardness results during two-step aging at 170 °C after natural aging for 2419.2 ks. The hardness increased to 93.1 HV due to the formation of the nanocluster after natural aging for 2419.2 ks. Hardness decreased by about 7.7 HV at Two (0.6 ks) and then increased after Two (0.6 ks) during the two-step aging. That is, the nanocluster dissolution (red line) and the formation of precipitates (blue line) occurred simultaneously at the initial stage of two-step aging. At the initial stage of two-step aging, the hardness increases and decreases were

dominant due to the formation of precipitates and dissolution of nanoclusters, respectively. Therefore, the dissolution of nanoclusters up to Two (0.6 ks) and the formation of nuclei of precipitates after Two (0.6 ks) is expected to occur predominantly.

### 6.3.3 APT analysis

We investigated the microstructure evolution at the initial stage of two-step aging for the nanocluster dissolution and precipitate formation on the basis of the APT results. Figure 6.4 shows a APT map that visualizes the atomic distribution. The maps on the left side show the solute atoms Mg and Si at the region of interest. The solute atoms after cluster analysis, in which the maximum separation method was applied, are displayed on the right side. Mg and Si atoms are shown as red and blue spheres, respectively. The size of the sphere did not directly match the size of the atoms. The lengths of the x, y and z axes of the analyzed region were 10×8×25 nm, respectively.

Table 6.1 shows the statistical data for each variable of the analyzed clusters, and the average value is described. Information on the average cluster number density, the Mg:Si ratio, the size and the atomic number density for each heat treatment condition was obtained. The cluster size was calculated based on the radius of gyration, but it provided a slightly smaller parameter than the actual cluster size. Therefore, it is common to convert to the Guinier radius ($r_G$), which reflects the actual size well [36]. The volume fraction and atomic density stand for the percentage of volume of clusters per unit volume of 1 $nm^3$ and the number of atoms inside the cluster per unit volume of 1 $nm^3$. The number density represents the number of clusters per unit volume of 1 $m^3$. 59, 59 and 52 clusters were obtained by the maximum separation method from 5, 6 and 10 million total atoms detected at NA (2419.2 ks), Two (0.6 ks) and Two (1.2 ks), respectively.

Figure 6.5 shows a comparison of the cluster size distributions for each heat treatment condition. The black, red and blue lines are the results for NA (2419.2 ks), Two (0.6 ks) and Two (1.2 ks), respectively. The number fraction of clusters represents the percentage of the number of clusters corresponding to each $r_G$ divided by the total number of clusters. In NA (2419.2 ks), Two (0.6 ks), and Two (1.2 ks), the clusters with a range of 0.44-2.45, 0.45-1.45, and 0.52-3.81 nm are distributed, respectively. Clusters larger than 1.50 nm were found in NA (2419.2 ks) and Two (1.2 ks), but no cluster larger than 1.50 nm in Two (0.6 ks) was clarified. Overall, the size of clusters decreased until Two (0.6 ks) and then increased. Therefore, we considered that nanocluster dissolution and precipitate nucleation during Two (0.6 ks) and Two (1.2 ks) are dominant, respectively.

Figure 6.6 shows the accumulated number fraction with the Mg:Si ratio of the cluster. Black, red and blue lines represent the results of NA (2419.2 ks), Two (0.6 ks) and Two (1.2 ks), respectively. For ease of checking the Mg and Si ratio inside clusters, we used Mg/(Mg+Si) values in this study. We classified clusters with Mg/(Mg + Si) values of less than 0.4, 0.4 to 0.6 and greater than 0.6 as Si-rich, balanced and Mg-rich, respectively. The distribution of Si-rich, Balanced and Mg-rich clusters at each heat treatment condition is quantitatively summarized in Table 6.2. Si-rich, Balanced and Mg-rich clusters of 37, 42 and 21% in Two (0.6ks) were identified, respectively. More than 90% of the total Si-rich and Balanced clusters were identified in NA (2419.2 ks) and Two (1.2 ks). Si-rich clusters accounted for 44% at NA (2419.2 ks) and 17% at Two (1.2 ks).

Figure 6.7 shows the value of Mg/(Mg+Si) with the size of the cluster. The black squares, red triangles and blue circles represent NA (2419.2 ks), Two (0.6 ks) and Two (1.2 ks), respectively. The green dotted line shows the chemical composition of the specimen (Mg/(Mg+Si) = 0.47). Clusters smaller than 1.5 nm in NA (2419.2 ks) and Two (1.2 ks)

exhibited various Mg:Si ratios. Chemical composition of the clusters became close to a constant value with an increasing cluster size. We confirmed that there was also a large cluster of 3.8 nm in Two (1.2 ks). Most of the clusters had a $r_G$ ranging from 0.5 to 1.0 nm and a wide range of Mg: Si ratios in Two (0.6ks).

Figure 6.8 shows the relationship between hardness, cluster volume fraction, and number density. Black and red represent the volume fraction and number density as a function of hardness changes, respectively. The hardness and number density increased in the order of Two (0.6 ks) < Two (1.2 ks) < NA (2419.2 ks), but the volume fraction increased in the order of Two (0.6 ks) < NA (2419.2 ks) < Two (1.2 ks). Details on the relationship between hardness change and cluster distribution are discussed in the next section.

## 6.4 Discussion

### 6.4.1 Mechanism of nanocluster dissolution and nucleation of β″

A detrimental effect on mechanical properties was reported when the natural aging was performed before artificial aging [1,2,37,38]. Pashley et al. [2] reported that coarsening of precipitates is accelerated during the two-step aging after natural aging, resulting in a negative effect of two-stage aging. Yamada et al. [39] confirmed that this negative effect of two-stage aging was due to the nanocluster formation during natural aging. Nanocluster formation during natural aging has been reported through various analysis methods. The exothermic peaks are generated near 0-150 °C during the DSC analysis [40–44]. Edwards et al. [45] revealed that the exothermic peak was due to the formation of nanoclusters composed of Mg and Si atoms by analysis using atom probe field ion microscopy (APFIM). The endothermic peak analyzed by DSC in Al-Mg-Si alloys was identified before the β" formation peak [41,46–48]. Bandini et al.

[46] and Edwards et al. [45] reported this endothermic peak as dissolution of the GP zone and Mg cluster, respectively. Serizawa et al. [3] confirmed that the nanoclusters formed after natural aging for 3.6 ks were not dissolved under 180 ℃ based on electrical resistivity and APT analyses. Meanwhile, the partial dissolution of nanoclusters formed during the natural aging was identified during two-step aging at 170 ° C [49]. It is known that Si-rich clusters are formed at the initial stage of natural aging, and then Mg is incorporated with an increasing natural aging time [41]. Aruga et al. [14] found that the Si-rich clusters were thermally stable, whereas the Mg-Si co-clusters were dissolved during aging at 170 ° C based on the APT analysis.

Whelan proposed the kinetics of precipitate dissolution based on theoretical calculations as follows:

$$\frac{dr}{dt} = -\frac{kD}{2r} - \frac{k}{2}\sqrt{\frac{D}{\pi t}} \tag{6.1}$$

$$k = 2(\rho_I - \rho_M)/(\rho_P - \rho_I) \tag{6.2}$$

where $r$, $D$, $k$, $\rho_I$, $\rho_M$ and $\rho_P$ are the radius at the dissolution time ($t$), diffusion coefficient, concentration gradient of the solute atom, solute atom concentration at the precipitate-matrix interface, solute atom concentration at the matrix and solute atom concentration at the precipitate, respectively. The kinetics of the precipitate dissolution proposed by Whelan [50] is based on the assumption that the solute atom concentration at the precipitate-matrix interface is always in equilibrium. The precipitate dissolution occurs with the interface movement to reduce the concentration gradient between the precipitate and the matrix. Madanat et al. [51] studied the reversion at 250 ℃ of clusters formed during natural aging for 2 weeks in an Al-Mg-Si alloy through theoretical calculation, experimental data and modeling. They calculated the vacancy concentration during reversion. The results confirmed that the vacancy concentration during the reversion aging for 30 s was increased. They explained that the

vacancy which had been sinking into the grain boundaries or the dislocation jog was regenerated in order to adjust the equilibrium vacancy concentration. The regenerated vacancy was transferred to the cluster, and then dissolution occurred. Pogatscher et al. [52] reported that the amount of dissolved Cluster (1) increased with an increasing two-step aging temperature based on the hardness results. They explained that the dissolution of the cluster formed during natural aging was controlled by the mobile vacancy concentration during the two-step aging. They characterized the clusters using the iso-concentration surface method, but it was difficult to investigate the dissolution mechanism of Cluster (1) because the cluster size and morphology were affected by selecting the concentration level of the iso-concentration surface [36]. The internal structure of the cluster, namely, the chemical composition and atomic density, cannot be analyzed by the iso-concentration surface method. On the other hand, the maximum separation method provides the chemical composition and atomic density of the cluster. We confirmed that the cluster size ($r_G$), volume fraction ($V_f$) and number density ($\rho$) decreased during Two (0.6 ks) (see Table 6.1). Nanoclusters were analyzed by the maximum separation method. There are two cases for the nanocluster dissolution. One is that the cluster is no longer recognized because the minimum number of solute atoms ($N_{min}$) in the $D_{max}$ is not satisfied. Another is that size reduction occurs because $D_{max}$ and $N_{min}$ are satisfied. These phenomena occur during the nanocluster dissolution. The schematic diagram is described as shown in Fig. 6.9.

The nanocluster dissolution and the precipitate formation should be considered at the same time at the initial stage of the two-step aging as mentioned in the introduction. It is difficult to identify nanoclusters of similar size from newly formed nuclei by the average value of the entire cluster. Analysis with the cluster size is necessary. Statistical data for the approximately upper and lower 10% of the $r_G$, $r_G^{max}$ and $r_G^{min}$, are summarized in Table 6.3. In $r_G^{max}$,

clusters larger than 1.5 nm formed after NA (2419.2 ks) were dissolved during Two (0.6 ks) so that no cluster larger than 1.5 nm ($r_G$) for Two (0.6 ks) was identified. Moreover, the number density of clusters for Two (0.6 ks) was lower than that of NA (2419.2 ks). It was apparent that some clusters with a size less than 1.5 nm formed after NA (2419.2 ks) were also dissolved, because the clusters after dissolution did not satisfy the value of $D_{max}$ or $N_{min}$. Meanwhile, the hardness increased after Two (0.6 ks) (see Fig. 6.3), and the values of $r_G$, $V_f$, and $\rho$ also increased (see Table 6.1). This hardness increase was mainly caused by the formation of the nucleus of β″. In this work, as reported by Kim et al. [17], Pre-β″ was defined as the nucleus of β″. We concluded that the dissolution of nanoclusters up to Two (0.6 ks) and the formation of pre-β″ dominated after Two (0.6 ks).

### 6.4.2 Internal structure evolution of each cluster

Chemical composition affects the formation and dissolution of nanoclusters in Al-Mg-Si-based alloys. The formation of nanoclusters is known to depend more on the Mg:Si ratio than on the amount of Mg+Si [8]. When Mg/(Mg+Si) is 0.5, the formation of nanoclusters is most promoted during natural aging, and the initial hardness decrease in two-step aging due to the partial dissolution of nanoclusters is affected by the chemical composition of the alloy [16]. At the same time, it is important to investigate the compositional change of nanoclusters. Therefore, we elaborated on the compositional change of nanoclusters at the initial stage of two-step aging. Table 6.4 shows the chemical composition analysis results for nanoclusters after natural aging in the literature based on a APT-based analysis. Murayama et al. [22] quantitatively reported on solute clusters formed during natural aging of alloys with Mg/(Mg+Si) values of 0.44 and 0.65 and confirmed that the solute clusters had Mg:Si ratios similar to the alloy composition [22]. Aruga et al. [14] confirmed the chemical composition

distribution of nanoclusters formed during short (108 ks) and long ($7.20\times10^3$ ks) natural aging times for alloys with Mg/(Mg+Si) = 0.40 and 0.53. It seems that the clustering behavior is influenced by alloy composition in a short natural aging time, but not much in a long natural aging time. Serizawa et al. [40] analyzed the clustering behavior at the multi-step aging with the natural aging and pre-aging time of alloys with a Mg/(Mg+Si) value of 0.49. They confirmed a wide range of Mg:Si ratios for nanoclusters after natural aging [40]: The smaller the cluster, the wider the Mg:Si ratio. Torsæter et al. quantitatively analyzed the chemical composition of clusters after natural aging for 604.8 ks with different chemical compositions, namely, Si-rich (Mg/(Mg+Si) value = 0.30) and Mg-rich (Mg/(Mg+Si) value = 0.61) alloys [53]. It can be seen that the Mg/Si ratio of the cluster generated during natural aging was largely similar to the composition of the alloy [53]. After NA (2419.2 ks), mainly Si-rich and balanced clusters formed (see Fig. 6.6). The Mg/(Mg+Si) value was similar to the composition of the alloy ( $r_G^{max}$ in Table 6.3). The chemical composition of nanoclusters approaches the composition of the alloy with an increasing cluster size (see Fig. 6.7). Meanwhile, it is known that Mg/(Mg+Si) ≅ 0.45 based on the high resolution TEM for β″ [4,18,54–56]. Thus, the pre-β″ formed during Two (1.2 ks) is similar to the Mg:Si ratio of β″.

The β″ transition from the nanocluster is determined not only by the chemical composition but also by the atomic arrangement inside a cluster [8]. Kim et al. [17] proposed that the thermal stability of a nanocluster is influenced not only by the size of the nanocluster but also by the atomic arrangement (i.e., the internal structure). The literature of APT-based studies mainly analyzed the size, number density, and chemical composition of nanoclusters [57–62], but it was difficult to understand how solute atoms inside nanoclusters were compactly composed. Therefore, we analyzed the atomic number density change of a cluster at the initial stage of two-step aging.

In the analysis of APT data, the Guinier radius ($r_G$), which reflects the actual size of the cluster, is obtained by converting the radius of gyration ($l_g$). Considering only the x-axis, $l_x$ is obtained by the following equation [36].

$$l_x = \sqrt{\frac{\sum_{i=1}^{n} m_i (x_i - \overline{x})^2}{m_i}} \tag{6.3}$$

where $x_i$, $m_i$, n and $\overline{x}$ are the spatial coordinates of the i$^{th}$ atom, the mass of the i$^{th}$ atom, the number of atoms and the center of mass, respectively. The center of mass ($\overline{x}$) is as follows [36].

$$\overline{x} = \frac{\sum_{i=1}^{n} x_i m_i}{\sum_{i=1}^{n} m_i} \tag{6.4}$$

Assuming clusters of different atomic densities with the same number of atoms on the uniaxial (i.e., X-axis) line, we can see that $l_x$ decreases as the constituent atoms of the cluster become more compact, based on $l_x$and $\overline{x}$ equations. Moreover, intuitively, we expected a higher atomic number density inside the cluster for a smaller cluster. The atomic number density (Al+Mg+Si) of nanoclusters with a radius over than 2 nm at NA (2419.2 ks) and Two (1.2 ks) was 22 and 49 atoms·nm$^{-3}$, respectively (see Table 6.3). It can be seen that the atomic number density (Al+Mg+Si) at Two (1.2 ks) is two times higher than other heat treatment conditions. Figure 6.10 shows the relationship of the atomic number density (Al+Mg+Si), $r_G$, and Mg/(Mg+Si) values for the 5 largest clusters with different heat treatments. Black, red and blue spheres represent NA (2419.2 ks), Two (0.6 ks) and Two (1.2 ks), respectively. The sphere size and number in Fig. 6.10(b) stands for the size of nanoclusters. The atomic density (Al+Mg+Si) at Two (1.2 ks) is higher than 30 nm$^{-3}$, while NA (2419.2 ks) and Two (0.6 ks) are lower than 30 nm$^{-3}$. The nucleus of the precipitate and nanocluster can be distinguished by considering the atomic density of the nanoclusters. We propose for the first time that the nanocluster in Al-Mg-Si alloys acts as a nucleus of the precipitate, pre-β ", when the size and atomic density are larger than 2 nm and 30 nm$^{-3}$, respectively.

### 6.4.3 Effects of number density and volume fraction on hardness change

The age-hardenable Al alloys are generally strengthened by a different mechanism depending on the radius of the particle on the basis of the critical cut-off radius ($r_c$). If particles smaller than $r_c$ are formed, they are strengthened by the cutting mechanism. In this cutting mechanism, the critical resolved shear stress ($\tau$) can be expressed by the following equation [63].

$$\tau = cf^m r^p \tag{6.5}$$

where $c$ is an alloy constant that depends on the particular strengthening mechanisms (coherency, chemical, stacking fault, and/or modulus hardening). $f$ and $r$ represent the volume fraction and particle radius, respectively. The exponents m and p are always positive and increase in strength as the volume fraction increases. If the particle grows to be larger than $r_c$, the dislocation passes through the particle, forming a loop or bypassing it. This mechanism is called Orowan hardening, and the critical resolved shear stress is expressed as [64]:

$$\tau_c = \frac{0.84\mu b}{2\pi(1-\nu)^{1/2}} \frac{ln(\Lambda/r_0)}{L_s - 2\langle r_s \rangle} \tag{6.6}$$

where $\mu$, $\Lambda$ and $r_0$, $b$, $L_s$ and $r_s$ stand for the shear modulus, outer and inner cut-off distances, Burger's vector, obstacle spacing and average planar particle radius, respectively. $L_s$ is expressed as [65]:

$$L_s = \left(\frac{2\pi}{3f}\right)^{1/2} r \tag{6.7}$$

where $r$ is the average radius of the particle. As the volume fraction ($f$) increases, the obstacle distance ($L_s$) decreases, which increases $\tau_c$. It can be seen that both cutting and Orowan mechanisms are proportional to the volume fraction. Marceau et al. [60] analyzed the strengthening mechanism during artificial and natural aging in AA6111 based on modeling and

experimental data and found that critical cut-off size ($r_c$) = 2.1 nm. From the $r_G^{max}$ result (see Table 6.3) at Two (1.2 ks), it can be seen that clusters with a radius of 2.1 nm or larger are formed. It is necessary to consider both cutting and Orowan mechanisms in the strengthening in the two-step aging in an Al-Mg-Si alloy. Meanwhile, Starink et al. [66] performed thermodynamic modeling to investigate the cluster strengthening in Al-Mg-Si alloys. As a result of the modeling, they found that strengthening due to nanocluster formation during natural aging is dependent on the short range order (SRO) mechanism and is proportional to the number of clusters (i.e., number density). Marceau et al. [60] analyzed cluster strengthening based on areal glide plane modeling and APT. They found that strengthening during artificial aging is dependent on the number density of small clusters of less than 1 nm, and clusters larger than 1 nm contribute very little to the increase in strength since few clusters are formed [60]. Therefore, it is important to analyze the relationship among the hardness change, the volume fraction of the cluster and the number density at the initial stage of two-step aging.

Figure 6.8 shows the relationship between the hardness change, the volume fraction of clusters and the number density of nanoclusters at the initial stage of two-step aging. The lowest hardness at Two (0.6 ks) was due to the low volume fraction and number density due to the nanocluster dissolution. At Two (1.2 ks), the average size and volume fraction of the cluster were found to be higher than NA (2419.2 ks), with low number density and hardness. Therefore, we deduced that an increase in the volume fraction of a nanocluster because of an increase in the number density of the cluster contributed more to strengthening than a size increase at the initial stage of two-step aging.

## 6.5 Conclusions

We performed a statistical analysis using APT to investigate the microstructural evolution at the initial stage of two-step aging in an Al-0.9%Mg-1.0%Si (mass%) alloy. Changes in size, volume fraction, number density, chemical composition, atomic number density, and hardness due to nanocluster dissolution and precipitate nucleation were mainly discussed. A summary of the main content is as follows.

- Nanoclusters in NA (2419.2 ks) formed in a size range of 0.44 ≦ $r_G$ ≦ 2.45. We confirmed that Si-rich (Mg/(Mg+Si) ≤ 0.4) and Balanced (0.4 < Mg/(Mg+Si) < 0.6) clusters mainly formed with a percentage of 97%. The larger the cluster, the more similar to the composition of the alloy (Mg/(Mg+Si) = 0.47).
- Microstructure changes at Two (0.6 ks) after NA (2419.2 ks) were described. Clusters larger than $r_G$ = 1.5 nm were not confirmed and smaller clusters (0.45 nm ≦$r_G$≦ 1.45 nm) were observed compared to NA (2419.2 ks). The number density at Two (0.6 ks) identified as 13.8 $10^{24}m^{-3}$ was lower than that of NA (2419.2 ks) of 23.5 $10^{24}m^{-3}$. Therefore, we concluded that the dissolution of the nanocluster predominantly occurs during Two (0.6 ks) after NA (2419.2 ks).
- Microstructure changes at Two (1.2 ks) after Two (0.6 ks) were characterized. The cluster size at Two (1.2 ks) was in the range of 0.52 nm ≤ $r_G$ ≤ 3.81 nm. In addition, the number density of 16.9 $10^{24}m^{-3}$ increased compared with Two (0.6 ks). After Two (0.6 ks), the formation of pre-β" was dominant during Two (1.2 ks), which confirmed that the chemical composition of the nanoclusters of 73% or more belongs to the Balanced composition. The chemical composition of the nanocluster approached the composition of β" with an increasing cluster size. Thus, the pre-β″ formed at Two (1.2 ks) was similar to the Mg: Si ratio of β″.

- To investigate the internal structure change of clusters at the initial stage of two-step aging, we analyzed the atomic number density of clusters with the largest cluster for each heat treatment condition. The atomic number density (Al+Mg+Si) at Two (1.2 ks) was higher than 30 $nm^{-3}$, while NA (2419.2 ks) and Two (0.6 ks) were lower than 30 $nm^{-3}$. The formation of β″ nuclei, i.e., based on hardness results of the formation of pre-β″, at Two (1.2 ks) dominated. The size and atomic density of the pre-β" as the nucleus of β" were higher than 2 nm and 30 $nm^{-3}$, respectively.
- Finally, we analyzed the relationship between the hardness change, the volume fraction and the number density at the initial stage of two-step aging. The lowest hardness at Two (0.6 ks) was due to the low volume fraction and number density after nanocluster dissolution. The average size and volume fraction of the cluster at Two (1.2 ks) were found to be higher than NA (2419.2 ks), with a low number density and hardness. An increase in the number density contributed more to strengthening than an increase in volume fraction at the initial stage of two-step aging in Al-Mg-Si alloys.

## References

[1] D.W. Pashley, J.W. Rohdes, A. Sendorek, Delayed Ageing in Aluminium-Magnesium-Silicon Alloys: Effect on Structure and Mechanical Properties, J. Institue Met. 94 (1966) 41–49.

[2] D.W. Pashley, M.H. Jacobs, J.T. Vietz, The basic processes affecting two-step ageing in an Al-Mg-Si alloy, Philos. Mag. 16 (1967) 51–76. https://doi.org/10.1080/14786436708229257.

[3] A. Serizawa, S. Hirosawa, T. Sato, 3DAP Characterization and Thermal Stability of Nano-Scale Clusters in Al-Mg-Si Alloys, Mater. Sci. Forum. 519–521 (2006) 245–250. https://doi.org/10.4028/www.scientific.net/MSF.519-521.245.

[4] C.D. Marioara, S.J. Andersen, J. Jansen, H.W. Zandbergen, Atomic model for GP-zones in a 6082 Al–Mg–Si system, Acta Mater. 49 (2001) 321–328. https://doi.org/10.1016/S1359-6454(00)00302-5.

[5] C.D. Marioara, S.J. Andersen, J. Jansen, H.W. Zandbergen, The influence of temperature and storage time at RT on nucleation of the β″ phase in a 6082 Al–Mg–Si alloy, Acta Mater. 51 (2003) 789–796. https://doi.org/10.1016/S1359-6454(02)00470-6.

[6] S. Hirosawa, T. Sato, Nano-Scale Clusters Formed in the Early Stage of Phase Decomposition of Al-Mg-Si Alloys, Mater. Sci. Forum. 475–479 (2005) 357–360. https://doi.org/10.4028/www.scientific.net/MSF.475-479.357.

[7] J. Kim, E. Kobayashi, T. Sato, Influence of Natural Aging Time on Two-Step Aging Behavior of Al-Mg-Si(-Cu) Alloys, Mater. Trans. 56 (2015) 1771–1780. https://doi.org/10.2320/matertrans.L-M2015824.

[8] S. Kim, J. Kim, E. Kobayashi, T. Sato, Influence of Mg/Si Ratio on Nanocluster Formation in Al-Mg-Si Alloys with Constant Mg+Si Concentration, Mater. Trans. 55 (2014) 1647–1655. https://doi.org/10.2320/matertrans.L-M2014832.

[9] Y. Takaki, T. Masuda, E. Kobayashi, T. Sato, Effects of Natural Aging on Bake Hardening Behavior of Al-Mg-Si Alloys with Multi-Step Aging Process, Mater. Trans. 55 (2014) 1257–1265. https://doi.org/10.2320/matertrans.L-M2014827.

[10] M. Werinos, H. Antrekowitsch, E. Kozeschnik, T. Ebner, F. Moszner, J.F. Löffler, P.J. Uggowitzer, S. Pogatscher, Ultrafast artificial aging of Al–Mg–Si alloys, Scr. Mater. 112 (2016) 148–151. https://doi.org/10.1016/j.scriptamat.2015.09.037.

[11] C.H. Liu, Y.X. Lai, J.H. Chen, G.H. Tao, L.M. Liu, P.P. Ma, C.L. Wu, Natural-aging-induced reversal of the precipitation pathways in an Al–Mg–Si alloy, Scr. Mater. 115 (2016) 150–154. https://doi.org/10.1016/j.scriptamat.2015.12.027.

[12] W.F. Miao, D.E. Laughlin, Precipitation hardening in aluminum alloy 6022, Scr. Mater. 40 (1999) 873–878. https://doi.org/10.1016/S1359-6462(99)00046-9.

[13] W.F. Miao, D.E. Laughlin, A differential scanning calorimetry study of aluminum alloy 6111 with different pre-aging treatments, J. Mater. Sci. Lett. 19 (2000) 201–203. https://doi.org/https://doi.org/10.1023/A:1006798305992.

[14] Y. Aruga, S. Kim, M. Kozuka, E. Kobayashi, T. Sato, Effects of cluster characteristics on two-step aging behavior in Al-Mg-Si alloys with different Mg/Si ratios and natural aging periods, Mater. Sci. Eng. A. 718 (2018) 371–376. https://doi.org/10.1016/j.msea.2018.01.086.

[15] J. Im, J. Kim, Effects of Si Addition with Natural Aging Time on the Two-Step and Multi-Step Aging Behavior in Al–Mg–Si Alloys, J. Nanosci. Nanotechnol. 17 (2017) 7912–7916. https://doi.org/10.1166/jnn.2017.15049.

[16] J. Im, J. Jeon, M. Song, S. Hong, J. Kim, Influence of Natural Aging Time and Mg/Si Ratio (Mg + Si = 1.3 mass%) on the Two-Step Aging Behavior in Al–Mg–Si Alloys, Met. Mater. Int. 25 (2019) 860–868. https://doi.org/10.1007/s12540-019-00257-8.

[17] J. Kim, S. Kim, E. Kobayashi, T. Sato, Thermal stability and transition behavior of nanoclusters during two-step aging at 250 °C in Al-Mg-Si(-Cu) alloys, Mater. Trans. 55 (2014) 768–773. https://doi.org/10.2320/matertrans.M2013411.

[18] J.H. Chen, E. Costan, M.A. van Huis, Q. Xu, H.W. Zandbergen, Atomic Pillar-Based Nanoprecipitates Strengthen AlMgSi Alloys, Science 312 (2006) 416–419. https://doi.org/10.1126/science.1124199.

[19] H. Chen, J. Lu, Y. Kong, K. Li, T. Yang, A. Meingast, M. Yang, Q. Lu, Y. Du, Atomic scale investigation of the crystal structure and interfaces of the B′ precipitate in Al-Mg-Si alloys, Acta Mater. 185 (2020) 193–203. https://doi.org/10.1016/j.actamat.2019.11.059.

[20] J.K. Sunde, C.D. Marioara, R. Holmestad, The effect of low Cu additions on precipitate crystal structures in overaged Al-Mg-Si(-Cu) alloys, Mater. Charact. 160 (2020) 110087. https://doi.org/10.1016/j.matchar.2019.110087.

[21] Y.X. Lai, W. Fan, M.J. Yin, C.L. Wu, J.H. Chen, Structures and formation mechanisms of dislocation-induced precipitates in relation to the age-hardening responses of Al-Mg-Si alloys, J. Mater. Sci. Technol. 41 (2020) 127–138. https://doi.org/10.1016/j.jmst.2019.11.001.

[22] M. Murayama, K. Hono, Pre-precipitate clusters and precipitation processes in Al–Mg–Si alloys, Acta Mater. 47 (1999) 1537–1548. https://doi.org/10.1016/S1359-6454(99)00033-6.

[23] B. Gault, M.P. Moody, F. De Geuser, G. Tsafnat, A. La Fontaine, L.T. Stephenson, D. Haley, S.P. Ringer, Advances in the calibration of atom probe tomographic reconstruction, J. Appl. Phys. 105 (2009). https://doi.org/10.1063/1.3068197.

[24] B. Gault, M.P. Moody, F. De Geuser, A. La Fontaine, L.T. Stephenson, D. Haley, S.P. Ringer, Spatial Resolution in Atom Probe Tomography, Microsc. Microanal. 16 (2010) 99–110. https://doi.org/10.1017/S1431927609991267.

[25] F. Vurpillot, G. Da Costa, A. Menand, D. Blavette, Structural analyses in three-dimensional atom probe: a Fourier transform approach, J. Microsc. 203 (2001) 295–302. https://doi.org/10.1046/j.1365-2818.2001.00923.x.

[26] F. VURPILLOT, F. DE GEUSER, G. DA COSTA, D. BLAVETTE, Application of Fourier transform and autocorrelation to cluster identification in the three-dimensional atom probe, J. Microsc. 216 (2004) 234–240. https://doi.org/10.1111/j.0022-2720.2004.01413.x.

[27] E. Cadel, F. Vurpillot, R. Lardé, S. Duguay, B. Deconihout, Depth resolution function of the laser assisted tomographic atom probe in the investigation of semiconductors, J. Appl. Phys. 106 (2009) 044908. https://doi.org/10.1063/1.3186617.

[28] Y. Aruga, M. Kozuka, Y. Takaki, T. Sato, Evaluation of Solute Clusters Associated with Bake-Hardening Response in Isothermal Aged Al-Mg-Si Alloys Using a Three-Dimensional Atom Probe, Metall. Mater. Trans. A. 45 (2014) 5906–5913. https://doi.org/10.1007/s11661-014-2548-y.

[29] Y. Aruga, M. Kozuka, Y. Takaki, T. Sato, Formation and reversion of clusters during natural aging and subsequent artificial aging in an Al–Mg–Si alloy, Mater. Sci. Eng. A. 631 (2015) 86–96. https://doi.org/10.1016/j.msea.2015.02.035.

[30] V. Fallah, B. Langelier, N. Ofori-Opoku, B. Raeisinia, N. Provatas, S. Esmaeili, Cluster evolution mechanisms during aging in Al–Mg–Si alloys, Acta Mater. 103 (2016) 290–300. https://doi.org/10.1016/j.actamat.2015.09.027.

[31] O. Engler, C.D. Marioara, Y. Aruga, M. Kozuka, O.R. Myhr, Effect of natural ageing or pre-ageing on the evolution of precipitate structure and strength during age hardening of Al–Mg–Si alloy AA 6016, Mater. Sci. Eng. A. 759 (2019) 520–529. https://doi.org/10.1016/j.msea.2019.05.073.

[32] W. Tu, J. Tang, L. Ye, L. Cao, Y. Zeng, Q. Zhu, Y. Zhang, S. Liu, L. Ma, J. Lu, B. Yang, Effect of the natural aging time on the age-hardening response and precipitation behavior of the Al-0.4Mg-1.0Si-(Sn) alloy, Mater. Des. 198 (2021) 109307. https://doi.org/10.1016/j.matdes.2020.109307.

[33] Vurpillot, Bostel, Blavette, The shape of field emitters and the ion trajectories in three-dimensional atom probes, J. Microsc. 196 (1999) 332–336. https://doi.org/10.1046/j.1365-2818.1999.00637.x.

[34] F. Vurpillot, A. Bostel, E. Cadel, D. Blavette, The spatial resolution of 3D atom probe in the investigation of single-phase materials, Ultramicroscopy. 84 (2000) 213–224. https://doi.org/10.1016/S0304-3991(00)00035-8.

[35] J.M. Hyde, E.A. Marquis, K.B. Wilford, T.J. Williams, A sensitivity analysis of the maximum separation method for the characterisation of solute clusters, Ultramicroscopy. 111 (2011) 440–447. https://doi.org/10.1016/j.ultramic.2010.12.015.

[36] M.K. Miller, R.G. Forbes, Atom-Probe Tomography, 1st ed., Springer US, Boston, MA, 2014. https://doi.org/10.1007/978-1-4899-7430-3.

[37] T. Hirata, S. Matsuo, Two-Step Ageing Behaviours in an Al-1.2 wt% $Mg_2Si$ Alloy, Trans. Japan Inst. Met. 13 (1972) 231–237. https://doi.org/10.2320/matertrans1960.13.231.

[38] G.H. Tao, C.H. Liu, J.H. Chen, Y.X. Lai, P.P. Ma, L.M. Liu, The influence of Mg/Si ratio on the negative natural aging effect in Al–Mg–Si–Cu alloys, Mater. Sci. Eng. A. 642 (2015) 241–248. https://doi.org/10.1016/j.msea.2015.06.090.

[39] K. Yamada, T. Sato, A. Kamio, Effects of Quenching Conditions on Two-Step Aging Behavior of Al-Mg-Si Alloys, Mater. Sci. Forum. 331–337 (2000) 669–674. https://doi.org/10.4028/www.scientific.net/MSF.331-337.669.

[40] A. Serizawa, S. Hirosawa, T. Sato, Three-Dimensional Atom Probe Characterization of Nanoclusters Responsible for Multistep Aging Behavior of an Al-Mg-Si Alloy, Metall. Mater. Trans. A. 39 (2008) 243–251. https://doi.org/10.1007/s11661-007-9438-5.

[41] A.K. Gupta, D.J. Lloyd, Study of precipitation kinetics in a super purity Al-0.8 pct Mg-0.9 pct Si alloy using differential scanning calorimetry, Metall. Mater. Trans. A. 30 (1999) 879–884. https://doi.org/10.1007/s11661-999-0081-1.

[42] J. Banhart, C.S.T. Chang, Z. Liang, N. Wanderka, M.D.H. Lay, A.J. Hill, Natural Aging in Al-Mg-Si Alloys - A Process of Unexpected Complexity, Adv. Eng. Mater. 12 (2010) 559–571. https://doi.org/10.1002/adem.201000041.

[43] C.S.T. Chang, J. Banhart, Low-Temperature Differential Scanning Calorimetry of an Al-Mg-Si Alloy, Metall. Mater. Trans. A. 42 (2011) 1960–1964. https://doi.org/10.1007/s11661-010-0596-5.

[44] J. Kim, J. Im, M. Song, I. Kim, Effects of Mg Addition and Pre-Aging on the Age-Hardening Behavior in Al-Mg-Si, Metals (Basel). 8 (2018) 1046. https://doi.org/10.3390/met8121046.

[45] G.A. Edwards, K. Stiller, G.L. Dunlop, M.J. Couper, The precipitation sequence in Al–Mg–Si alloys, Acta Mater. 46 (1998) 3893–3904. https://doi.org/10.1016/S1359-6454(98)00059-7.

[46] K. HIRANO, Diffusion in aluminum, J. Japan Inst. Light Met. 29 (1979) 249–262. https://doi.org/10.2464/jilm.29.249.

[47] M. Werinos, H. Antrekowitsch, T. Ebner, R. Prillhofer, P.J. Uggowitzer, S. Pogatscher, Hardening of Al–Mg–Si alloys: Effect of trace elements and prolonged natural aging, Mater. Des. 107 (2016) 257–268. https://doi.org/10.1016/j.matdes.2016.06.014.

[48] H. Li, Z. Yan, L. Cao, Bake hardening behavior and precipitation kinetic of a novel Al-Mg-Si-Cu aluminum alloy for lightweight automotive body, Mater. Sci. Eng. A. 728 (2018) 88–94. https://doi.org/10.1016/j.msea.2018.05.014.

[49] J. Kim, E. Kobayashi, T. Sato, Effects of Cu Addition on Behavior of Nanoclusters during Multi-Step Aging in Al-Mg-Si Alloys, Mater. Trans. 52 (2011) 906–913. https://doi.org/10.2320/matertrans.L-MZ201121.

[50] M.J. Whelan, On the Kinetics of Precipitate Dissolution, Met. Sci. J. 3 (1969) 95–97. https://doi.org/10.1179/msc.1969.3.1.95.

[51] M. Madanat, M. Liu, J. Banhart, Reversion of natural ageing in Al-Mg-Si alloys, Acta Mater. 159 (2018) 163–172. https://doi.org/10.1016/j.actamat.2018.07.066.

[52] S. Pogatscher, H. Antrekowitsch, H. Leitner, T. Ebner, P.J. Uggowitzer, Mechanisms controlling the artificial aging of Al–Mg–Si Alloys, Acta Mater. 59 (2011) 3352–3363. https://doi.org/10.1016/j.actamat.2011.02.010.

[53] M. Torsæter, H.S. Hasting, W. Lefebvre, C.D. Marioara, J.C. Walmsley, S.J. Andersen, R. Holmestad, The influence of composition and natural aging on clustering during preaging in Al–Mg–Si alloys, J. Appl. Phys. 108 (2010) 073527. https://doi.org/10.1063/1.3481090.

[54] W. Yang, M. Wang, R. Zhang, Q. Zhang, X. Sheng, The diffraction patterns from β″ precipitates in 12 orientations in Al–Mg–Si alloy, Scr. Mater. 62 (2010) 705–708. https://doi.org/10.1016/j.scriptamat.2010.01.039.

[55] H.W. Zandbergen, S.J. Andersen, J. Jansen, Structure Determination of Mg 5 Si 6 Particles in Al by Dynamic Electron Diffraction Studies, Science 277 (1997) 1221–1225. https://doi.org/10.1126/science.277.5330.1221.

[56] H.K. Hasting, W. Lefebvre, C. Marioara, J.C. Walmsley, S. Andersen, R. Holmestad, F. Danoix, Comparative study of the β″-phase in a 6xxx Al alloy by 3DAP and HRTEM, Surf. Interface Anal. 39 (2007) 189–194. https://doi.org/10.1002/sia.2487.

[57] L. Cao, P.A. Rometsch, M.J. Couper, Clustering behaviour in an Al–Mg–Si–Cu alloy during natural ageing and subsequent under-ageing, Mater. Sci. Eng. A. 559 (2013) 257–261. https://doi.org/10.1016/j.msea.2012.08.093.

[58] A. V. Ceguerra, M.P. Moody, L.T. Stephenson, R.K.W. Marceau, S.P. Ringer, A three-dimensional Markov field approach for the analysis of atomic clustering in atom probe data, Philos. Mag. 90 (2010) 1657–1683. https://doi.org/10.1080/14786430903441475.

[59] S. Esmaeili, D. Vaumousse, M.W. Zandbergen, W.J. Poole, A. Cerezo, D.J. Lloyd, A study on the early-stage decomposition in the Al-Mg-Si-Cu alloy AA6111 by electrical resistivity and three-dimensional atom probe, Philos. Mag. 87 (2007) 3797–3816. https://doi.org/10.1080/14786430701408312.

[60] R.K.W. Marceau, A. De Vaucorbeil, G. Sha, S.P. Ringer, W.J. Poole, Analysis of strengthening in AA6111 during the early stages of aging: Atom probe tomography and yield stress modelling, Acta Mater. 61 (2013) 7285–7303. https://doi.org/10.1016/j.actamat.2013.08.033.

[61] M.W. Zandbergen, Q. Xu, A. Cerezo, G.D.W. Smith, Study of precipitation in Al–Mg–Si alloys by Atom Probe Tomography I. Microstructural changes as a function of ageing temperature, Acta Mater. 101 (2015) 136–148. https://doi.org/10.1016/j.actamat.2015.08.017.

[62] M.W. Zandbergen, A. Cerezo, G.D.W. Smith, Study of precipitation in Al–Mg–Si Alloys by atom probe tomography II. Influence of Cu additions, Acta Mater. 101 (2015) 149–158. https://doi.org/10.1016/j.actamat.2015.08.018.

[63] A.K. Vasudevan, R.D. Doherty, Aluminum Alloys: Contemporary Research and Applications, 1989.

[64] O. Wouters, Plasticity in Aluminum Alloys at Various Length Scales, Groningen, 2006. https://doi.org/https://doi.org/90-367-2541-0.

[65] A.J. Ardell, Precipitation hardening, Metall. Trans. A. 16 (1985) 2131–2165. https://doi.org/10.1007/BF02670416.

[66] M.J. Starink, L.F. Cao, P.A. Rometsch, A model for the thermodynamics of and strengthening due to co-clusters in Al–Mg–Si-based alloys, Acta Mater. 60 (2012) 4194–4207. https://doi.org/10.1016/j.actamat.2012.04.032.

**Tables**

Table 6.1 Statistical data analyzed by a $N_{min}$ of 10 atoms and $D_{max}$ 0.75 nm of atom probe measurements.

| | Volume fraction | Number density ($10^{24}$ $m^{-3}$) | Guinier radius (nm) | Mg/(Mg+Si) value | Atomic density ($nm^{-3}$) |
|---|---|---|---|---|---|
| NA (2419.2 ks) | 0.13 | 23.5 | 0.91 | 0.46 | 53.9 |
| Two (0.6 ks) | 0.02 | 13.8 | 0.73 | 0.50 | 48.9 |
| Two (1.2 ks) | 0.14 | 16.9 | 0.93 | 0.53 | 61.7 |

Table 6.2 Summary of distribution of Si-rich, Balanced and Mg-rich clusters in each heat treatment condition of Fig. 6.

| | Number fraction of clusters (%) | | |
|---|---|---|---|
| | Si-rich | Balanced | Mg-rich |
| NA(2419.2 ks) | 44 | 53 | 3 |
| Two(0.6 ks) | 37 | 42 | 21 |
| Two(1.2 ks) | 17 | 75 | 8 |

Table 6.3 Statistical data for the top and bottom 10% of the Guinier radius. *rmax G* and *rmin G* represent top and bottom, respectively.

| $r_G^{max}$ | Guinier radius (nm) | Mg/(Mg+Si) value | Atomic density ($nm^{-3}$) |
|---|---|---|---|
| NA (2419.2 ks) | 2.06 | 0.47 | 22 |
| Two (0.6 ks) | 1.21 | 0.44 | 23 |
| Two (1.2 ks) | 2.23 | 0.46 | 49 |


| $r_G^{max}$ | Guinier radius (nm) | Mg/(Mg+Si) value | Atomic density ($nm^{-3}$) |
|---|---|---|---|
| NA (2419.2 ks) | 2.06 | 0.47 | 22 |
| Two (0.6 ks) | 1.21 | 0.44 | 23 |
| Two (1.2 ks) | 2.23 | 0.46 | 49 |

Table 6.4 Chemical composition analysis results for nanocluster in literature based on APT results.

| Natural aging time (ks) | Chemical composition of alloy (mass %) | | Mg/(Mg+Si) value of alloy | Chemical composition of nanocluster | Reference |
|---|---|---|---|---|---|
| | Mg | Si | | | |
| $6.05 \times 10^3$ | 0.62 | 0.34 | 0.65 | Similar to the composition of the alloy | Murayama et al. [26] |
| | 0.58 | 0.73 | 0.44 | | |
| 108 | 0.62 | 0.93 | 0.40 | Avg. 0.46 | Aruga et al. [18] |
| | 0.78 | 0.70 | 0.53 | Avg. 0.60 | |
| $7.20 \times 10^3$ | 0.62 | 0.93 | 0.40 | Avg. 0.52 | |
| | 0.78 | 0.70 | 0.53 | Avg. 0.54 | |
| Up to $7.88 \times 10^4$ | 0.78 | 0.81 | 0.49 | Random | Serizawa et al. [32] |
| $6.05 \times 10^2$ | 0.36 | 0.83~87 | 0.30 | Mainly distributed of similar to the composition of the alloy | Torsæter et al. [33] |
| | 0.74~77 | 0.43~54 | 0.61 | | |

**Figures**

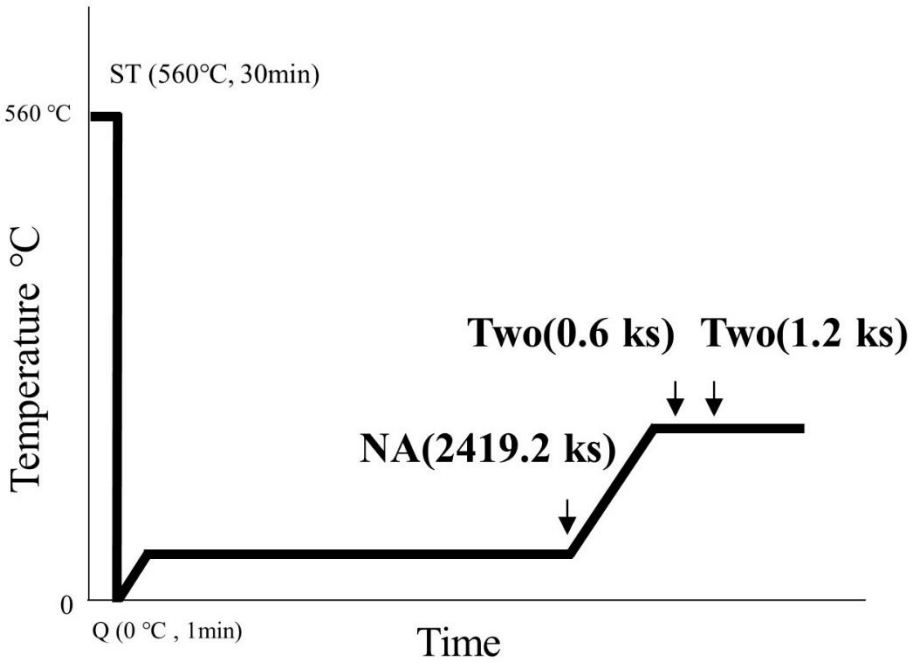


Figure 6.1 Heat treatment history of the two-step aging process. ST, NA and Two stand for solid solution heat treatment, natural aging, and two-step aging, respectively. Natural aging was carried out for 2419.2 ks. Two-step aging, artificial aging at 170 °C after natural aging for 2419.2 ks was conducted.

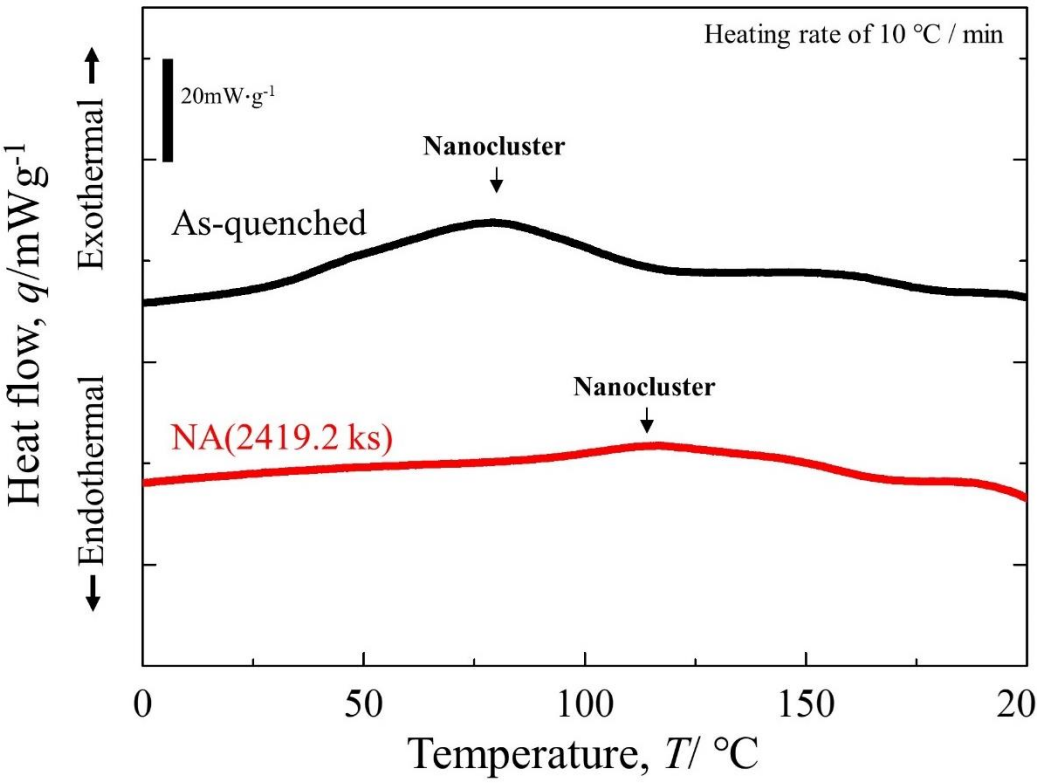


Figure 6.2 Show the DSC thermograms of the as-quenched (black solid line) and natural aged for 2419.2 ks (red solid line) specimens.

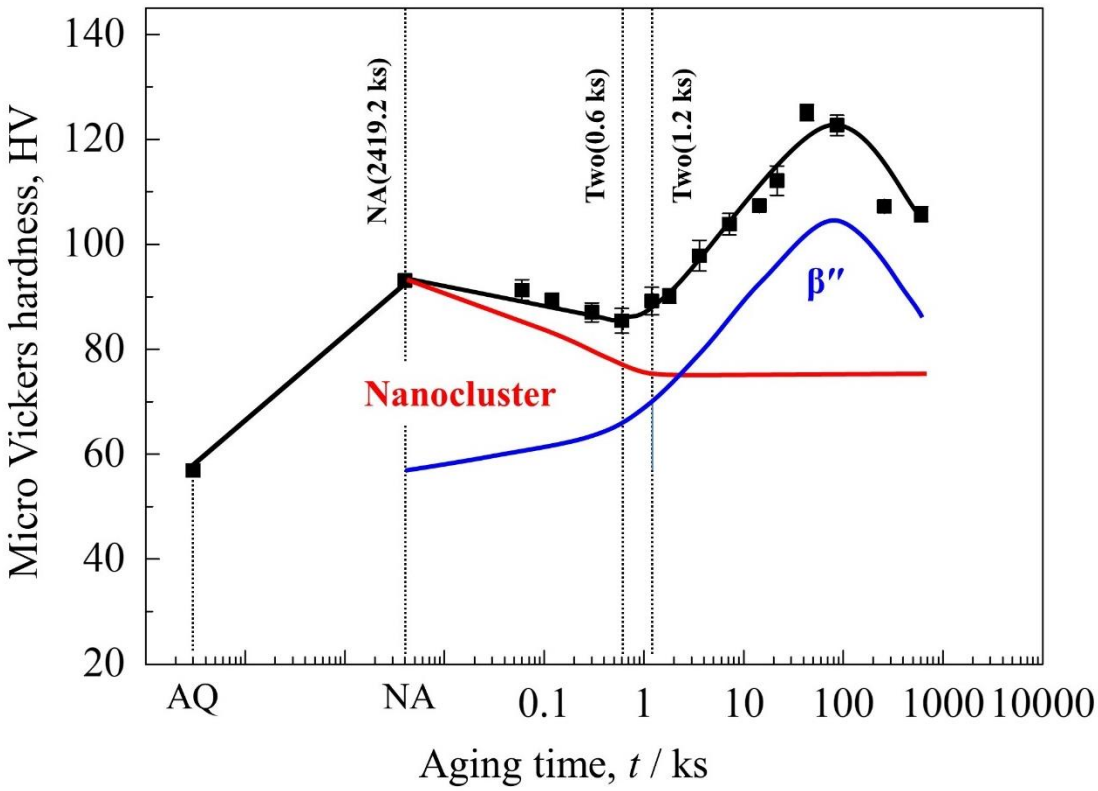


Figure 6.3 Hardness changes during two-step aging at 170 °C after natural aging for 2419.2 ks. Hardness changes (black line) at the initial stage of two-step aging are caused by the nanocluster dissolution (red line) and the formation of precipitates (blue line). The hardness increases and decreases were dominant due to the formation of precipitates and dissolution of nanoclusters, respectively.

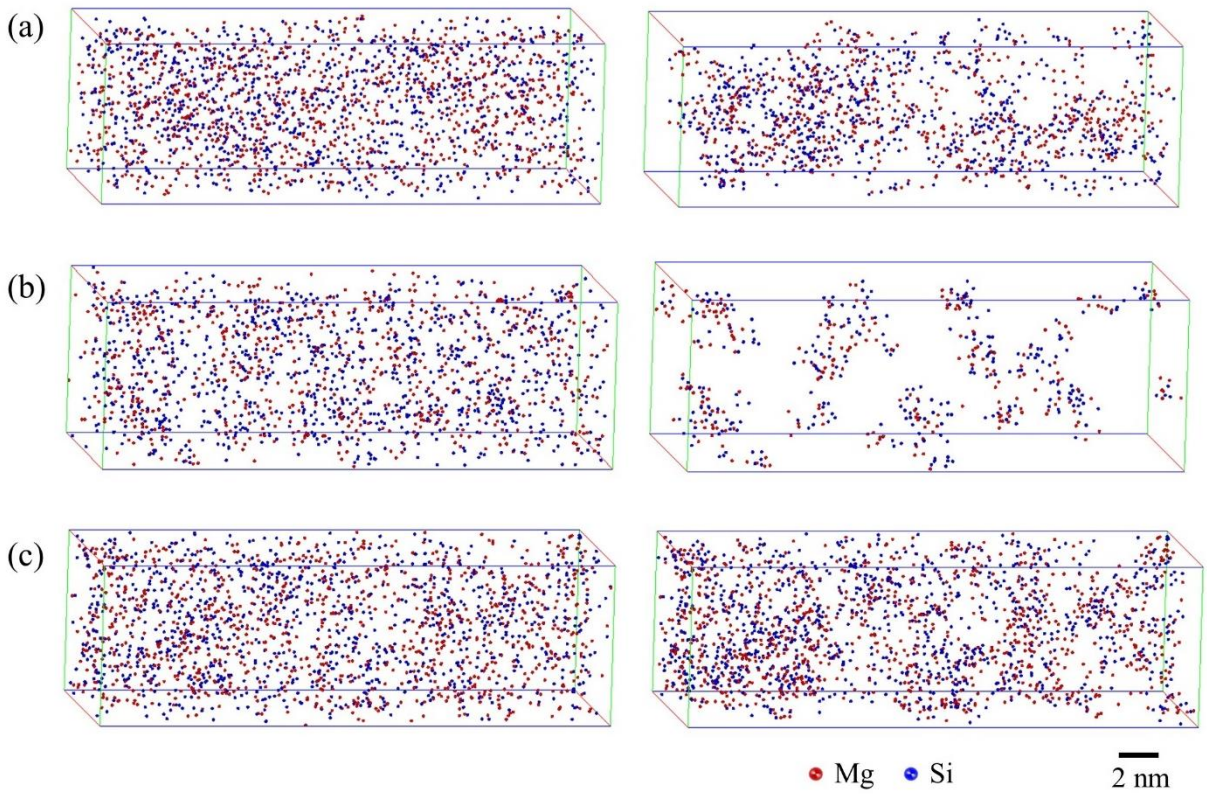


Figure 6.4 APT maps showing the distribution of analyzed clusters (a) after natural aging for 2419.2 ks, two-step aging at 170 ℃ for (b) 0.6 and (c) 1.2 ks after natural aging. The maps on the left and right represent the solute atoms at the region of interest and after cluster analysis by maximum separation method.

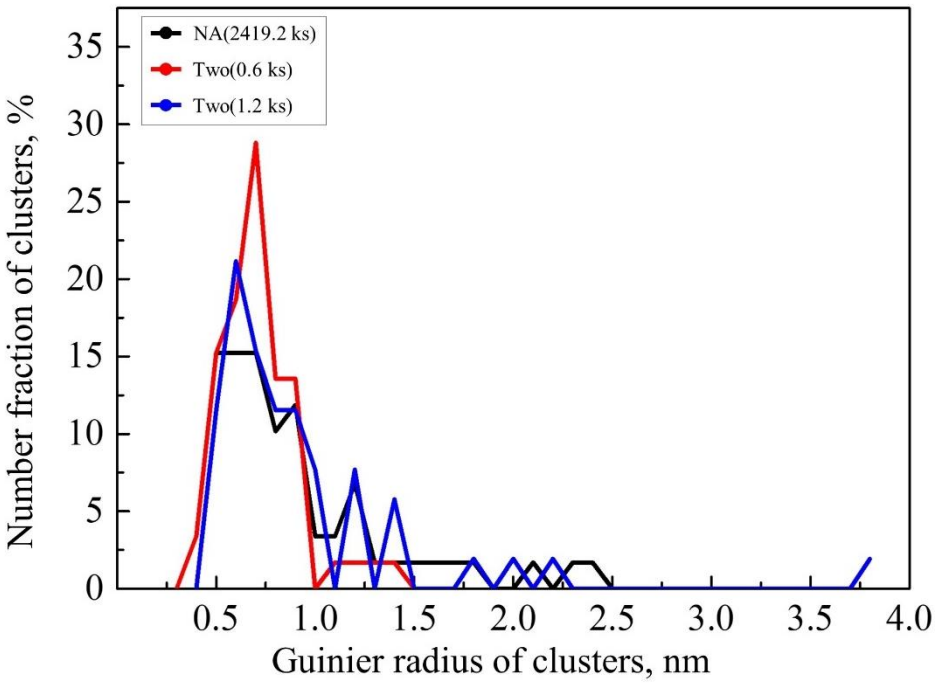


Figure 6.5 Comparison of size distribution of clusters with the different heat treatment condition. NA and Two stand for natural aging and two-step aging (artificial aging at 170 ℃ after natural aging for 2419.2 ks), respectively.

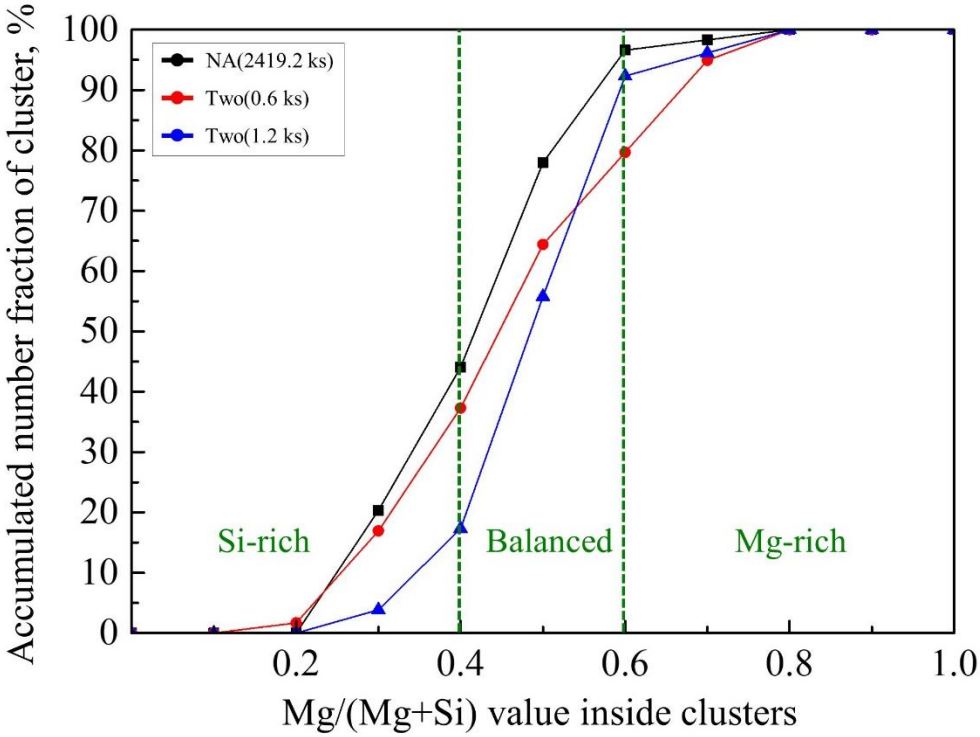


Figure 6.6 Accumulated cluster fraction with Mg/(Mg+Si) value inside clusters. Si-rich, balanced and Mg-rich clusters were classified by the Mg/(Mg+Si) values of less than 0.4, 0.4 to 0.6 and greater than 0.6 ks, respectively.

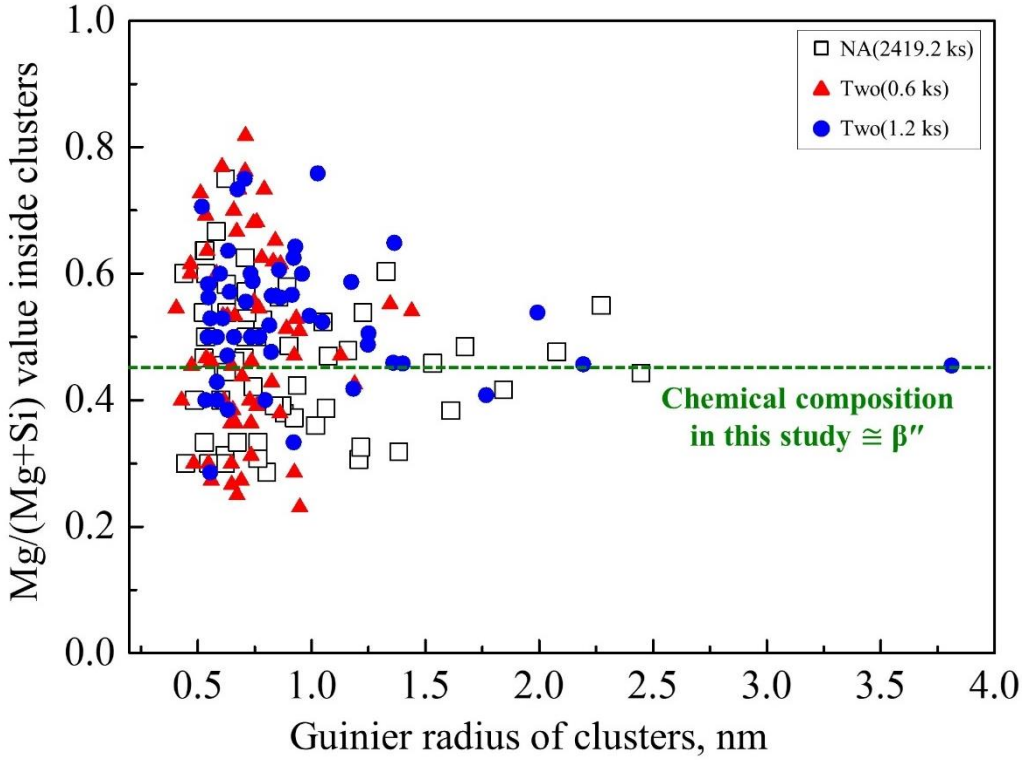


Figure 6.7 Comparison of relationship between size and Mg/(Mg+Si) value inside clusters. Green dotted line represents the chemical composition in this study. NA and Two stand for natural aging and two-step aging (artificial aging at 170 ℃ after natural aging for 2419.2 ks), respectively.

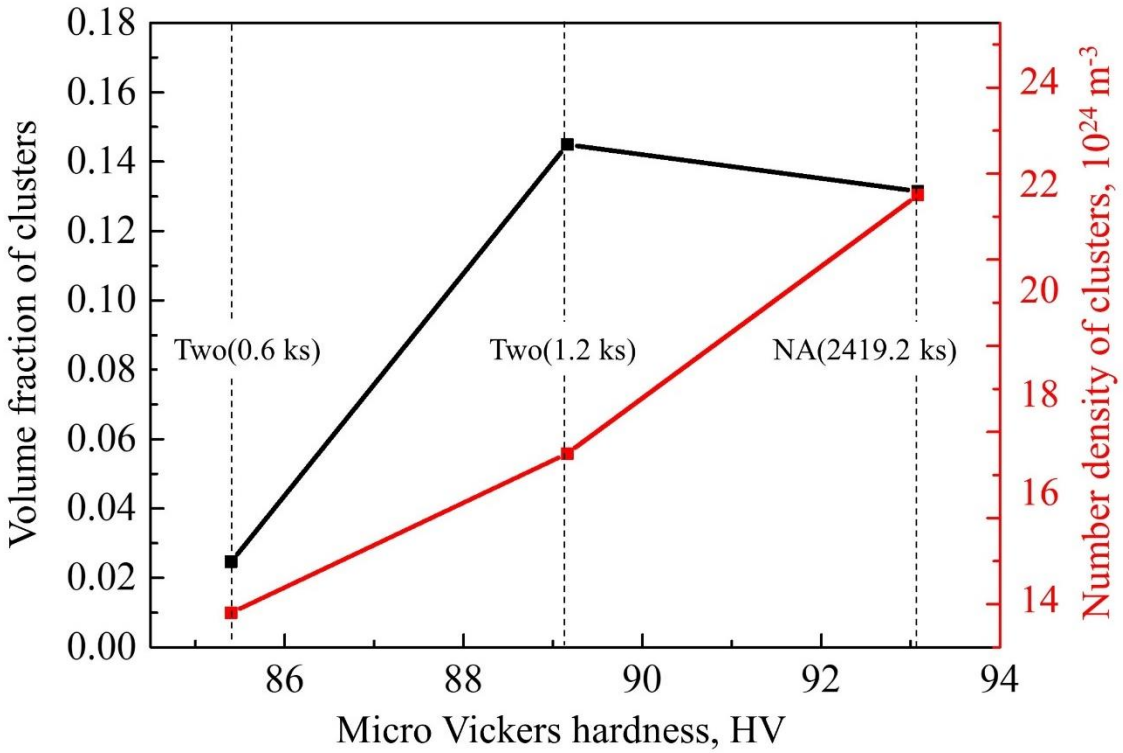


Figure 6.8 Relationship between hardness changes, volume fraction and number density of clusters with the different heat treatment histories. NA and Two stand for natural aging and two-step aging (artificial aging at 170 ℃ after natural aging for 2419.2 ks), respectively.

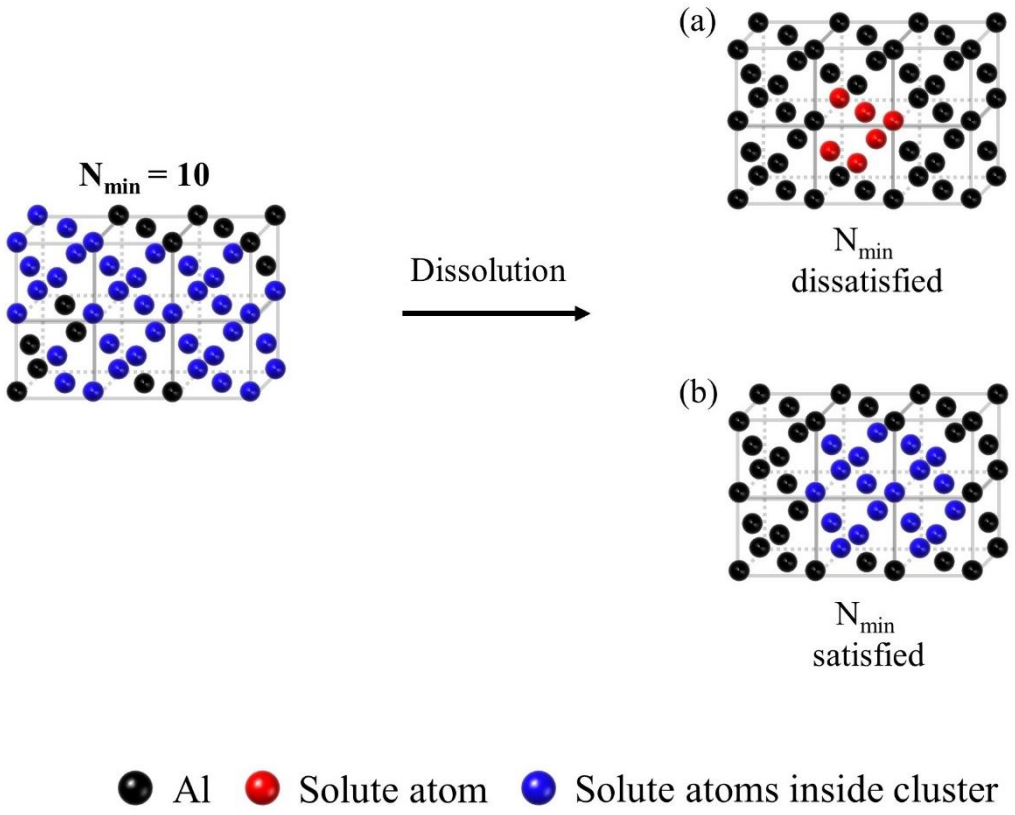


Figure 6.9 Schematic of the phenomena that can occur during nanocluster dissolution. (a) is not recognized as a cluster and causes a decrease in number density. (b) is the situation where only the size of cluster is reduced despite the dissolution.

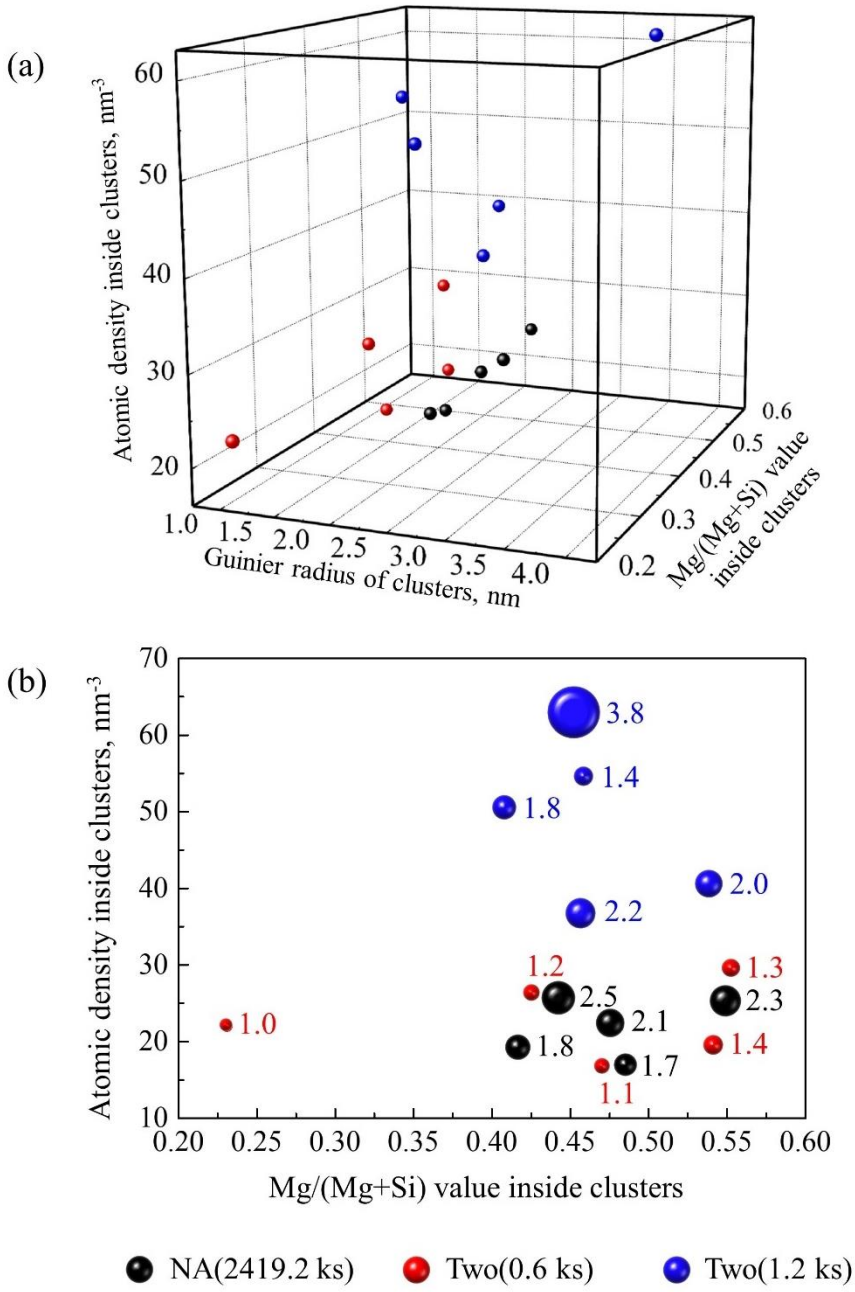


Figure 6.10 The relationship between atomic density (Al+Mg+Si), $r_G$ and Mg/(Mg+Si) value of five clusters included in $r_G^{max}$ of Table 3 in each heat treatment condition is shown. Black, red and blue spheres represent NA(2419.2 ks), Two(0.6 ks) and Two(1.2 ks), respectively. (a) shows each variable in three dimensional, and (b) shows the $r_G$ as the size of a sphere. The number in (b) represent the $r_G$ of each cluster.

# Chapter 7

# General conclusions

The principle objective of the present thesis is described in the **Chapter 1**.

***"Evolution and Thermal Stability of Nanoclusters in Al-Mg-Si Alloys: Insights from Interatomic Structure of Clusters Formed at Low Temperature and Two-step Aging"*** is successfully achieved throughout the previous chapters. The main findings of each chapter are summarized in this chapter.

In the **Chapter 1** ***"General introduction"***, background and the controversial issues related to the clustering evolution and thermal stability of nanoclusters in Al-Mg-Si alloys were presented. To better understand these issues, the necessity of analyzing the interatomic structure of nanoclusters using APT was described.

In the **Chapter 2** ***"Parameters optimization in cluster identification algorithms for characterizing nanoclusters in Al-Mg-Si-Cu alloys"***, the optimization of user-defined parameters in cluster identification algorithm were attempted. The four types of unphysical clusters were confirmed: large size having alloy composition, string-like, fragmented and connected clusters. It was confirmed that the combination of the parameters that minimized those unphysical clusters was in good agreement with the volume render and isoconcentration surface. A proposal was successfully made for optimizing user-defined parameters in the DBSCAN algorithm to perform cluster analysis on Al-Mg-Si-Cu alloy.

In the **Chapter 3** ***"Transition behavior of nanoclusters under sufficient low-temperature aging time in Al-Mg-Si alloy"***, the transition behavior of the nanoclusters at 50 °C considering the diffusion rate of solute atoms was investigated. Despite the expectation that Cluster (2)

should be sufficiently formed based on the normalized aging time, the results of DSC, hardness, and electrical resistivity experiments indicated the formation of the thermally unstable Cluster (1). From these results, it was concluded that the temperature increased from room temperature accelerated the Mg-enrichment of the clusters, but it did not facilitate the transition from Cluster (1) to Cluster (2).

In the **Chapter 4** ***"Interatomic structure as a determining factor of thermal stability of nanoclusters in Al-Mg-Si alloy"***, the relationship between interatomic structure and thermal stability of the nanoclusters were discussed via concentration profile that provide the atomic arrangement inside clusters. The clusters formed at 50 °C for the same aging time were found to be more thermally unstable than the clusters formed during NA. Those clusters formed at different temperatures were indistinguishable based on atomic arrangement-independent characteristics such as size, composition and atomic density. On the other hand, it was observed that the clusters formed during 50 °C had a Mg-rich core-shell structure, which was different from the clusters formed during NA.

In the **Chapter 5** ***"Correlation between nanocluster evolution and aging temperature in Al-Mg-Si alloy"***, the reason for the complex clustering evolution with different temperatures were investigated by newly proposed approaches. Two distinct clustering evolutions were observed, determined by the transition temperature between 40 and 70 °C. The clusters capable/incapable of continuous evolution were found to have low/high solute atom concentration cores, respectively.

In the **Chapter 6** ***"Microstructural evolution at the initial stage of two-step aging in an Al-Mg-Si alloy"***, the change in microstructure due to the simultaneous contribution of nanocluster dissolution and nucleation of precipitate was investigated. During the two-step aging after natural aging for 2419.2 ks, until the hardness reached a minimum and increased again,

nanocluster dissolution and formation of β″ nucleus were predominantly observed, respectively. The partial dissolution of clusters was observed during the initial stage of two-step aging. It was found that the clusters with high atomic density can serve as nuclei for precipitation, in contrast to clusters of similar size formed during natural aging.

In the **Chapter 7 "*General conclusions*"**, the major results and findings obtained from **Chapter 2** to **Chapter 6** are summarized. The difficulty of studying nanoclusters in Al-Mg-Si alloys due to the limitations of the analysis method was overcome through the newly proposed interatomic structure analysis using APT. This analysis result provided a critical experimental evidence to reveal the controversial issues surrounding clustering evolution and thermal stability of nanoclusters, leading to a better understanding of the complex two-step aging behavior in Al-Mg-Si alloys. Those research achievements contribute to design the alloy and heat-treatment history to control the microstructure of Al-Mg-Si panels manufactured by two-step aging process.

# Acknowledgements

I would like to express my sincere gratitude to those who provided unsparing help and support during the research and writing process of this doctoral thesis, as well as outside of the research.

First and foremost, I am deeply grateful to my supervisor Assoc. Prof. Equo Kobayashi for valuable guidance and active advice provided during both the internal and external aspects of my research. I am very grateful for the opportunity to pursue a doctoral program at Tokyo Institute of Technology, especially Kobayashi laboratory. His unwavering support and perseverance have been instrumental in increasing my confidence and enabling me to successfully complete my degree. I am truly fortunate to have had the opportunity of studying under his supervision.

I would like to extend my gratitude to the members of my thesis committee, Prof. Toshiyuki Fujii, Prof. Ji Shi, Prof. Eiji Tada and Assoc. Prof. Shinji Muraishi for their contributions. Their insightful comments and questions gave me the opportunity to think deeply about my research.

I would like to acknowledge to Dr. JaeHwang Kim for his unstinting support throughout the whole research work. His insightful comments and thought-provoking discussions have played a critical role in determining the direction of my thesis. Moreover, I am deeply grateful for the opportunity to receive guidance on the essential qualities of a researcher.

I sincerely thank Ass. Prof. MinHo O for giving me advice beyond the academic realm. His generous assistance during my time in the research lab has enabled me to dedicate myself to my studies. I also thank to Assoc. Prof. HeeSoo Kim for his encouragement.

Finally, I would like to express my deep gratitude to my parents, older brother and HyangHwa Kim for their support, understanding and encouragement during my Ph.D. work.

Their belief in me has been a source of strength throughout this challenging journey. This thesis has been successfully completed thanks to their dedication.

August, 2023

MinYoung Song